NANO- AND MICRO-SCALE TECHNIQUES FOR ELECTRICAL TRANSPORT MEASUREMENTS

BENJAMIN HEATHCOTE WILLIAMS

St. Edmund Hall

A thesis submitted for the degree of

Doctor of Philosophy

Clarendon Laboratory

University of Oxford

Trinity Term 2016

Benjamin Heathcote Williams: *Nano- and micro-scale techniques for electrical transport measurements,* a thesis submitted for the degree of Doctor of Philosophy, Trinity Term 2016

NANO- AND MICRO-SCALE TECHNIQUES FOR ELECTRICAL TRANSPORT MEASUREMENTS

BENJAMIN HEATHCOTE WILLIAMS
Clarendon Laboratory & St. Edmund Hall, University of Oxford

DPhil thesis, Trinity Term 2016

ABSTRACT

This thesis outlines the development of two new techniques that exploit very small structures, on the micro- and nano-scale, to enable innovative electrical transport measurements on a variety of materials of current interest in condensed matter physics.

The first technique aims to apply the versatility of electron-beam lithography for micro-fabrication of patterned electronic circuitry to the problem of performing transport experiments on individual crystallites taken from a typical powder sample. We show that these small samples, tens of microns in size, are actually often very high quality single crystals and can be exploited for measurements of electrical transport in materials of which no larger crystals are available. By way of demonstration, we present the results of preliminary transport measurements on a crystallite of the layered oxide chalcogenide $Sr_2MnO_2Cu_{1.5}Se_2$. We report a phase transition in the resistivity at 213 K which may correspond to the onset of previously reported short-range order in copper and vacancy sites in the $Cu_{1.5}Se_2$ planes.

The second technique is designed to investigate the topological protection of surface transport in 3-D topological insulators. We decorate the surfaces of single-crystal samples with two different species from a well-characterised family of single-molecule magnets. The two coatings have an electrostatically identical influence on the sample surface, but differ in that one species carries a spin and the other is spinless. The spinless molecule acts as a control, to allow us to cleanly determine the influence of the magnetic component of a scattering potential on transport in the surface. With this technique we investigate proposed topological Kondo insulator SmB_6. We find that the surface state dominates low-temperature transport and demonstrate that the momentum relaxation is very sensitive to a spin degree of freedom in the scatterer, in keeping with expectations of a topological insulator.

You're an idiot! —
Lucy Judson on thermodynamics

ACKNOWLEDGEMENTS

It is a fallacy, not often enough acknowledged, that any doctoral student can claim sole credit for the contents of their thesis. Over the course of a long and sometimes trying period of research, I have become ever more keenly aware of my dependence on the patience, generosity and kindness of my colleagues, friends and family. In my under-slept haze as I prepare to print this, I am bound to forget to thank more than one of them, for which I can only apologise. Each of them has as much a claim to this doctorate as I do.

Firstly, of course, I would not be submitting this thesis today if it were not for my supervisors, Moon-Sun Nam and Arzhang Ardavan. Under the circumstances, the fact that nobody died can be regarded as a triumph in itself. I am also deeply indebted to Steve Blundell for bravely trying to use me to fill a very large Tom Lancaster-shaped hole at Mansfield. When the research felt like it was going nowhere, my students there provided an invaluable source of amusement, inspiration and money. Jason Brown and Dave Sharp showed near-infinite patience while I bumbled around in their cleanrooms. Paolo Radaelli has given me much support and advice. Simon Clarke patiently provided a steady stream of interesting powder samples. Paul Goddard and Roger Johnson bookended my doctorate with two fun experiments overseas, where I didn't quite break everything, and provided no end of support in between. Alice Taylor has become a great friend and an excellent role model for a scientific career—she's quitting. Alongside teaching, I've kept myself sane by throwing liquid nitrogen at schoolchildren and unsuspecting members of the public. In this I am indebted to Andrews Boothroyd and Steele, for inspiration and for buying the nitrogen, and to Siân Tedaldi, for putting our amateur enthusiasm to good use. Danielle Kaminski, Amy Webber and Junjie Liu provided tea and solidarity. Stephen gave us all something to cheer about, Tash lost some samples for me to find, Jordan kept me in mounties and burnt toast, Alex kept me in wry northern humour, Sam kept me in wry southern humour, Arjun invited us to his own private Diwali, Alun to a most glorious wedding, my fellow musketeers and other office-mates have put up with my hair-tearing angst with good humour, Dave and Fran have grown up so fast and I'm *so proud*… In fact, I have been lucky to have been surrounded by so many good colleagues and friends that I cannot possibly mention them all by name. To every one of them, I'm very grateful.

Outside the lab, I have been perhaps even luckier in the people I've been able to spend my time in Oxford with. I'm deeply grateful to Sam and Peggy, for teaching me how to kayak, to Alice for ceilidhs and swimming, to Hog for keeping me in culture when I couldn't afford it, to Dinah and Jesse for letting me loose on the farm, to Eleanor and Paul for letting the cats try to help me write my thesis, to Rory and Kat for music and merriment and to all the old Magdalen gang for (sometimes) tolerating my ambitious walks and, more recently, for tolerating my increasingly long periods of silence. The Maison Franglais, in both its incarnations, has been the very best of houses, and Pauline, Paul, Ed and Sarah the very best of friends and housemates. They have tolerated my long quiet spells, disappearances and moody blues when the work was tough, as well as my tendency to distract myself by taking things apart when they may or may not have needed fixing, not to mention my more recent poverty, of which they have been incredibly tolerant. More recently, I've spent quite a lot of my time split between two houses and I owe Gill and Ian an enormous debt of gratitude for letting me squat uninvited and hide myself away with my computer and most of their tea.

Throughout these six years of tightened belt and shortened fuse, my family have been unbelievably patient and supportive. My parents, Corinna and Nick, have been accepting of my clearly unwise career choices without passing judgement. Without their love and unquestioning support, I would have given up long ago. Josh and Bex have never hesitated to cut me down to size when I needed it, and have never hesitated to prop me back up when I needed it more. One of my greatest regrets of having spent such a large portion of the last few years either working or worrying about work, is that I sometimes feel I've missed them both growing up and overtaking me. I hope I can now start to make amends for my absence.

Lastly, I had originally intended that one person should go conspicuously nameless on this page, in the interest of maintaining an elaborate charade. She has borne more of my doom and gloom than anyone else, has kept me sane and has shown incredible patience for my amateurish scientific dabblings while she gets on with real hard work. There have been several times over the past months when I have been convinced that she would be better off to have nothing more to do with me and my eternal thesis. I'm very lucky that it hasn't quite dawned on her yet.

REVISED ACKNOWLEDGEMENTS FOR A REVISED THESIS

It seemed rather extravagant to indulge myself in two whole pages to thank everyone who had a hand in the production of the first submitted version of this thesis. Unfortunately for the reader, I was encouraged at the examination to have another shot at it. There are now many more people to whom I am indebted for going above and beyond in digging me out of what felt like, and still feels like, a very deep hole.

Paul Goddard and Steve Blundell have the greatest claim on my gratitude. At a time when I was unable to see the green shoots for fallen trees, they helped put it all in perspective and patiently covered their ears while I gave up on any semblance of professionalism and yelled profanities at their office walls. Over the last seven months, they have given up countless valuable hours in listening, dispensing wisdom, proofreading and distilling their knowledge. They can have derived no reward from it and I do not believe I will ever be in a position to pay them back in kind. Nevertheless, I will do my best with the limited resources available. Others whose help was indispensable include Sonia Contera for AFM measurements and cake, Matt Bristow and Amalia Coldea for letting me loose on their brand-new PPMS sample rotator, Stefano Carretta and Alessandro Chiesa for extending the hand of kindness to a complete stranger, and Craig Topping and Nat Davies for SQUID tips and blather over a Bru.

I would like to redouble my thanks to all my friends and family. Just as I should have been starting the long process of paying off my moral debt for six years of their support, I demanded a loan of six months more. I will not tire you by repeating them all, but three notable names escaped earlier mention by being out of the country. Since arriving, Matthew has kept me in laughs, Morgan has kept the creative spirit alive, and Pete has done perhaps more than anyone in the name of concise and profound wording.

Despite the help of all those I have named, and many I have not, I would surely have given up completely if it wasn't for Lucy. I'm not sure if there's anything I can do to thank her for salvaging the remains of me from the wreckage of my DPhil. I can only promise to try.

It's time for a break. Lucy and I are off for a swim.

CONTENTS

LIST OF FIGURES

LOA

1-D · one-dimensional

2-D · two-dimensional

3-D · three-dimensional

AFM · atomic force microscopy /microscope

AMR · anisotropic magnetoresistance

AMRO · angle-dependent magnetoresistance oscillations

ARPES · angle-resolved photo-emission spectroscopy

^{t}Bu · tertiary-butyl group, $C(CH_3)_3$

Cr_7Zn · $(Me_2NH_2)[Cr_7ZnF_8(O_2C\,{}^{t}Bu)_{16}]$ (see ^{t}Bu)

Cr_8 · $Cr_8F_8(O_2C\,{}^{t}Bu)_{16}$ (see ^{t}Bu)

DC · direct current

DIP · dual in-line package

EBL · electron-beam lithography

EBSD · electron backscatter diffraction

EDX · energy dispersive X-ray spectroscopy

EOS · electron optical system

FIB · focussed-ion-beam

Ga_7Zn · $(Me_2NH_2)[Ga_7ZnF_8(O_2C\,{}^{t}Bu)_{16}]$ (see ^{t}Bu)

IPA · isopropyl alcohol

LCC · leadless chip carrier

LOA · list of abbreviations

MIBK · methyl isobutyl ketone

PL · photo-lithography

RIE · reactive ion etch

RKKY · Ruderman-Kittel-Kasuya-Yosida

SCCM · standard cubic centimetres per minute

SEM · scanning electron microscopy

SMM · single-molecule magnet

SQUID · superconducting quantum interference device

STM · scanning tunnelling microscopy

STS · scanning tunnelling spectroscopy

TI · topological insulator

VPSEM · variable pressure scanning electron microscope

WAL · weak anti-localisation

1

OUTLINE OF THESIS

The work reported in this thesis falls into two quite distinct parts, but a unifying theme is the innovative application of nano- and micro-scale structures to problems of much larger-scale electrical transport measurements. This has resulted in the development of two new techniques that, it is hoped, may yet find much broader application than the few experiments reported here.

Part I relates the development of a new method for printing conducting metal contacts onto crystallites of inorganic materials with dimensions as small as about 10 μm. The intention of this work is that it should enable standard electrical transport measurements, in low temperatures and high magnetic fields, on a very wide range of materials. A great many materials of interest in studies of magnetism, correlated electron dynamics and related phenomena are routinely synthesised as powders, but are not as readily available in larger single crystals. We show here that the individual grains in such powders are typically well-formed crystallites, tens of microns in size—too small for measurement using conventional electrical transport techniques but of very high quality. In developing our new method, we hope eventually to be able to take advantage of the abundance of powder samples of materials for which there exist, as yet, no larger single crystals and thereby enable electrical transport measurements on previously inaccessible systems.

This new method is an application of electron-beam lithography on an unconventional substrate assembly. **Chapter 2** therefore provides a description of the key features of scanning electron microscopy and electron-beam lithography, by way of introduction. **Chapter 3** then presents an investigation of the structure and morphology of crystallites from various representative powder samples of inorganic compounds with layered crystal structures. It also describes the design and ongoing development of our technique for making lithographically patterned electrical contacts on such crystallites. Finally, by way of demonstration, it presents the results of preliminary transport measurements on a crystallite of the layered oxide chalcogenide $Sr_2MnO_2Cu_{1.5}Se_2$.

Part II of this thesis describes a new technique for the investigation of surface transport in 3-D topological insulators. These materials have recently been of intense interest for unusual features of their surface bandstructure, which is predicted to guarantee very good surface conduction due to a locking of the spin and crystal momentum of surface quasiparticles, even when the bulk of the material is a band insulator. To date, transport measurements of this phenomenon have often been hampered by the difficulty of teasing apart the interplay of bulk and surface conduction. Furthermore, whilst previous investigations of the unique spin characteristics of the surface state have often exploited magnetic dopants in an effort to disrupt the surface spin currents, it is difficult to distinguish the magnetic influence of such dopants from their electrostatic effect. In this part of the thesis, we demonstrate our development of a method in which we decorate the surface of a putative topological insulator with two different species from a well-characterised family of molecular magnets. The two coatings have an electrostatically identical

influence on the topological insulator, but differ in that one species carries a spin and the other is spinless. In this technique, the spinless molecule acts as a control, to allow us to cleanly determine the influence of the magnetic component of a scattering potential on transport in the surface state.

Chapter 4 provides a preliminary reminder of a few magnetoresistance techniques that were used in the work described in the following chapters. Hall effect and magnetoresistance measurements will be used in the following chapters to investigate surface and bulk transport in a proposed topological insulator. **Chapter 5** presents a review of the discovery of topological effects in condensed matter physics and of the prediction and discovery of topological insulator materials. Various 3-D topological insulators are discussed for their suitability as subjects of a transport study and SmB_6 is identified as the best candidate system. **Chapter 6** presents details of the structure and magnetic properties of two molecular magnet compounds. It then describes a series of transport experiments on samples of SmB_6 using these molecular magnets, deposited on the samples by thermal sublimation, to demonstrate that a surface conduction channel dominates low-temperature transport and that the surface state momentum relaxation is very sensitive to a spin degree of freedom in the scatterer.

In each part, we report the development of a new method for making transport measurements on interesting systems in condensed matter physics. It is the intention of this work that, with refinement, the techniques outlined here might be of more general applicability than the specific examples we have investigated. The technique for measuring micron-scale crystallites, described in part I, is intended to be of use in studies of a range of different inorganic materials, for which large

single crystals do not yet exist. Similarly, the use of molecular magnets to provide scattering potentials with independent electrostatic and magnetic components, described in part II, may be useful in determining the transport properties of many different topological insulator materials as well as other materials with unusual surface states.

Part I

PRINTED CONTACTS FOR MICRON-SCALE SINGLE-CRYSTAL TRANSPORT MEASUREMENTS

> In spite of modern developments, it is still necessary for the lithographer to be a craftsman… There are so many processes dependent on skill of hand and judgement of eye.
>
> D Cumming on the *Training of Apprentices* [1]

2

ELECTRON MICROSCOPY AND LITHOGRAPHY FOR NANOFABRICATION

This chapter describes some of the well-established experimental techniques that were used in the work recounted in chapter 3. It begins with an introduction to imaging below the resolution limit of visible light with scanning electron microscopy (SEM). It then describes how electron-beam lithography (EBL) uses a modification of the same focussed-electron technology for micro- and nano-fabrication.

Even before Richard Feynman issued his now famous challenge to take advantage of the 'room at the bottom' [2], the rudimentary practicalities of writing micron-scale features with an electron beam had already been established [3]. Nevertheless, nanofabrication techniques are today predominantly the preserve of applications and research in device engineering and remain under-exploited in many branches of solid state physics research. Much of the experimental work reported in the first part of this thesis has involved unconventional applications of micro- and nanofabrication techniques. These have necessitated the development of modifications to more conventional fabrication procedures. To allow the reader to better understand these modifications, there follows a short introduction to the established techniques of scanning electron microscopy and electron-beam lithography, as used in this work. More detail on development of the modified techniques can be found in chapter 3.

2.1 SCANNING ELECTRON MICROSCOPY

Many techniques exist for imaging objects below the resolution limit of visible light but perhaps the most versatile is scanning electron microscopy (SEM). Until its development in the 1930s [4], there had been no very significant improvement in general-purpose microscopic imaging since Hooke had first captivated scientist and non-scientist readers alike with his *Micrographia* [5]. Successive technological developments have refined the scanning electron microscope and today it is a key imaging tool in micro- and nanofabrication, as well as in other areas of the physical and the biological sciences [6]. Because of the complex depth profiles and charging

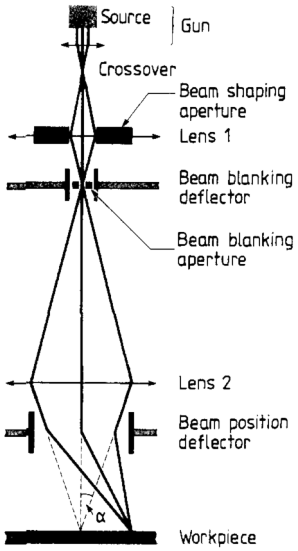

Figure 2.1: Schematic cross-section of the electron optical system of a typical SEM or EBL apparatus. Reproduced from [7].

characteristics of the fabricated structures described in chapter 3, it will be helpful to the reader to have an understanding of the SEM techniques used here.

SEM exploits the short wavelength of moderately high-energy electrons to achieve a resolution limit of order 1 nm, an improvement of two to three orders of magnitude over standard optical microscopy [8, 9]. For the highest resolutions, the electron source is typically the atomically fine tip of a tungsten wire cathode, from which electrons are stripped by field emission. They are then accelerated in an electric field to 1–100 keV through the evacuated column of the electron optical system (EOS), which consists of various apertures, shutters and magnetic lenses. These shape and focus the beam and adjust its stigmation, much like the optics of a light microscope. The shutter and the deflecting lenses can also be used to effectively shut off the beam so that the electron current at the base of the column can be switched on and off. A schematic of a typical such EOS is shown in figure 2.1.

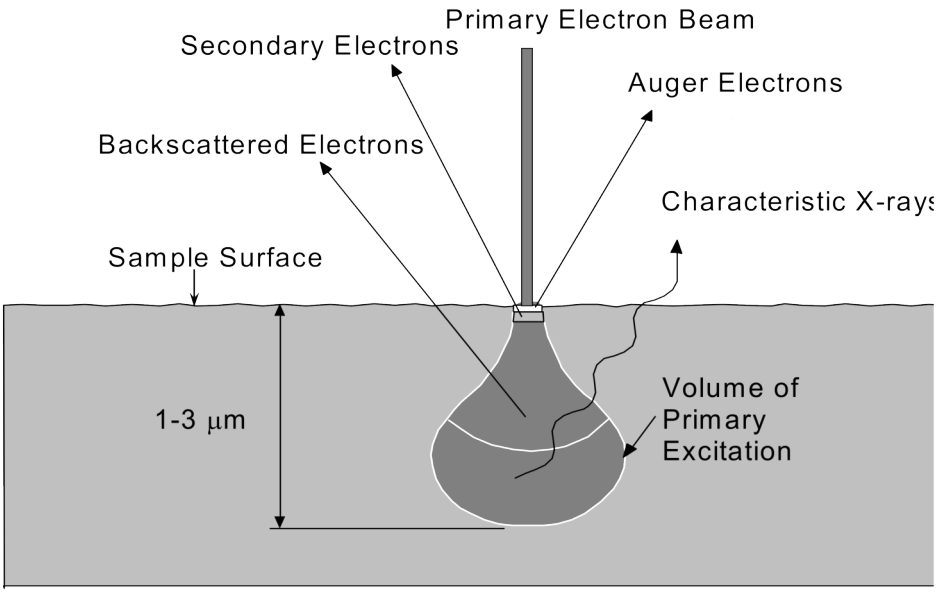

Figure 2.2: Incidence of an electron beam on a thick sample. Backscattered electrons are energetic enough that they can escape from several microns deep within the sample, whereas the less energetic secondary and Auger electrons have a shorter mean free path and can only escape where they are generated within a few nanometres of the surface. X-rays are also generated due to the creation of vacancies in the inner electron shells of atoms in the solid. Adapted from [10].

At the base of the EOS column, the beam enters a sample chamber, which is usually under vacuum, where the object of study is mounted on a translation and rotation stage. When the electron beam strikes the solid object, the incident, or primary electrons undergo various elastic and inelastic scattering processes that produce various forms of radiation [8, 9], illustrated in figure 2.2. In addition to generating bremsstrahlung and cathodoluminescence, some primary electrons are scattered back out of the sample by elastic and near-elastic collisions as deep as several microns within the solid. An appropriate detector can be used to detect these backscattered electrons and either to image the sample or, in the case of a crystalline solid sample, to explore its crystallography by resolving the electron

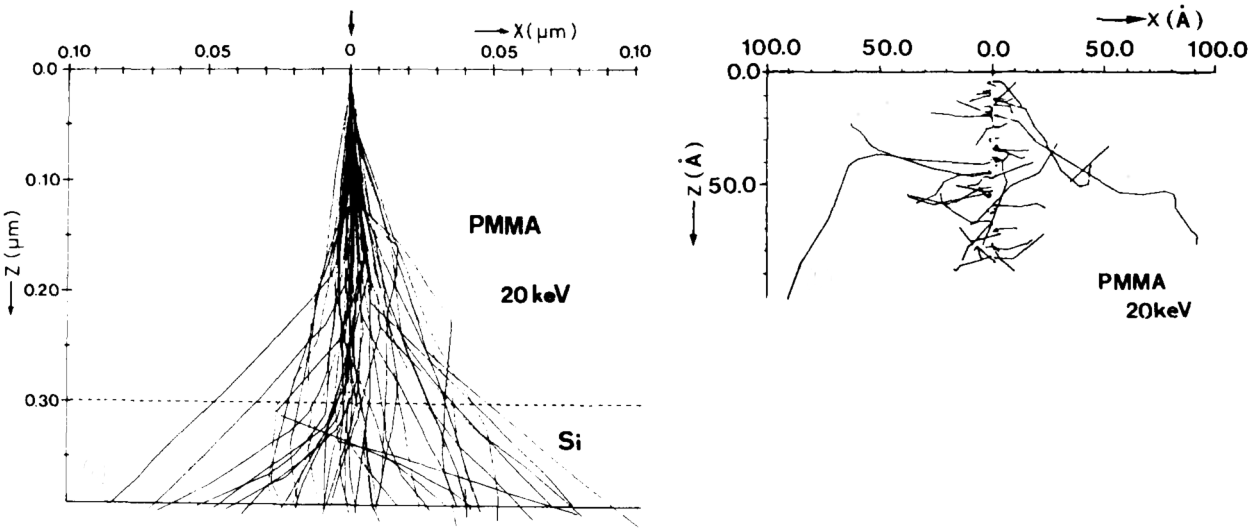

(a) Scattering of primary electrons

(b) Generation of secondary electrons

Figure 2.3: Monte Carlo simulation of the scattering of fifty primary electrons and the generation of secondary electrons when a 20 keV electron beam strikes a solid. The target material is a 300 nm-thick layer of PMMA on silicon. Reproduced from [11].

backscatter diffraction (EBSD) pattern. Important inelastic processes include the creation of so-called secondary electrons by the liberation of an inner-shell electron by the collision of a primary electron with an atom. Secondary electrons have much lower mean energy and mean free path than the scattered primary electrons and so they can only escape the sample where they are generated within a few nanometres or tens of nanometres of the surface. Hence they provide an excellent surface imaging tool with better resolution of topography than backscattered electrons. Secondary electrons are detected using an Everhart-Thornley detector, which gathers the electrons with a positive-charged collector and counts them using a combined scintillator-photomultiplier. Figure 2.3 shows the scattering of primary electrons and the generation of secondary electrons in a silicon sample coated with poly(methyl methacrylate) (PMMA). Using the beam position deflector

(see figure 2.1) to scan the electron beam over the sample surface, the detection of backscattered electrons or, more usually, secondary electrons allows an image of the entire surface to be constructed. Because the electron beam typically has a very high depth of field, very sharp images can be obtained, even where samples have out-of-plane feature heights of order 1 μm.

In addition to high resolution imaging and crystallography, SEM can be used to determine chemical composition with similar spatial precision by means of energy dispersive x-ray spectroscopy (EDX) and Auger spectroscopy [10]. Both techniques rely on the fact that the stimulation of secondary electrons leaves vacancies in the inner electron shells of excited atoms throughout the region excited by primary electrons. An electron filling the vacancy can either emit an x-ray as it relaxes or transfer the same energy to an outer shell electron, which is emitted as an Auger electron. Because, like secondary electrons, Auger electrons must overcome a binding energy to escape the atom, they are qualitatively similar, but with even lower mean energy and shorter mean free path. Hence they can only escape the uppermost few nanometres of the sample. The x-rays, by contrast, can be detected from anywhere within the region of excitation. Both these x-rays and the Auger electrons have energy spectra that are characteristic of a particular electronic structure. Careful analysis of a spectrum can therefore yield a detailed elemental composition of the target.

Because the electron beam continually deposits a negative charge in the sample, this must be dissipated. If it is not, the beam can be deflected by the accumulated potential, which distorts the image and limits the achievable resolution. For this reason, the best results are achieved with conducting samples, which must be electrically connected to ground through the sample stage. Samples which are not

sufficiently conducting need either to be coated with a thin conducting layer, such as sputtered gold, or imaged with a variable pressure scanning electron microscope (VPSEM) [9]. In the latter, the sample space and the EOS column are separated by two or more small, pressure limiting apertures, which allow differential pumping of the chambers. In this way, an atmosphere of a certain gas, often water vapour, can be maintained around the sample, while the EOS remains at high vacuum. Ionised gas molecules in the sample space provide a discharge path for the deposited electrons in the sample.

2.2 ELECTRON-BEAM LITHOGRAPHY

Some materials, when exposed to an electron beam, undergo chemical changes which can be exploited to perform electron-beam lithography (EBL) on a substrate [7]. Materials which harden on exposure to the electron beam and become more difficult to remove from the substrate, while the unexposed parts are more easily washed away with a developer solvent, are referred to as negative-tone resists. Materials which become easier to remove after exposure are known as positive-tone resists. Although in SEM the electron beam is scanned across the entire sample surface, the same EOS can be used to direct the electron beam according to a specific pattern. By patterned exposure of a resist and removal of the susceptible parts, one can create a mask, through which other materials may be deposited. The mask, and any material deposited on it, may subsequently be removed by a solvent more aggressive than the developer in a process called 'lift-off'. All that remains of the deposited material is the unmasked portion, i.e. a negative of the mask pattern. If

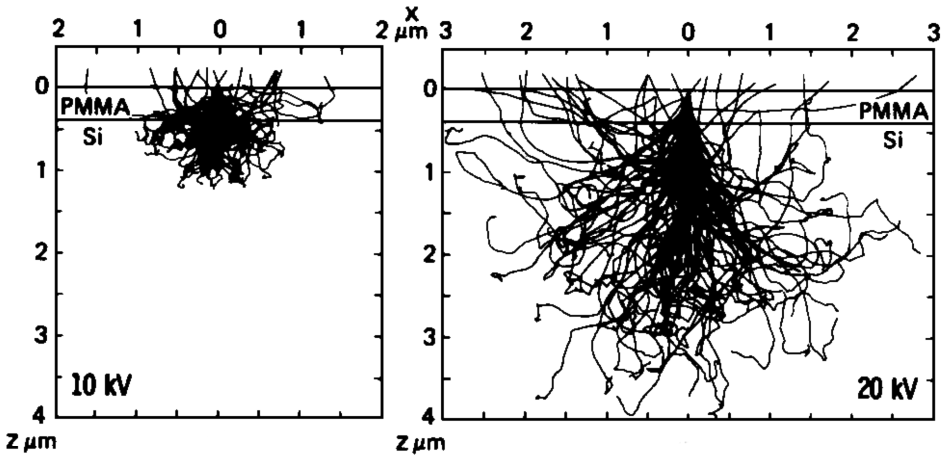

(a) 10 keV beam (b) 20 keV beam

Figure 2.4: Monte Carlo simulation of the scattering of 100 primary electrons when electron beams with different incident energies strike a solid. The target material is a 400 nm-thick layer of PMMA on silicon. Reproduced from [12].

the deposition of the coating material results in reasonably uniform coverage of all surfaces, as in sputtering, lift-off tends to be more difficult than if the deposition is directional, as in thermal evaporation. This is because coating the side-walls of the developed resist can prevent a clean break between the masked and unmasked portions of the deposited material.

The resolution of EBL is limited by more than just the resolution of the EOS. Because of the spread of backscattered and secondary electrons within the resist, written features show a pronounced bleed around the path of the electron beam. Figure 2.4 shows how a lower electron beam energy may counter-intuitively result in more energy dumped in the resist layer. Lower beam energies often have broader written features as the spread of scattered electrons is more spherical and less like the teardrop shape of higher beam energies. A commonly used positive-tone resist is poly(methyl methacrylate) (PMMA) [13–15], which affords a very high max-

imum resolution of tens of nanometres when written with a beam of 30–100 keV. PMMA is available in several different polymerisations and dissolved in chlorobenzene or anisole. A commonly used technique is to employ bi-layer PMMA—a substrate is coated with a layer of PMMA with a lower molecular weight (i.e. shorter polymers) followed by a layer with a higher molecular weight (longer polymers). When developed, the lower layer is more readily dissolved than the upper layer and so an under-cut develops at the edges of the pattern. When other material is subsequently deposited onto the patterned PMMA, this helps to maintain a separation between the masked and unmasked material, thus aiding lift-off, particularly where sputtering is the deposition method.

The work described in chapter 3 has involved the development of a specialist application of EBL to samples on non-standard substrates. This technique required the imaging by SEM of electrically insulating substrates. As such, various discharge methods were explored, including a coating of conducting polymer, a sputtered gold coating, and the use of VPSEM. The work also involved the use of PMMA resist and careful optimisation of beam energy to achieve the best possible resolution. Both $495\,\mathrm{kg\,mol^{-1}}$ and $950\,\mathrm{kg\,mol^{-1}}$ polymerisations of PMMA were used, dissolved 8 % by weight in anisole.

3

ELECTRICAL TRANSPORT MEASUREMENTS ON MICRON-SCALE SINGLE CRYSTALS

The synthesis of a great many materials of interest to condensed matter physicists usually involves the creation of powder samples consisting of small crystallites, tens of microns in size. Such samples are too small for conventional single-crystal transport measurements and so larger crystals must be grown, which is often difficult and time-consuming. This chapter details the development of a novel procedure that instead aims to permit transport measurements on the small crystallites that can easily be obtained from a typical powder. The structural and morphological characteristics of such crystallites is explored, and a technique proposed for making electrical contacts on a single crystallite by means of an unconventional application of electron-beam lithography (EBL). Details of the ongoing development of the technique are reported, along with some early results of its use in simple transport experiments.

Chapter 2 details some of the established fundamentals of nanofabrication and EBL. A passing familiarity with these techniques is assumed here and, if unfamiliar with them, the reader is referred to sections 2.1 & 2.2 for an introduction.

3.1 MOTIVATION

In the mid-1980s, the celebrated discovery of superconductivity at unprecedentedly high temperatures in certain cuprates [16–18] reinvigorated interest in the study of superconductors. Since then, much work in the study of correlated electron systems has been preoccupied with highly anisotropic systems. In common with the cuprate superconductors, many other unconventional superconductors have a layered crystal structure, with the resultant dynamics of the charge carriers being quasi-two-dimensional [19].

To understand such systems, it is key to be able to resolve the anisotropy of their physical properties. Ideally, one measures single crystal samples. In the case of an electronic transport measurement, electric and magnetic fields can then be applied along different axes in order to investigate the ways in which the material's transport properties depend on orientation. In practice, however, the chemical synthesis of such compounds often yields a powder sample—an amalgam of small crystallites in random orientations. Synthesis is often done by sintering [20, 21]: the reagents are ground to a powder to increase the exposed surface area, mixed, and heated in a furnace to sufficient temperature that the ions become mobile and the desired phase becomes thermodynamically accessible. Like the reagents, the resulting product is a powder, composed of crystallites which may be of the order of microns or tens of microns in size. In contrast to single-crystal measurements, a great deal of information about the anisotropy of the physical properties is lost in measuring a powder sample.

Conventional techniques for DC transport measurements usually require wires to be fixed to a material by hand using solder or a conducting adhesive. For this to be possible, samples must typically be several hundreds of microns or even millimetres in size. The limitation is the precision of human manipulation. Unfortunately, this rules out the measurement of many samples as synthesised. The growth of larger crystals is an art in itself and may introduce additional challenges in the form of defects and dislocations in the crystal structure [22, 23]. Some systems are not readily amenable to growth and this limitation can be a barrier to better understanding new systems. Even when there is no structural obstacle to crystal growth, new materials are very often first synthesised as a powder and only grown into larger crystals after some months or years of research, delaying their accessibility for transport measurements. For example, in the case of the cuprate superconductors, a great many systems were synthesised rapidly following the discovery of the first high-temperature superconductor [24] but, in each case, the determination of methods to produce good-quality single crystals took several years and encountered numerous obstacles [23, 25]. The tiny crystallites in such a powder, however, are often very good-quality single crystals, as illustrated in section 3.3. With this in mind, it would be desirable to develop a reliable method for making contacts for electronic transport measurements on such small crystals without the need to grow larger samples.

3.2 EXISTING TECHNIQUES

Attempts have been made before to perform DC transport measurements on very small crystals. In 2001, Kim *& al.* [26] found that, in trying to grow thin films of magnesium diboride, they could instead grow very uniform hexagonal platelet-like crystals with very clean and flat surfaces normal to the *c*-axis. These crystals were 20–120 µm in diameter and 2–10 µm in thickness. By fixing the samples to a substrate using a photoresist as an adhesive, metal contacts were fabricated on the surface using photo-lithography (PL). This method reportedly yielded contact resistances smaller than 2 Ω. Though it seemed to work extremely well and allowed for good measurements of the resistivity of MgB_2, there seems to be no reported application of this technique to other samples.

Another method, rather more involved and technically difficult, was demonstrated by Moll *& al.* [27] in measurements, including pulsed magnetic field measurements, to determine the critical current densities and magnetic-field dependence of resistivity in single crystals of the iron arsenide superconductor SmFeAs(O,F). The authors used a combination of focussed-ion-beam (FIB) milling, to cut the samples to shape, and FIB-induced chemical vapour deposition of platinum, to make conducting contacts. In this way, they were able to carve elaborate sample geometries from a single crystal and simultaneously measure resistivity in the *a*-*b* plane and in the *c*-direction. Though extremely elegant, the technical sophistication of this technique makes it difficult to apply quickly and repeatedly to several samples.

It would clearly be desirable to develop a generic method to address the inaccessibility of typical as-synthesised sub-50 μm single-crystal samples for transport measurements. A method that can be used reliably for a wide range of systems and sample geometries would enable single-crystal measurements on a host of systems currently beyond the immediate reach of the conventional methods.

3.3 DERIVING SINGLE CRYSTALS FROM A POWDER

The sample materials studied throughout this chapter were all sintered powders, provided by Simon Clarke of the Inorganic Chemistry Laboratory at the University of Oxford and his students Jack Wright and Genevieve Allcroft, except the samples of $La_{1.85}Sr_{0.15}CuO_4$ which were small shards broken from a single crystal provided by Dharmalingam Prabhakaran of the Clarendon Laboratory.

In order to determine whether it would be possible to develop a method for measuring the transport properties of micron-scale crystallites derived from a powder, it is important to understand the typical characteristics of their morphology. We used SEM to inspect individual crystallites, and x-ray diffraction to determine their structure and to check the quality of the crystallites and the typical incidence of crystal twinning. Figure 3.1 shows examples of typical samples of a variety of materials. The key characteristics common to all these materials are that they show well defined faces and have a tendency to form platelet-like crystals with diameters of tens of microns and thicknesses of order 1 μm. With an appropriate diffractometer, x-ray crystallography can be performed, even on such small crystallites. We used an Agilent SuperNova diffractometer to show that the crystals with the

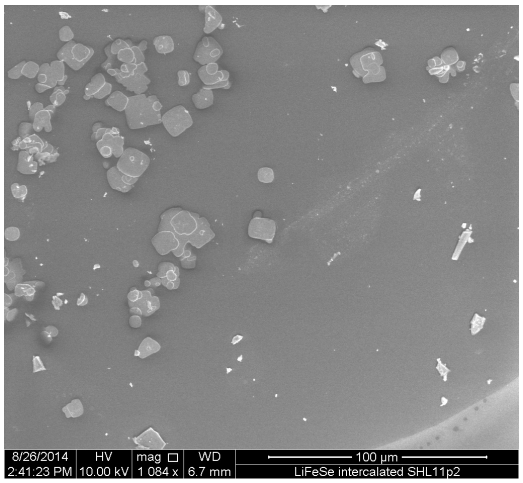

(a) Powder of LiOHFeSe crystallites

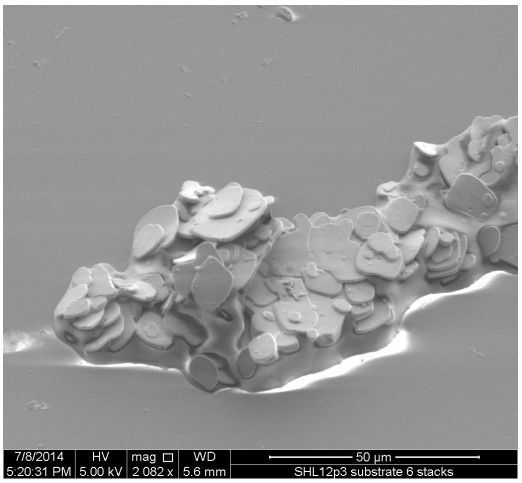

(b) Agglomeration of LiOHFeSe powder

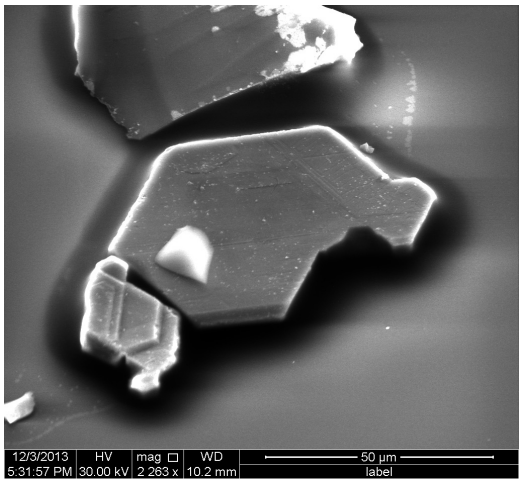

(c) FeSe crystallite

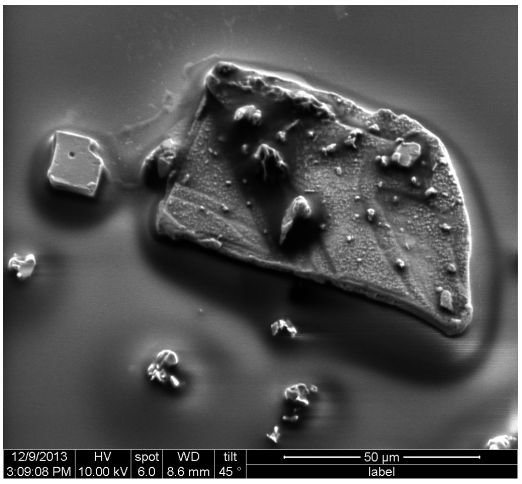

(d) $FeSe_{1-x}Te_x$ crystallite

Figure 3.1: SEM images of typical crystallites of various materials, obtained from powder synthesisis. In each case, the crystallites have been scattered on an amorphous quartz substrate and fixed to it with a photoresist as an adhesive.
a: A powder of LiOHFeSe crystallites, viewed from above, showing their uniformly platelet-like morphology.
b: An agglomeration of LiOHFeSe powder, viewed obliquely, clearly showing the thickness of the crystallites and their clean surfaces.
c: A crystallite of FeSe, viewed obliquely, with visible terraces, indicative of the layered structure.
d: A crystallite of $FeSe_{1-x}Te_x$, with $x \approx 0.02$, viewed obliquely, with clearly visible terraces and surface contaminants, most likely unincorporated tellurium.

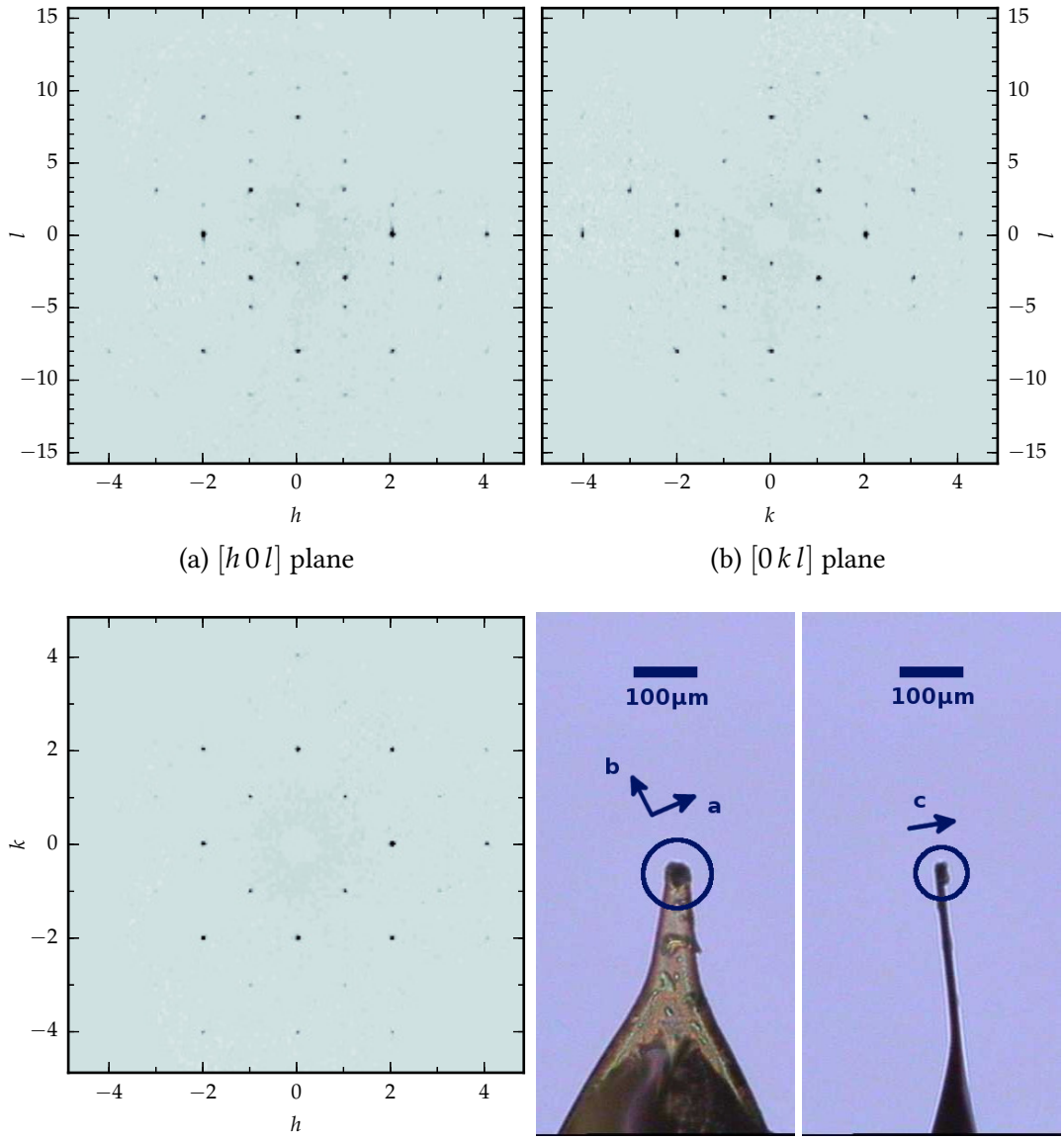

(a) $[h\,0\,l]$ plane (b) $[0\,k\,l]$ plane

(c) $[h\,k\,0]$ plane (d) Sample (top) (e) Sample (side)

Figure 3.2: Determination of the structure of a single crystallite of $Sr_{0.65}Na_{0.35}Fe_2As_2$. a–c: X-ray diffraction pattern, displayed as three reconstructed $15.7\,\text{Å}^{-1} \times 15.7\,\text{Å}^{-1}$ slices through reciprocal space, centred on $[0\,0\,0]$. The space group is $I4/mmm$ [28], with lattice parameters $a = (3.8890 \pm 0.0004)$ Å and $c = (12.587 \pm 0.004)$ Å. d–e: The platelet-like sample (circled), typical of this material, taken from a powder and mounted, lying flat on a kapton support, for x-ray diffractometry. Approximate sample dimensions in the *a*-*b* plane are $25\,\mu\text{m} \times 25\,\mu\text{m}$. Crystal axes are shown.

cleanest and most regular appearance under SEM do indeed show excellent crystallinity with minimal twinning. The diffraction patterns from one such crystallite are shown in figure 3.2. The material, $Sr_{0.65}Na_{0.35}Fe_2As_2$, is representative of many such layered compounds. The Bragg peaks are perfectly isotropic in the *h*-*k* plane (figure 3.2c), with broadening barely larger than than the instrumental minimum and with no evidence of twinning. There is slightly more broadening along the *l*-axis (figures 3.2a & 3.2b). This may represent a higher incidence of stacking faults between the *c*-normal layers, as the inter-layer bonding is weaker than the intra-layer bonding, but it is not sufficient to indicate significant twinning.

The high quality of these clean and well-formed crystals would make them excellent candidate samples for electrical transport measurements, were it not for their small size. This motivates the design of a method to exploit these previously inaccessible samples.

3.4 REQUIREMENTS OF A NEW METHOD

Drawing inspiration from the MgB_2 work of Kim *& al.* [26], a lithographic process for printing contacts on the top surface of a sample has the promise of almost universal applicability to inorganic samples (the application of such a method to samples of most organic materials is probably precluded by the use of organic solvents in micro- and nano-lithography). The requirements and challenges of such an unconventional method are detailed below, and in sections 3.6, 3.7 & 3.8 we demonstrate how these requirements have been addressed in the development of our new technique. We have explored this promising method in some detail and

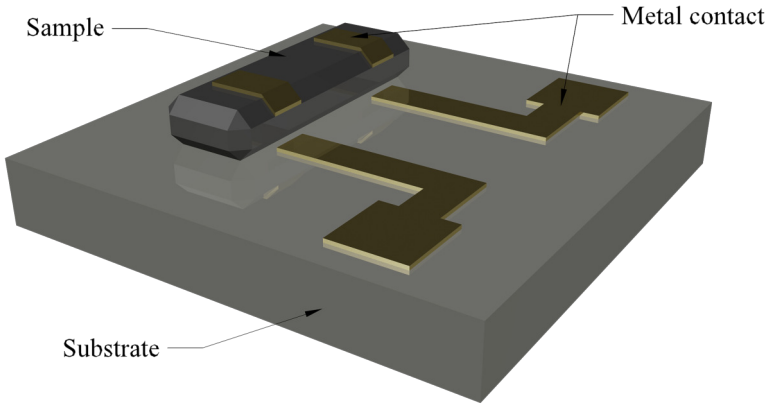

Figure 3.3: A challenge in lithographic patterning of contacts on small crystals. Patterning crystallites, such as those obtained from a powder, is hampered by the sample thickness. It is difficult to pattern a layer thick enough to avoid broken contacts at the sample edge.

it appears that very few obstacles now remain to its routine application. Section 3.10 details the few problems that are outstanding.

3.4.1 *Space constraints*

In order to permit measurements of samples in high magnetic fields at low temperatures, it is desirable to keep the overall dimensions of the mounted sample assembly small, so that it might fit a wide range of measurement probes in various cryostats. In order to use the equipment available in the Clarendon Laboratory, this effectively constrains the assembly to fit within a space of approximately $10\,\mathrm{mm} \times 10\,\mathrm{mm} \times 5\,\mathrm{mm}$. This means that the substrates on which the sample is

fixed must be quite small. In spin-coating resists onto the substrate for lithography, the small size of the substrate reduces the centrifugal effect of the spin-coater. One consequently risks large edge-beads and rippling of the surface of spin-coated resists.

3.4.2 *Lithography on a sample crystallite*

Although, as seen in figure 3.1, the surfaces of powder crystallite samples can be very clean and uniform, the overall shape and size of such crystals is very variable. Using conventional micro- and nanofabrication techniques such as PL and EBL to create printed metal patterns usually requires a very flat substrate surface. Substrates that are not flat limit the resolution of the lithographic patterning—in EBL, focussing is compromised due to the substrate surface departing from the focal plane of the electron beam optics; in contact or proximity PL, imperfect contact or variable separation between mask and substrate leads to diffractive blurring at the edges of features. This may limit the smallest written feature size achievable with lithographic patterning.

Furthermore, and crucially, vertical discontinuities on the substrate, such as an affixed sample, would lead to breaks in a deposited metal layer (see figure 3.3). It is consequently much more challenging to incorporate a crystallite, such as those illustrated in figure 3.1, into printed device circuitry than to print a measurement device onto an epitaxially grown film or epitaxially grown crystallites, such as the MgB_2 samples of Kim *& al.*[I].

3.5 PROPOSED SOLUTION

To resolve the challenges of lithographic patterning of non-planar samples, we have explored an innovative method that involves the encapsulation of a sample crystallite in a composite substrate, in such a way as to permit conventional planar lithographic patterning. A sample is enclosed in a thick layer of negative-tone photoresist (i.e. resist that cross-links and hardens on exposure) on a substrate that is transparent to UV light. The photoresist is exposed to UV radiation through the substrate from below. The small region of resist on top of the sample is shaded by the sample itself and is therefore not exposed and is easily removed by the developer solvent, leaving the upper surface of the sample uncoated. By adjusting the resist thickness, and the exposure and development parameters appropriately to the sample thickness, one can produce an assembly in which the top surface of the photoresist and the bare upper surface of the sample are sufficiently coplanar as to allow lithographic patterning of measurement circuitry on the sample. This proposed solution is illustrated in figure 3.4.

To this end, we chose to use readily available fused quartz substrates, which are easily diced to appropriate sizes (in this work, the substrate dimensions were typically $2.5\,\text{mm} \times 2.5\,\text{mm} \times 0.35\,\text{mm}$) and display ample trasmission in the UV region of the electromagnetic spectrum [29] to permit exposure of the photoresist. The resist we have chosen to use is EPON SU-8 [30, 31], primarily because, after exposure and development, it is extremely hard, has very low electrical conductivity, shows very good adhesion to a substrate and is largely impervious to the solvents typically used in EBL. These properties make it an ideal resist to form part of the

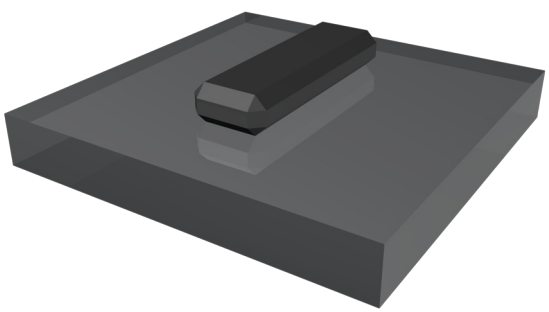

(a) Sample on transparent substrate

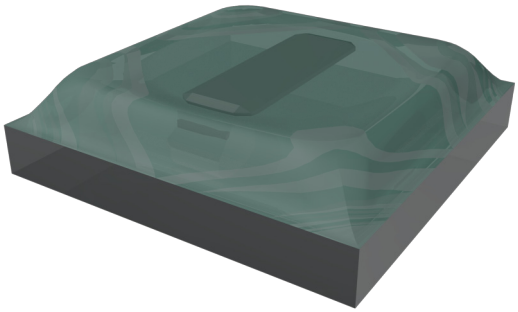

(b) Sample enveloped in resist

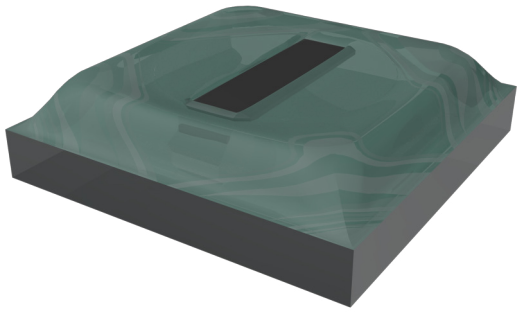

(c) Resist developed/etched to reveal sample

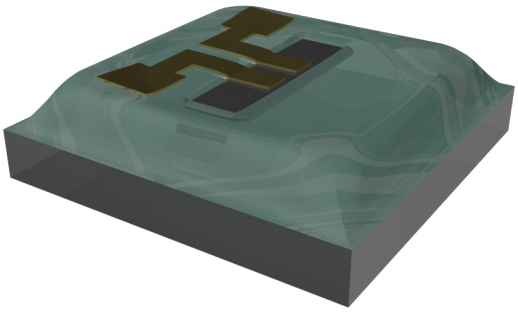

(d) Sample patterned with metal contacts

Figure 3.4: Schematic of the proposed solution to the problem of lithographic patterning of contacts on small single-crystal samples. The sample dimensions have been exaggerated for clarity. a: A sample is fixed to a substrate that is transparent to UV light. b: The sample is enveloped in a photoresist, which is hardened by UV exposure from beneath, through the transparent substrate. c: The sample masks part of the resist, which is removed by the developer, leaving the top sample surface uncoated. The base substrate and the resist together now form a composite substrate enclosing the sample. Further etching ensures a reasonably continuous upper surface where the sample and resist meet. d: The relative continuity of the top surface of the assembly permits lithographic patterning of metal contacts on top of the sample and resist.

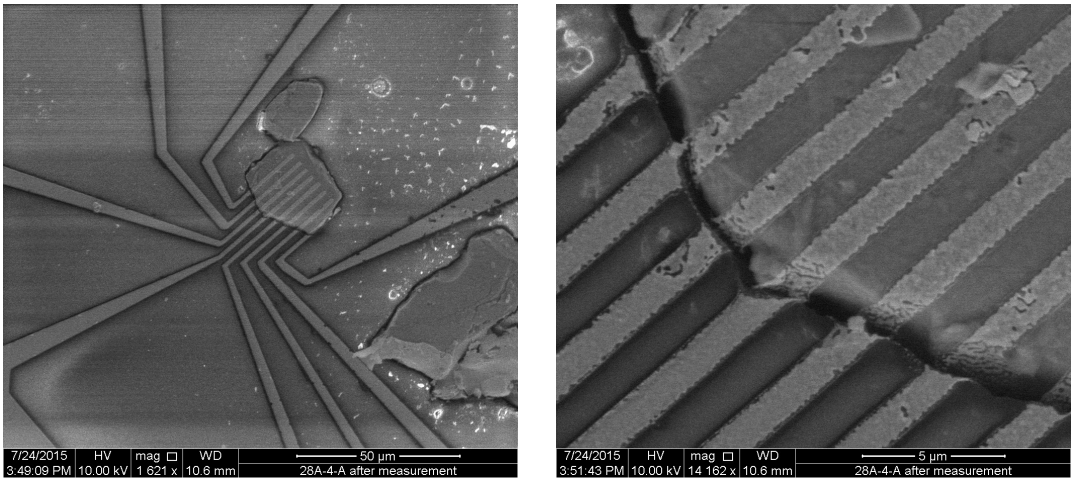

(a) Lithographically printed tracks (b) Detail

Figure 3.5: Example of a height mismatch between upper surface of the composite substrate and the top of a sample. The sample is $Sr_{0.65}Na_{0.35}Fe_2As_2$. The photoresist has been made too thick for the sample, such that there is a break in the deposited metal tracks at the sample edge.

proposed composite substrate assembly. It also shows minimal out-gassing in a vacuum, making it well suited to cryogenic measurements [32].

3.5.1 *Practical details of the photoresist exposure*

The specific resist formulation used throughout was Microchem SU-8 2025, which is a solution of SU-8 in cyclopentanone that can be deposited by spin-coating in a layer with thickness in the range 20–80 µm, dependent on spin speed [33]. Diluted with additional cyclopentanone, the resist can be deposited in a thinner layer. A typical procedure was to mix SU-8 2025 and cyclopentanone in the ratio 1 : 1 by volume to achieve layers in the thickness range 1–20 µm, with a spin speed of order 3000 rpm. The exact speed was adjusted for each different batch of sample powder, according to the typical thickness of crystallites in the batch. Resist thickness

measurements are detailed in section 3.8.1 below. The result of using a resist layer with a depth poorly matched to the sample thickness is shown in figure 3.5.

Before coating with resist, a bare quartz substrate is first subjected to an oxygen plasma etch to remove surface contaminants and ensure good adhesion of the resist to the substrate. Once the substrate has been coated with SU-8 to an appropriate thickness, a dusting of sample crystallites is scattered onto the top surface of the uncured resist. By introducing a single droplet of cyclopentanone (the approximate volume of the eye of a UK size 8/metric size 60 sewing needle is adequate), which diffuses through the deposited resist layer, reducing the viscosity and surface tension, the crystallites become immersed and subsumed in the resist puddle. Alternatively, the powder sample can be mixed with the dilute resist, agitating in an ultrasonic bath to ensure good dispersion of the crystallites, before spin-coating the substrate. In either case, the curing parameters closely follow the recommended values prescribed in the manufacturer's specifications [33], with appropriate adjustments to account for the resist thickness.

Because UV exposure equipment designed for conventional PL is designed to illuminate the masked substrate from above, it was necessary to use an alternative light source for the desired exposure from below. We used a Mega Electronics LV202-E UV exposure unit, which is designed for basic photo-etching of printed circuit-board. It provides a broad UV spectrum with a nominal intensity of $25\,\mathrm{W\,m^{-2}}$. The SU-8 exposure dose D, as a function of resist thickness d, is $D = \frac{5d}{3} \times 10^7\,\mathrm{J\,m^{-3}}$, hence the exposure time $t = \frac{2d}{3} \times 10^6\,\mathrm{s\,m^{-1}}$. A $6\,\mu\mathrm{m}$-thick resist layer, which was found to be adequate for most powders, therefore only requires a four-second exposure.

Standard development of the SU-8 is performed in 1-methoxy-2-propyl acetate as per the manufacturer's recommendations [33], halted with an isopropyl alcohol (IPA) rinse, and followed by an oxygen plasma etch to remove development residue. The etcher used was a Polaron PT7160 plasma barrel etcher with the following parameters—etcher power: 100 W; etcher frequency: 13.56 MHz; oxygen pressure: ∼0.5 mbar; etch time: 90 s.

3.6 CHALLENGES IN PERFORMING ELECTRON-BEAM LITHOGRAPHY

At the outset, certain aspects of this sample preparation technique were anticipated to present complications in the subsequent lithographic patterning of the sample. Whereas conventional EBL is typically performed on very flat substrates that are sufficiently electrically conducting to drain the charge deposited in the substrate by the electron beam, the peculiarities of our method require special adaptation.

3.6.1 *Countering charge accumulation*

After embedding crystallites in the composite substrate, it is necessary to image the assembly in order to determine accurately the position of a target crystallite and to design a pattern of metal contacts to fit. Due to the high resolution required, SEM is the most appropriate imaging tool. Although the high resistivity of the quartz and SU-8 is desirable for preventing a short circuit in the transport measurements, it means that exposure to the electron beam causes the substrate to accumulate charge and the image to be distorted. It is not desirable to intro-

duce a conducting surface layer because this may contaminate the sample/substrate surface before EBL and so, instead, a VPSEM was used (see section 2.1). Using a FEI Quanta Inspect S VPSEM with accelerating voltages between 1–30 kV and a beam current of 1 nA, a 0.6 mbar atmosphere of water vapour was found to be sufficient to permit adequate imaging, as shown in the many micrographs in this chapter, such as in figures 3.1 and 3.7.

Once imaged, the sample and substrate are coated in an EBL resist. During the EBL exposure, it is again necessary to drain the deposited electron charge. We compared various conducting coatings, which are deposited on top of the EBL resist before exposure and removed before development: a spun coat of Showa Denko ESPACER (a conducting polymer, removed with water), a sputtered layer of aluminium (removed with an aqueous solution of sodium hydroxide) and a sputtered layer of gold (removed with an aqueous solution of iodine and potassium iodide). The best results were obtained using a 10 nm gold discharge layer, removed by a 30 s immersion in a solution of I_2 : KI : H_2O in the ratio 1 g : 4 g : 40 ml, halted by rinsing in de-ionised water.

3.6.2 *Patterning the uneven surface*

In spin-coating viscous resists onto a substrate, one usually observes an accumulation of excess resist pooling near the edges of the substrate, known as the edge-bead. In this case, due to the small substrate size, the edge-bead of the SU-8 photoresist will cover a significant fraction of the substrate surface. The consequent defocussing effect on the EBL pattern limits the reliable minimum feature

size. In practice we found that features much smaller than 0.5 µm were not consistently realisable. Samples and contact patterns therefore had to be chosen carefully to take this into account.

In addition, the presence of sample crystallites in the resist layer will create a distorted and uneven surface. This motivated the choice of sputtering to deposit the metal for the contact pattern, over evaporative deposition. Although we anticipated this causing difficulties in the lift-off of surplus metal, it has benefits for continuity on and adhesion to the substrate/sample surface and helps to iron out any small discontinuity that might still exist between the top surfaces of the sample and resist.

3.6.3 *Practical details of the EBL*

Various thicknesses and formulations of PMMA and compositions of deposited metal were tested to determine the best resolution and lift-off characteristics. Because the deposited metal was sputtered, bi-layer PMMA was expected to provide better lift-off than a single layer of resist (see section 2.2). Counter-intuitively, bi-layer PMMA (495 kg mol^{-1} and 950 kg mol^{-1} molecular weight) actually gave very poor lift off, even when each layer was 500 nm thick and the deposited metal layer was only 20 nm thick. By contrast, a single 500 nm layer of 495 kg mol^{-1} PMMA gave good lift-off even for much thicker layers of metal. Figure 3.6 shows the cleaner cut in the metal coating at the pattern edge in the case of single-layer PMMA and bi-layer PMMA. We do not understand the reason for this, though it may be due to excessive generation of secondary electrons close to the top surface of the resist

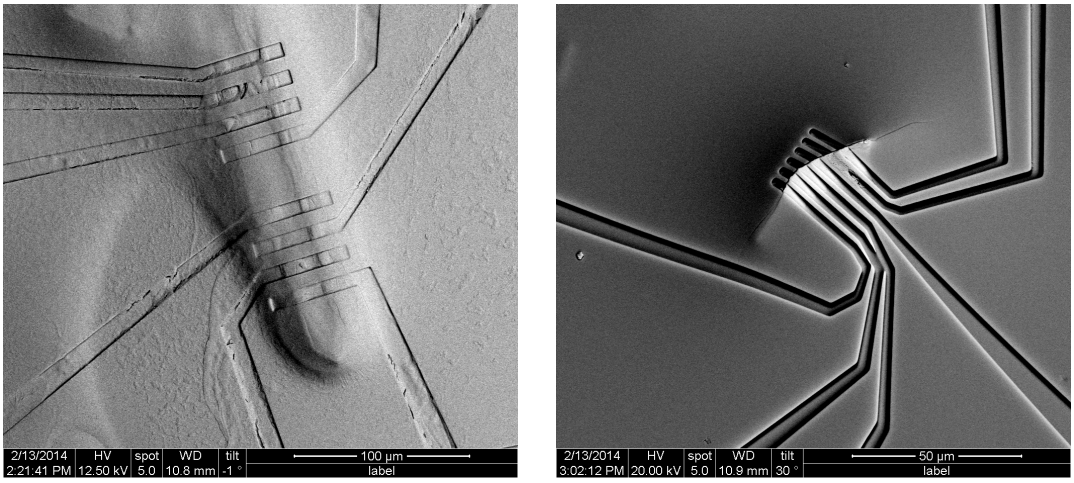

(a) Poor separation of sputtered metal

(b) Good separation of sputtered metal

Figure 3.6: Good and bad examples of post-EBL deposition of metal. a: A large rod-like crystallite of β-FeSe (visible in outline), after EBL patterning with eight contacts and deposition of sputtered metal, but before lift-off. Bi-layer PMMA was used and there is an incomplete break in the metal at the pattern edge. Subsequently, lift-off resulted in the ripping and removal of the metal contacts. b: A crystallite of $La_{1.85}Sr_{0.15}CuO_4$ (one edge visible in outline), similarly patterned with a comb of eight contacts, identically coated with metal and again pictured before lift-off. In this case, 495 kg mol^{-1} PMMA alone was used and there is visibly better separation of metal at the pattern edge. Lift-off in this case was successful.

as the electron beam interacts with the discharge layer, leading to overexposure of the upper layer of PMMA in the bi-layer structure, relative to the lower layer.

A good compromise between resolution and exposure time was achieved with an electron beam accelerating voltage of 30 kV. The optimum electron beam dose for a single 500 nm layer of 495 kg mol^{-1} PMMA with a 10 nm gold discharge layer was (1.8 ± 0.1) C m^{-2}.

The developer used throughout to remove exposed PMMA was a mixture of methyl isobutyl ketone (MIBK) and IPA in the volumetric ratio MIBK : IPA of 1 : 3. Development consisted of immersion in this mixture for 45 s and then a rinse in IPA, followed by an oxygen plasma etch, exactly as per the development of SU-8 (section 3.5.1 above). Metal was deposited through the patterned mask by sputtering 70 nm of gold on a 15 nm titanium or chromium binding layer. Lift-off was performed by prolonged immersion in acetone. Agitation in an ultrasonic bath was found to be unhelpful since it tended to shatter the SU-8 layer underneath, however a gentle teasing of the edges of the sputtered metal with an acupuncture needle seemed to promote a clean lift-off. Figure 3.7 shows a sample embedded in the composite substrate, before and after patterning with titanium/gold contacts.

3.7 MEASUREMENT

To perform transport measurements on a sample prepared in this way, the substrate is mounted, using a small amount of dilute GE varnish, in a Kyocera PB-60962-A-01 16-pin ceramic LCC. The lithographically patterned gold leads connect the sample to larger bond pads on the substrate. These are connected to the LCC by hand using

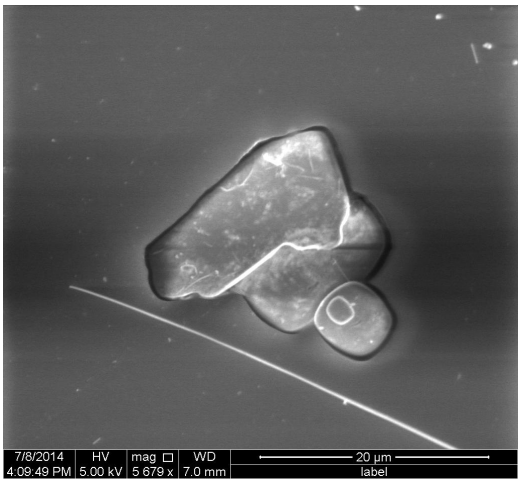

(a) Samples embedded in SU-8

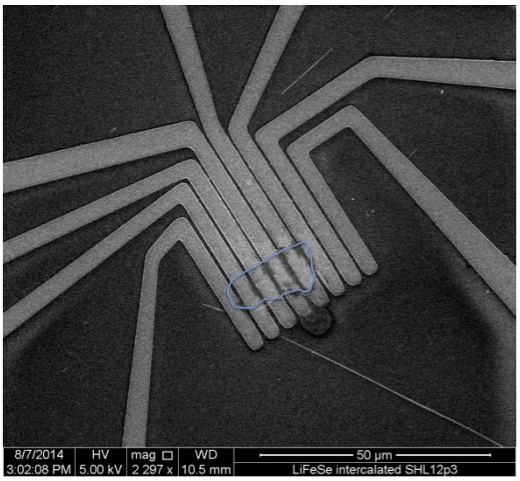

(b) Sample patterned with contact leads

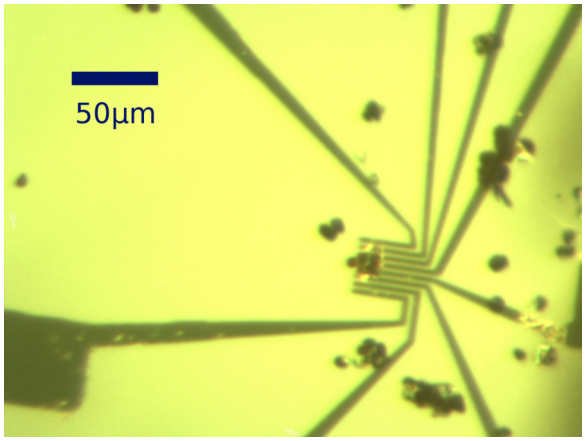

(c) Optical image of same sample

Figure 3.7: Example of patterning an embedded crystallite with contact leads.
a: A cluster of typical platelet-like samples of LiFeSe fixed in SU-8 with the top surface exposed.
b: The same sample after patterning with titanium/gold. The largest crystallite (its outline highlighted in blue) has been patterned for four-wire resistance measurement, with extra contacts for redundancy.
c: An optical micrograph of the sample, as imaged in b, showing other embedded samples.

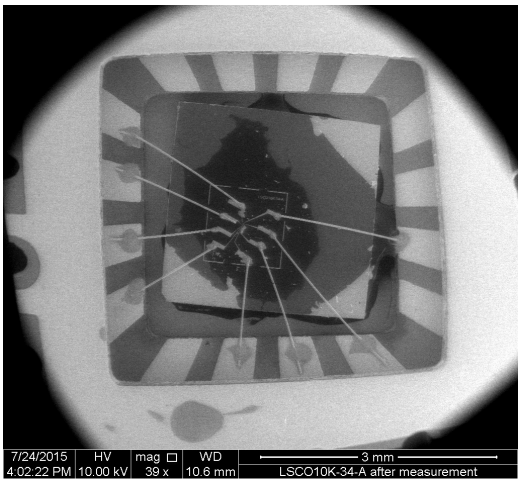

(a) Finished assembly mounted in a LCC

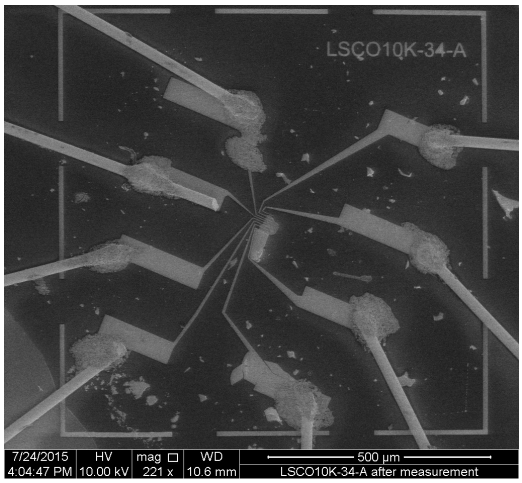

(b) Overview of EBL-patterned area

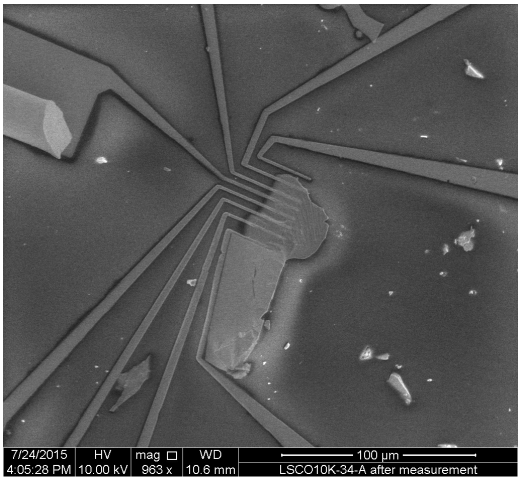

(c) Detail of tracks leading to sample

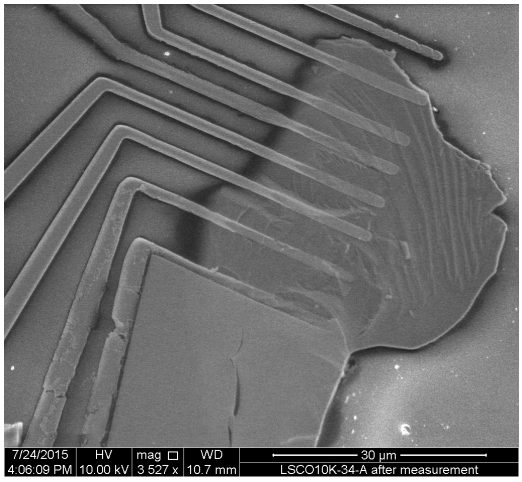

(d) Detail of sample surface

Figure 3.8: $La_{1.85}Sr_{0.15}CuO_4$ held in a finished substrate assembly and mounted in a LCC for measurement. a: The LCC, with sixteen gold contact pads around the central recess. Eight of the pads are connected to the substrate surface with lengths of 25 µm-diameter gold wire, fixed at each end with silver epoxy.
b–d: The wires, bonded to the printed gold pads on the surface of the composite substrate. Patterned gold leads connect each pad to the sample in the centre. The sample does not show clean facets because it has been crudely cleaved from a larger sample, rather than selected from a powder.

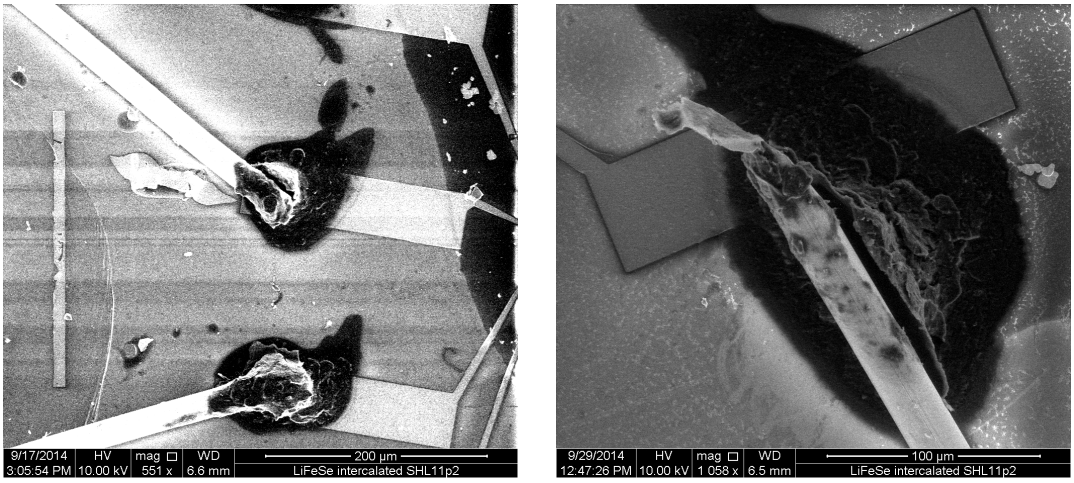

(a) Two carbon paste wire bonds (b) A carbon paste wire bond

Figure 3.9: Carbon paste wire bonds on the patterned substrate assembly after thermal cycling. Both substrate assemblies pictured here were subjected to slow cooling to 77 K and slow warming to room temperature. The contact in (b) and the upper contact in (a) have both broken due to differing the thermal expansivities of the gold wire and the quartz/SU-8 substrate.

25 µm gold wire and Epotek H20E-LV conducting silver epoxy. Ultrasonic ball- and wedge-bonding of gold wire was found to be impossible. Neither ball nor wedge bonds could be made to hold on the patterned contact pads on the substrate. This may be either due to the SU-8 not being hard enough or because there is insufficient adhesion between sputtered titanium/gold and chromium/gold and SU-8 prepared in this way.

Figure 3.8 shows a complete assembly. Once wired in this way, the LCC can then be mounted on a cryostat insert fitted with a push-fit socket appropriate for low-temperature measurements. Because the sample/substrate assembly consists of many different materials with different expansion coefficients, the strength of the conducting epoxy is essential. Connections made with softer conducting adhesives such as silver paint or graphite paste were found to break on cooling to low temper-

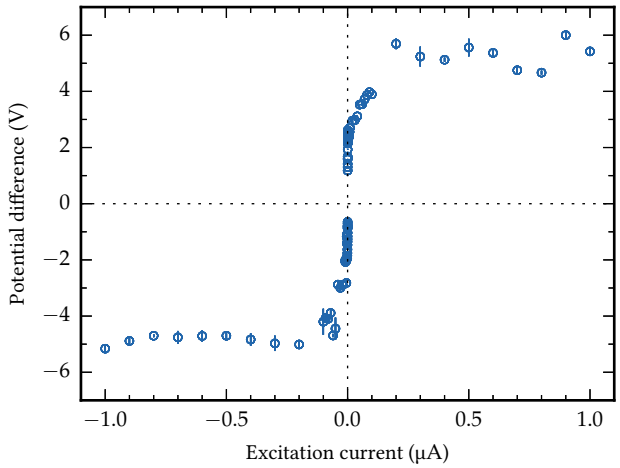

Figure 3.10: Two-contact current-voltage characteristics of typical fabricated contacts at room temperature. The sample in this case is $LaSr_{1.95}Sr_{0.05}CuO_2$. Note that there is a negative differential resistance for excitation magnitudes between 0.2 μA and 0.8 μA. The behaviour is suggestive of a tunnel junction between the sample surface and the metal contacts, consisting of an insulator layer with a bandgap of ∼4 eV.

atures, as demonstrated in figure 3.9. Measurement of deliberately short-circuited gold tracks show them to retain Ohmic behaviour when carrying currents in excess of 1 μA.

3.8 CHALLENGES ENCOUNTERED IN DEVELOPING THE TECHNIQUE

A number of samples were prepared for measurement in this way. At first, attempts to make DC transport measurements were consistently hampered by large contact resistances, of order 1 MΩ. By varying the excitation current, the impedance of the fabricated assembly was found to have some characteristics of a tunnel junction, as shown in figure 3.10. The junction appears to be caused by a layer of an insulating material with a bandgap of ∼4 eV between the contacts and the

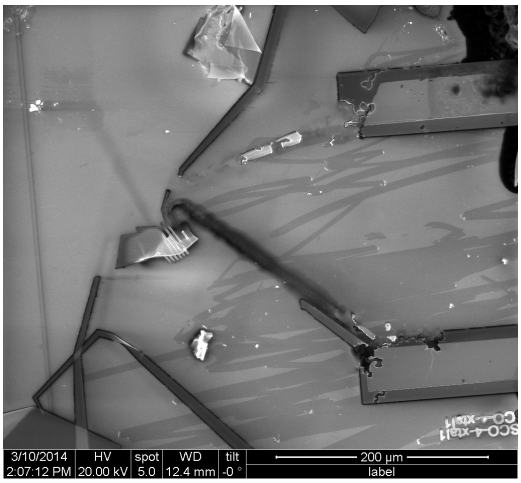

(a) Pitted and broken gold leads

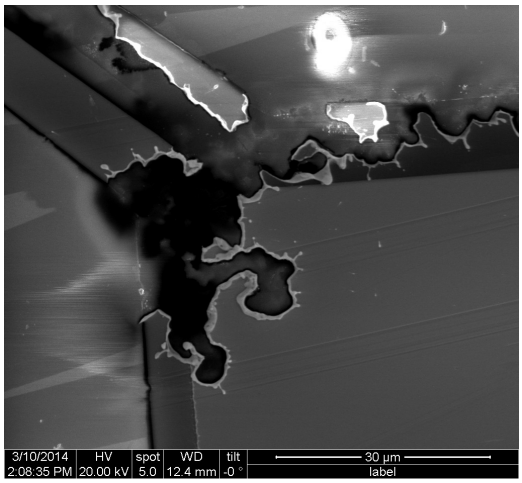

(b) Pitted gold leads (detail)

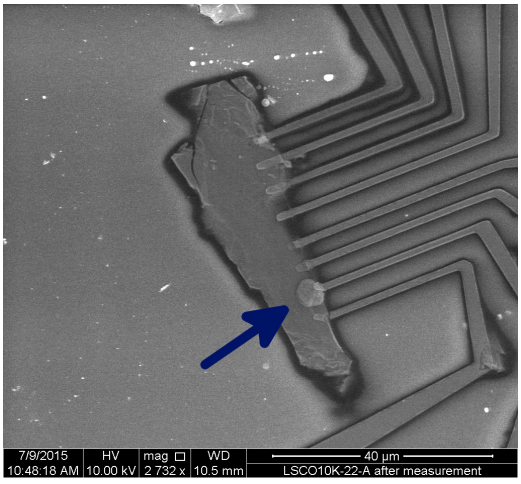

(c) Oyster shell deposit under contact

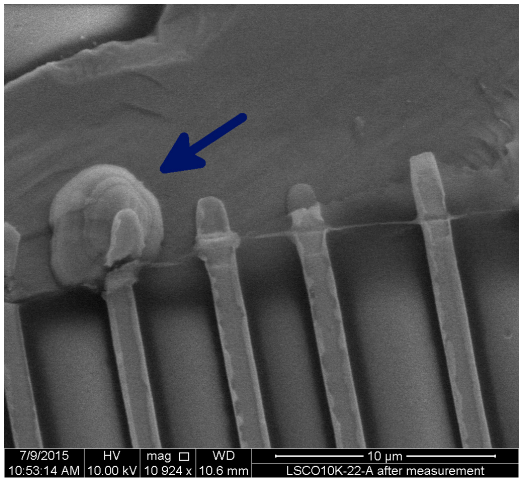

(d) Oyster shell deposit (detail)

Figure 3.11: Damage to patterned gold leads and contacts due to high current densities.
a–b: Damage to patterned metal features, showing a characteristic pitting, suggestive of catastrophic Joule heating.
c–d: The devil's toenail. A deposit of material, probably gold, resembling an oyster shell, has accumulated under one of the patterned contacts on the sample surface (indicated with arrows).

sample surface. This is consistent with the 3.4 eV optical bandgap of SU-8 [34]. Hence it seems some residual SU-8, not removed in development, remained on the sample surface before patterning with metal contacts. This is plausible, despite the O_2 plasma etch procedure which was intended to remove residual resist, because SU-8 is relatively slow to etch in pure O_2 plasma [35]. It was not possible to push the excitation current much beyond the negative differential resistance regime of the tunnel junction due to destructive Ohmic heating of the contact leads (see figure 3.11a–b). Nevertheless, there is some hint, for excitation currents in excess of 0.8 μA, of a contact resistance of ∼2–4 MΩ.

The strongest evidence that the current path through the fabricated assembly is exactly as designed, despite the high contact resistance and probable tunnel junction, is the appearance on some samples of unusual deposits, apparently metallic, between the patterned contacts and the sample surface following the application of a DC current through the sample. These deposits were absent after lift-off and appeared during measurement. One such deposit is illustrated in figure 3.11c–d, for which the contact in question was the current sink. The excitation currents used were very high, in an effort to overcome an apparent tunnel junction. The deposit appears to have accumulated in layers, corresponding to successive pulses of current, growing until the contact broke away from the rest of the patterned track. It seems likely that the deposit may have been caused by electro-migration of gold from the patterned contact lead [36]. This reassures us that, despite the high contact resistance, the applied exitation current is indeed travelling through the sample.

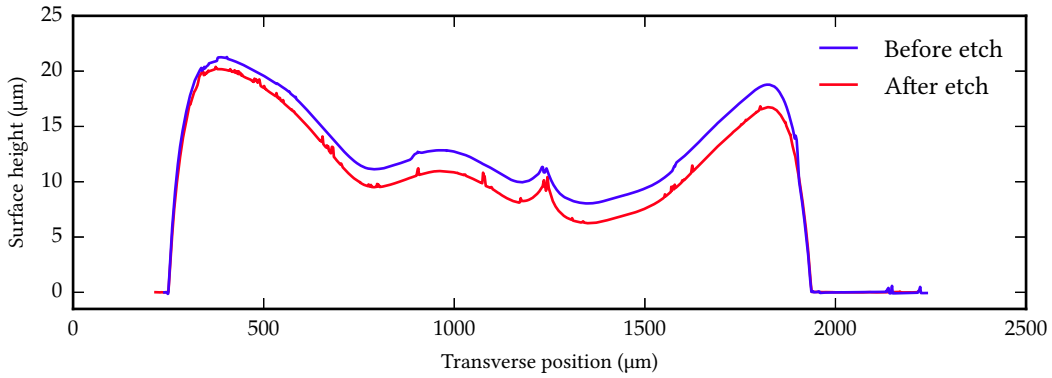

(a) Surface profile of composite substrate cross-section

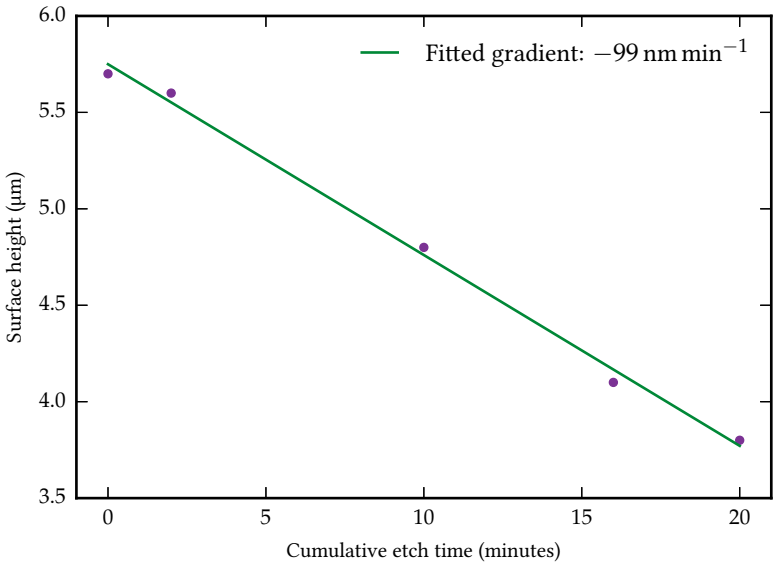

(b) Evolution of resist thickness with etch time

Figure 3.12: Susceptibility of SU-8 to SF_6/O_2 plasma etch. a: Height profile of SU-8 resist above quartz substrate before and after a cumulative 20 min etch, as described in the text. The irregular surface with pronounced edge-bead is clearly visible. b: Rate of removal of SU-8 on a different substrate during the same etch.

3.8.1 *Eliminating residual SU-8*

Although SU-8 is very slow to etch in a pure O_2 plasma, the introduction of a small volume fraction of fluorine plasma, by means of a mixed atmosphere of O_2 and SF_6, can result in relatively rapid etch rates [35]. We explored the efficacy of such an etch in cleaning the surface of the embedded sample before EBL patterning and reducing the contact resistance. In order to characterise the etch rate, we used a Tencor P-17 surface profilometer to gauge the thickness of the SU-8 layer on the quartz substrate. We then explored various etching routines using a reactive ion etch (RIE) system (a custom-built Benchtop System 90). Use of both instruments, which reside at the Science and Technology Facilities Council's Innovations Technology Access Centre for Micro- and Nano-Technology (STFC I-TAC MNT), was made possible by research visits to their cleanroom facilities at the Rutherford Appleton Laboratory.

By varying various parameters of the RIE, we were able to achieve extremely reliable and reasonably rapid etch-rates. Figure 3.12 shows the characterisation of an etch with the following parameters—SF_6 flow rate: 10 SCCM; O_2 flow rate: 50 SCCM; pressure: 100 mTorr; radio-frequency oscillator power: 120 W. This results in a repeatable SU-8 etch-rate of $(99 \pm 6)\,\mathrm{nm\,min^{-1}}$.

3.9 PROMISING TRANSPORT MEASUREMENTS

The SF_6/O_2 etch made quite a pronounced difference to transport measurements. Typical two-wire resistances through the entire sample assembly dropped from

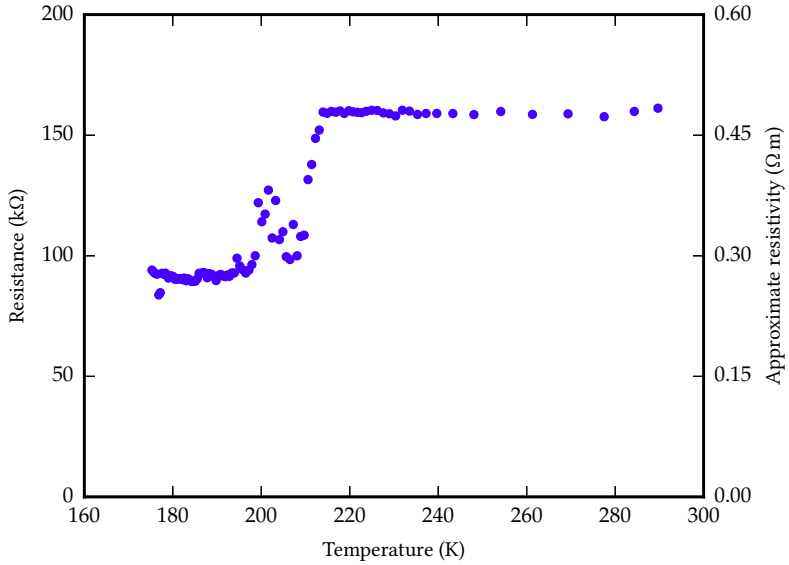

Figure 3.13: Four-contact DC resistance measurement of a sample of $Sr_2MnO_2Cu_{1.5}Se_2$, cooling from room temperature. There is an apparent phase transition at 213 K. Resistivity has been calculated by estimating the sample dimensions from electron micrographs.

$\sim$2 MΩ, consistently for all sample materials, to between 10 kΩ and 200 kΩ, depending on the sample material.

To date, we have only been able to measure a small number of samples following this improvement to the technique. In order to test the methodology of measurement of complex materials in small crystal form, the compound $Sr_2MnO_2Cu_{1.5}Se_2$ was selected as a subject of study because it has a complex, non-trivial formula comprised of a variety of cations and anions in a layered planar structure. It is thus highly representative of typical correlated fermion systems under current investigation. Related semiconducting oxychalcogenides and fluoride chalcogenides have been identified as having potential for exploitation as transparent conducting materials [37]. The structure of $Sr_2MnO_2Cu_{1.5}Se_2$ consists of alternating planes of $Cu_{1.5}Se_2$ and MnO_2 separated by layers of Sr. There have been several previous

studies of the structure and magnetisation in this and related compounds [38–41]. The sulphide analogue $Sr_2MnO_2Cu_{1.5}S_2$ shows long-range ordering of Cu^+ and tetrahedral vacancies, whereas such ordering in $Sr_2MnO_2Cu_{1.5}Se_2$ is only short-range [38]. This is thought to be associated with a greater mobility of Cu^+ ions in the sulphide than in the selenide. There is also a significant difference between the two structures in their magnetic ordering. In the selenide, the Mn ions are ferromagnetically ordered within MnO_2 planes, while each plane is antiferromagnetically coupled to the adjacent planes, with a Néel temperature of 53 K. There is similar behaviour when Ag is substituted for Cu. Meanwhile the sulphide has a much more complicated structure of zigzag antiferromangetism within the planes, with a Néel temperature of 28 K. It is also possible that these compounds display charge ordering of the mixed-valent Mn ions [38, 40, 41].

It has been suggested that the MnO_2 layer may behave as a Mott insulator and that $Sr_2MnO_2Cu_{1.5}Se_2$ and related compounds may display interesting electronic and magnetic behaviour analogous to the layered oxides [38]. A powder transport study of a related compound with full occupancy of the coinage metal site, $Sr_2MnO_2Cu_2Se_2$, has revealed semiconducting behaviour with a resistivity of 0.418 mΩ m at room temperature [39]. Transport in such compounds is expected to be highly anisotropic and to be dominated by in-plane transport in the coinage metal chalcogenide planes. As such, the details of structural ordering in these planes is likely to strongly influence the transport properties. Little is yet known about the low-temperature transport properties of $Sr_2MnO_2Cu_{1.5}Se_2$. Measurements are particularly hindered by the absence, to date, of available single-crystal samples of a size suitable for conventional transport measurements. Hence this material is well suited to measurements using the technique developed here. Some

representative data from a sample of $Sr_2MnO_2Cu_{1.5}Se_2$ are shown in figure 3.13.

The sample measured here is shown in figure 3.14a, embedded in SU-8. It was then patterned with contacts for simple four-wire resistance measurements (with a comb of eight contacts for redundancy) and measured using a 10 nA, 0.5 Hz (effectively DC) excitation from a Keithley 6221 current source and a Keithley 2182A nanovoltmeter. This permitted subtraction of alternate forward and backward currents to eliminate voltage bias due to thermoelectric effects. The sample was allowed to cool slowly in an evacuated cryostat insert immersed in liquid nitrogen.

The data show what appears to be a clear phase transition in the resistivity at 213 K. Below 175 K, the resistance became unphysically large. Inspection of the sample after warming again to room temperature (figure 3.14c–d) shows that it appears to have disintegrated into a finer powder of sub-micron crystallites, partly destroying the patterned contacts, possibly due to excessive Joule heating (though this seems unlikely, since the measured resistivity corresponds to a Joule heating power density of approximately 300 kW m^{-3} at 175 K, equivalent to a total heating power of order 100 pW in the sample). The observed resistivity transition at 213 K corresponds closely to a suggested structural transition that has been observed in electron diffraction of similar-sized crystallites [38], wherein copper vacancies in the $Cu_{1.5}Se_2$ layer adopt short-range order at low temperatures, which disappears above 220 K. It is possible that strain caused by this structural transition contributed to the destructive stresses in our sample.

The initial resistivity data from $Sr_2MnO_2Cu_{1.5}Se_2$ shows some promise in exploring the electronic properties of this material and related oxide chalcogenides, many of which are currently inaccessible to measurements of electronic transport.

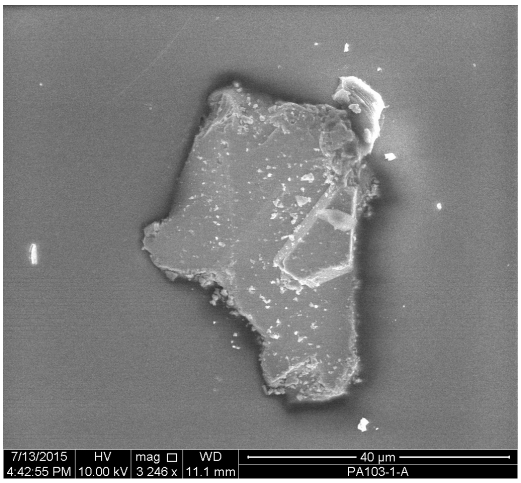

(a) Sample embedded in SU-8

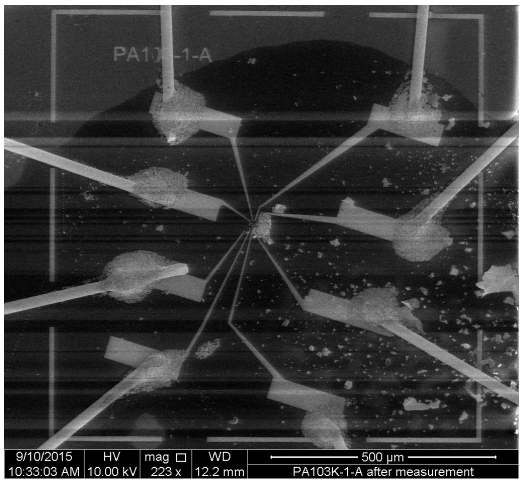

(b) Sample patterned for measurement

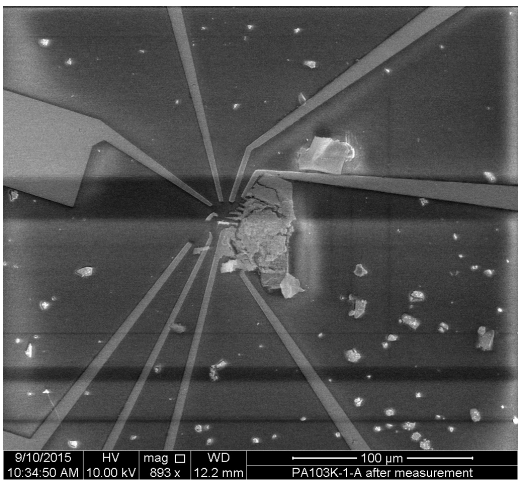

(c) Sample after measurement

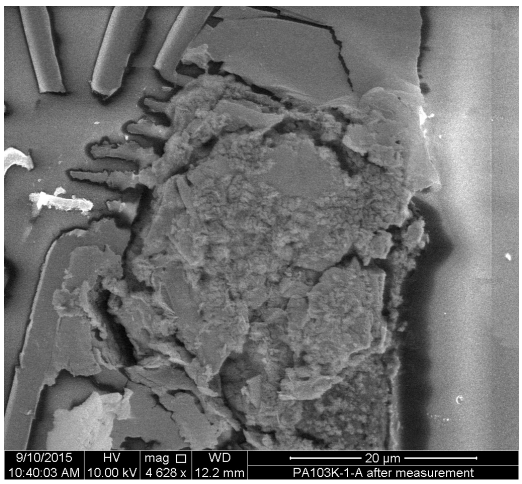

(d) After measurement (detail)

Figure 3.14: A sample of $Sr_2MnO_2Cu_{1.5}Se_2$, before and after measurement.
a: The sample, embedded in SU-8 and subjected to a 6 min (approximately 600 nm) SF_6/O_2 etch.
b: The sample patterned with contacts for measurement.
c–d: The sample after measurement, showing curious disintegration, possibly due to an instability of the sample to the effect of the excitation current.

3.10 CLOSING COMMENTS

There are many ways in which this method could yet be improved and enhanced. It would be relatively straightforward, with an appropriate electron microscope, to perform EDX measurements of embedded samples in situ before and/or after transport measurements are made. This would also help to determine whether reactive species from the etching processes contaminate the sample surface significantly or interfere with the chemistry of the sample, providing a better understanding of whether the high resistances sometimes observed are a result of high contact resistance or simply the result of the sample dimensions and resistivity. More complicated contact geometries, including Hall and van der Pauw measurement geometries, for which such planar samples are well suited, are eminently feasible. With a thicker photoresist layer, it may even be possible to embed platelet-like crystallites on end, in such a way as to permit *c*-axis transport measurements as opposed to *a*-*b* plane measurements.

The work described in this chapter represents substantial progress in the development of a new technique for transport measurements on as-synthesised single-crystal inorganic samples, with dimensions of order 10 μm, derived from sintered powders. Most of the fabrication processes involved have been refined to the extent that relatively little further characterisation remains to be done. It is our hope that this technique may soon be made sufficiently straightforward as to be routinely useful as a short-cut to obtaining single-crystal transport data from materials in which crystal growth has not yet yielded large enough samples for measurement by conventional methods.

Part II

MOLECULAR NANO-MAGNETS AS A PROBE OF SPIN-CURRENT RELAXATION IN A TOPOLOGICAL INSULATOR

> Above everything else, the apprentice can be assured that he is entering into a great and noble art, the possibilities of which are far from being exhausted.
>
> D Cumming on the *Training of Apprentices* [1]

4

TRANSPORT MEASUREMENT TECHNIQUES

This chapter describes some of the well established low-temperature and high-magnetic-field electrical transport techniques that were used in the work recounted in subsequent chapters. It describes the classical Hall effect for systems of multiple conducting quasiparticle species, and various features of the anisotropic magnetoresistance of 2-D and 3-D metals, all of which will be of use in chapter 6.

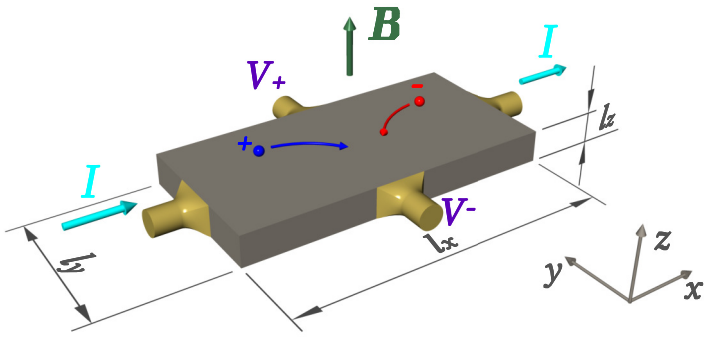

Figure 4.1: Schematic of a Hall effect experiment. Current, I, flows through the sample along the x-axis and the applied magnetic field, $\mathbf{B}$, has a positive z-component. Hall voltage, $V_{\mathrm{H}} = V_+ - V_-$, is measured along the y-axis. Deflected trajectories of electron-like (labelled '$-$') and hole-like (labelled '$+$') quasiparticles is illustrated.

4.1 CLASSICAL HALL EFFECT

In chapter 6, we present results of some Hall effect measurements on SmB_6. It will be particularly useful to recall some features of the semi-classical Hall effect for a material with more than one quasiparticle species [42–45]. In the semi-classical description of the Hall effect, illustrated in figure 4.1, quasi-particles with group velocity $\mathbf{v}$ and charge q, forming an electric current through a material in a magnetic field $\mathbf{B}$ experience a force transverse to their velocity by virtue of the $\mathbf{B}$-dependent component of the Lorentz force, $\mathbf{F}$:

$$\mathbf{F} = q\left(\mathbf{E} + \mathbf{v} \times \mathbf{B}\right) , \tag{4.1}$$

where $\mathbf{E}$ is the electric field on the quasi-particles. Under the Drude-Sommerfeld model, in the steady state, the time-averaged drift velocity of quasiparticles, $\mathbf{v}_\mathrm{d}$, is related to the Lorentz force and the quasiparticle effective mass, m^* and scattering time, τ, simply as

$$\begin{aligned}\mathbf{F} &= \frac{m^*\mathbf{v}_\mathrm{d}}{\tau} \\ &= q\left(\mathbf{E} + \mathbf{v}_\mathrm{d} \times \mathbf{B}\right) \ . \end{aligned} \tag{4.2}$$

This can be re-phrased in terms of current density, $\mathbf{j}$,

$$\begin{aligned}\mathbf{j} &= nq\mathbf{v}_\mathrm{d} \\ &= \sigma_0\mathbf{E} + q\frac{\tau}{m^*}\mathbf{j} \times \mathbf{B} \ , \end{aligned} \tag{4.3}$$

where $\sigma_0 = \frac{nq^2\tau}{m^*}$ is the conductivity in the absence of a magnetic field. Equation 4.3 can be further rearranged to obtain the resistivity, ρ:

$$\mathbf{E} = \rho\mathbf{j} = \frac{1}{\sigma_0}\left(\mathbf{j} - q\frac{\tau}{m^*}\mathbf{j} \times \mathbf{B}\right) \ . \tag{4.4}$$

Now, if we align the magnetic field with the z-axis and consider only the quasi-particle currents in the x-y plane, we can state the resistivity as a tensor, relating the x- and y-components of $\mathbf{j}$ and $\mathbf{E}$. If the material is isotropic in the x-y plane,

$$\begin{aligned}\mathbf{E} &= \frac{1}{\sigma_0}\begin{pmatrix} 1 & -\frac{q}{e}\omega_\mathrm{c}\tau \\ \frac{q}{e}\omega_\mathrm{c}\tau & 1 \end{pmatrix}\mathbf{j} \ , \\ \rho &= \frac{1}{\sigma_0}\begin{pmatrix} 1 & -\frac{q}{e}\omega_\mathrm{c}\tau \\ \frac{q}{e}\omega_\mathrm{c}\tau & 1 \end{pmatrix} \ , \end{aligned} \tag{4.5}$$

where e is the elementary charge constant and $\omega_c = \frac{eB}{m^*}$ is the quasiparticle cyclotron frequency and $B = |\mathbf{B}|$. The off-axis component ρ_{yx} of the resistivity tensor provides the Hall coefficient,

$$R_H = \frac{\rho_{yx}}{B} \,. \tag{4.6}$$

For a single quasiparticle species, this gives

$$R_H = \frac{1}{nq} \,. \tag{4.7}$$

By inverting the resistivity tensor, one obtains the corresponding conductivity tensor, σ:

$$\begin{aligned} \mathbf{j} &= \sigma \mathbf{E} \,, \\ \sigma &= \frac{\sigma_0}{1 + {\omega_c}^2 \tau^2} \begin{pmatrix} 1 & \frac{q}{e}\omega_c \tau \\ -\frac{q}{e}\omega_c \tau & 1 \end{pmatrix} \,, \end{aligned} \tag{4.8}$$

where we have exploited the fact that $q = \pm e$, so $\frac{q^2}{e^2} = 1$. In the absence of a magnetic field, we can easily see that we regain the expected scalar conductivity.

When the material has more than one quasiparticle type, one electron-like and one hole-like for example, the current densities of each of the quasiparticle types are simply summed to obtain the total current density. Hence the individual quasiparticle conductivities are also additive. Where the index i denotes the quasiparticle species,

$$\mathbf{j} = \sum_i \mathbf{j}_i = \left(\sum_i \sigma_i \right) \mathbf{E} = \sigma \mathbf{E} \,. \tag{4.9}$$

Hence the resistivity in the case of multiple quasiparticle species is

$$\rho = \frac{1}{{\sigma_{xx}}^2 + {\sigma_{xy}}^2} \begin{pmatrix} \sigma_{xx} & -\sigma_{xy} \\ \sigma_{xy} & \sigma_{xx} \end{pmatrix} , \tag{4.10}$$

where $\sigma_{xx} = \sum_i \frac{\sigma_{0i}}{1 + {\omega_{ci}}^2 {\tau_i}^2}$ and $\sigma_{xy} = \sum_i \frac{\sigma_{0i} \frac{q_i}{e} \omega_{ci} \tau_i}{1 + {\omega_{ci}}^2 {\tau_i}^2}$. Remembering equation 4.6, it follows that the Hall coefficient is

$$R_{\mathrm{H}} = \frac{1}{B} \cdot \frac{\sigma_{xy}}{{\sigma_{xx}}^2 + {\sigma_{xy}}^2} . \tag{4.11}$$

The Hall coefficient can be measured by applying a longitudinal current and measuring the transverse voltage or Hall voltage, V_{H}, as portrayed in figure 4.1. Bearing in mind that the x-component of the current density is related to the total current by $j_x = \frac{I}{l_y l_z}$, with the dimensions l_y & l_z defined in the figure, the Hall voltage is related to the y-component of the electric field and to the Hall coefficient by

$$\begin{aligned} V_{\mathrm{H}} &= E_y \cdot l_y \\ &= \rho_{yx} j_x \cdot l_y \\ &= \frac{R_{\mathrm{H}} B I}{l_z} . \end{aligned} \tag{4.12}$$

4.2 MAGNETORESISTANCE AS A PROBE OF THE FERMI SURFACE

Key to understanding the physical properties of any metallic correlated electron system is a determination of the size and shape of its Fermi surface. Measurements of electrical transport in a uniform magnetic field can reveal a great deal

about the fermiology. When a charged quasiparticle undergoes orbits in the real-space plane to which the field is normal, its momentum likewise performs orbits in the corresponding reciprocal-space plane. Because the quasiparticle's acceleration by the field is always perpendicular to its momentum, its energy, ϵ, is unchanged. Hence the reciprocal-space orbit must traverse a surface of constant energy. Since the only such surfaces with populated and available states in proximity are in the immediate neighbourhood of the chemical potential, these orbits follow the **B**-normal cross-section of the Fermi surface. The specific nature of these trajectories strongly influences the character of the magnetoresistance, measurements of which are therefore a rich source of information about Fermi surface morphology. Presented here is a short description of some features of magnetoresistance in two- and three-dimensional systems, which will inform the discussion of experiments on SmB_6 in chapter 6. A more complete introduction can be found in several sources [46–48].

4.2.1 *Magnetoresistance in simple metals*

Let us first consider the simple case of a 3-D metal with a Fermi surface that does not protrude beyond the first Brillouin zone, and which therefore has the topology of a sphere. Under the Lorentz force of equation 4.2, the real-space trajectories of quasiparticles follow roughly helical closed orbits with a radius $r_{\mathbf{B}} = v_d/\omega_c$. In the relaxation time (τ) approximation, a quasiparticle will travel along an arc of length equal to the mean free path, $\lambda = v_d\tau$, before having its momentum randomised by a scattering event. When the magnetic field is small, such that

$\lambda \ll r_{\mathbf{B}}$, it is straightforward to show that the fractional change in resistance due to the applied field is

$$\frac{\Delta\rho(\mathbf{B})}{\rho(0)} \propto \left(\frac{\lambda}{r_{\mathbf{B}}}\right)^2 \propto B^2 \,. \tag{4.13}$$

In higher fields, the average quasiparticle trajectory before scattering will be a more complete arc, or even multiple full orbits. The real-space trajectory is determined by the velocity, $\mathbf{v}(\mathbf{k}) = \frac{1}{\hbar}\frac{\partial\epsilon}{\partial\mathbf{k}}$, which is naturally always normal to the Fermi surface and which changes as the wavevector, $\mathbf{k}$, describes the reciprocal-space orbit. The conductivity will then depend on exactly how the quasiparticle velocities are averaged over the relaxation time. This is expressed in the Chambers formula [47, 49], which is, more formally, the solution to the Boltzmann transport equation in the presence of electric and magnetic fields and under the relaxation time approximation [50]. This provides the conductivity tensor,

$$\sigma_{ij} = \frac{e^2\tau}{4\pi^3}\int\left(-\frac{\mathrm{d}f_0}{\mathrm{d}\epsilon}\right) v_i(\mathbf{k})\,\overline{v}_j(\mathbf{k})\,\mathrm{d}^3\mathbf{k}\,, \tag{4.14}$$

where the indices i and j can each be any of the Cartesian coordinates, f_0 is the equilibrium Fermi-Dirac occupation function and

$$\overline{v}_j(\mathbf{k}) = \frac{1}{\tau}\int_{-\infty}^{0} v_j(\mathbf{k}, t)\,\mathrm{e}^{t/\tau}\,\mathrm{d}t \tag{4.15}$$

is the time-averaged j-component of the velocity, weighted by the $\mathbf{k}$-independent relaxation time, τ.

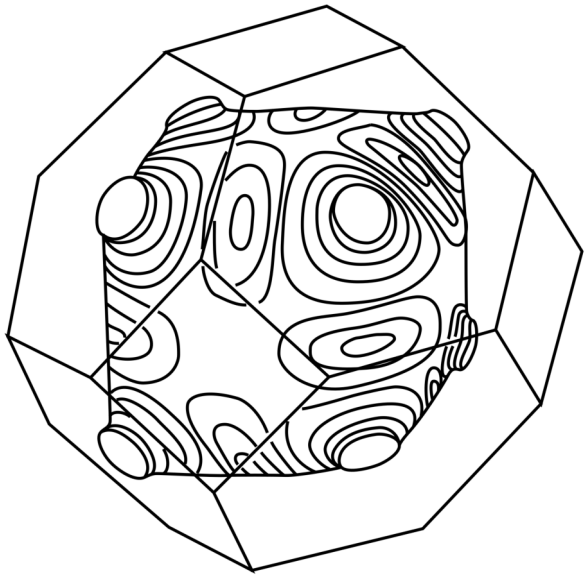

Figure 4.2: The Fermi surface of copper, contained within the first Brillouin zone (wire polygon). Contours of constant wavenumber give an impression of the curvature of the surface. Note the necks at the $(1\,1\,1)$ and equivalent directions. *Reproduced from [44].*

4.2.2 *Anisotropic magnetoresistance*

The Chambers formula can be applied to arbitrary Fermi surface morphology, not just the restrictive case described above. It provides the means to a numerical determination of magnetotransport for any metal, provided one has sufficient information about the fermiology. However, because σ_{ij} only depends on a path-average of the $\mathbf{k}$-space orbit, it is not so straightforward to do the reverse and deduce the exact form of the Fermi surface from magnetoresistance measurements. Instead, one can deduce certain key features, particularly by varying the angle of the applied field to probe the anisotropic magnetoresistance (AMR).

One feature that can often be determined quite easily is the presence of so-called *open orbits*. These are $\mathbf{k}$-space trajectories that follow extended parts of the Fermi

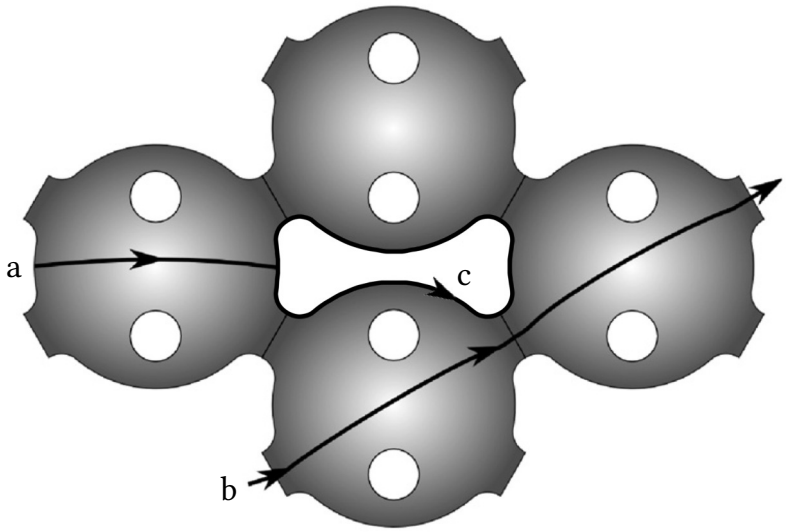

Figure 4.3: Fermi surface orbits in copper; a: closed; b: open; c: 'dog-bone'. Four reciprocal space unit cells are shown.
Reproduced from [51].

surface, when it extends beyond the first Brillouin zone, that connect it to neighbouring copies of itself, each translated by a reciprocal lattice vector. Open orbits therefore do not form loops like the *closed orbits* alluded to in section 4.2.1 above. Many materials contain both types, a notable example being the well-known Fermi surface of copper, shown in figure 4.2, which consists of a body-centred cubic array of rounded near-cubes, connected by narrow necks in the $(1\,1\,1)$ and equivalent directions [48, 52]. There exist closed orbits around the necks and the body of the Fermi surface, as well as the famous 'dog-bone' orbit. With the correct magnetic field orientation, open orbits traverse the necks and connect an infinite number of reciprocal lattice unit cells in each direction. Examples are shown in figure 4.3.

The character of the magnetoresistance contributions from open and closed orbits is particularly easy to distinguish at high fields. At high enough fields, closed

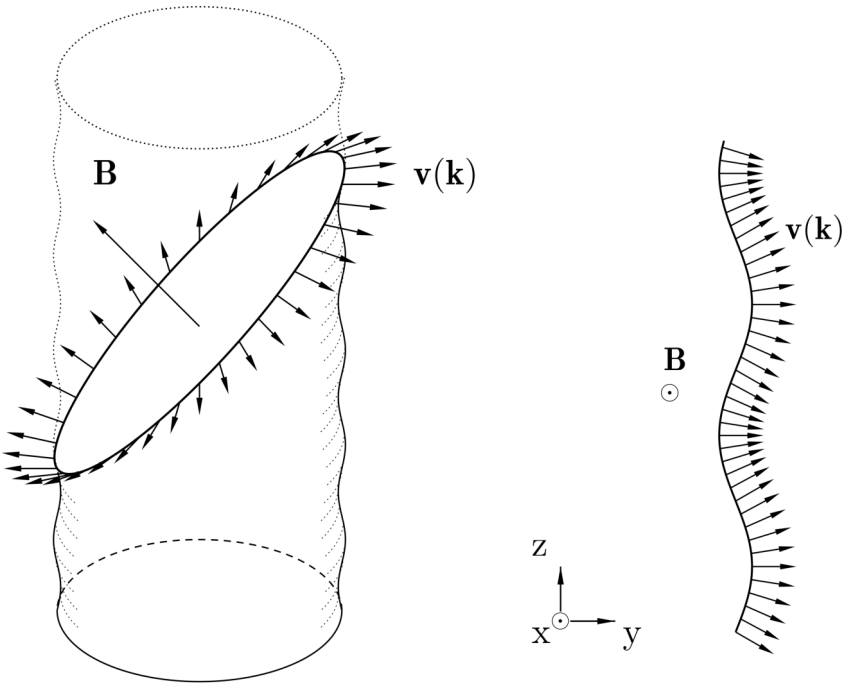

(a) Closed orbit (b) Open orbit

Figure 4.4: Fermi surface of a typical quasi-2-D metal, with the inter-plane axis (the cylinder axis) aligned with $\hat{\mathbf{z}}$. The velocity $\mathbf{v}(\mathbf{k})$ is shown (arrows normal to the Fermi surface) for a closed orbit (a: with $\mathbf{B}$ at an angle to $\hat{\mathbf{z}}$) and an open orbit (b: with $\mathbf{B} \parallel \hat{\mathbf{x}}$). The closed orbit will clearly average $\mathbf{v}$ to zero if $\omega_c \tau \gg 1$, whereas the open orbit will retain a non-zero $\overline{v}_y$.
Reproduced from [53].

orbits cause those components of the velocity perpendicular to **B** to be averaged to zero, because **k** dwells as long in each region of the Fermi surface as in the diametrically opposite region, the two contributing opposing velocity contributions. This is illustrated in figure 4.4a. In the case where a material yields only closed orbits when a strong magnetic field is aligned with $\hat{\mathbf{z}}$, the conductivity is a simple extension of the form in equation 4.8,

$$\sigma_{ij} = \sigma_0 \begin{pmatrix} \gamma^2 a_{xx} & \gamma a_{xy} & \gamma a_{xz} \\ -\gamma a_{xy} & \gamma^2 a_{yy} & \gamma a_{yz} \\ -\gamma a_{xz} & -\gamma a_{yz} & a_{zz} \end{pmatrix} , \tag{4.16}$$

where $\gamma = (\omega_c \tau)^{-1} \ll 1$ and the a_{ij} factors are material-dependent [54]. Taking the inverse of the conductivity yields a resistivity tensor with diagonal components ρ_{ii} that have no field dependence in the high-field limit. The magnetoresistance contribution from closed orbits therefore saturates. Intuitively, above a certain magnetic field strength, the quasiparticles are making several complete orbits within the relaxation time and a further increase in magnetic field makes no material difference to their overall trajectory.

By contrast, open orbits do not average to zero the component of the velocity that is perpendicular to the Fermi surface, as can be seen from figure 4.4b. Adopting the geometry defined in the figure, with an open orbit along $\hat{\mathbf{z}}$ due to a uniform magnetic field parallel to $\hat{\mathbf{x}}$, the conductivity in the high-field limit becomes

$$\sigma_{ij} = \sigma_0 \begin{pmatrix} a_{xx} & a_{xy} & \gamma a_{xz} \\ -a_{xy} & a_{yy} & \gamma a_{yz} \\ -\gamma a_{xz} & -\gamma a_{yz} & \gamma^2 a_{zz} \end{pmatrix} . \tag{4.17}$$

Once more, this yields diagonal elements of the resistivity tensor ρ_{xx} and ρ_{yy} that have no field dependence in the high-field limit, that is to say they still saturate. Contrastingly,

$$\rho_{zz} \propto (\omega_c \tau)^2 \propto B^2 \,, \tag{4.18}$$

so the resistivity component parallel to the open orbit does not saturate and continues to increase with B. Again, one can understand this situation intuitively by considering semi-classical real-space trajectories. Quasiparticles with a non-zero z-component of $\mathbf{v}$ are deflected by the $\mathbf{k}$-space orbit onto a meandering trajectory in the y-direction. ρ_{zz} is subject to two competing tendencies. It increases with increasing ω_c, which encourages a quicker adoption of the y-ward wandering path. Meanwhile, it decreases with increasing scattering rate, $1/\tau$, which resets the particle trajectories so that they may resume movement in the z-direction under the influence of the z-component of the electric field. Because the y-component of the velocity never averages to zero, the competing pull of the magnetic field and the scattering rate on ρ_{zz} never saturates and, for a fixed relaxation time, the resistivity component in the direction corresponding to to the reciprocal space open orbit retains a field dependence, even in high fields.

Where a pocket of the Fermi surface encloses unoccupied states, rather than filled states, such that the velocity vector points inwards rather than outwards, it has characteristics of hole-like quasiparticle dynamics, rather than electron-like quasiparticle dynamics, and is described as a hole pocket. In real systems, it is not uncommon to find electron and hole pockets nested inside one another. This can lead to a superposition of magnetoresistance effects. Smaller pockets, with higher

Fermi surface curvature, will necessarily have smaller effective masses and so the different contributing magnetoresistance effects will have different cyclotron frequencies for a given field strength, lending further complexity to the shape of the AMR.

4.2.3 *Dimensionality of the Fermi surface*

Chapter 6 is concerned with SmB_6, a proposed 3-D topological insulator material with, it is suggested, 2-D metallic surface states coexisting with a simple-cubic Kondo-insulating 3-D bulk. Some studies, however, have suggested instead that the measured properties of this material are consistent with a non-topological Kondo insulator. Measurements of the AMR will be important in determining which of these two hypotheses is more likely and so it will be useful to have some prior understanding of the general properties of AMR for Fermi surfaces of different dimensionalities.

As mentioned above with regard to copper, materials with 3-D Fermi surfaces may display a complex AMR, according to the shape of the Fermi surface and whether it is closed or extended. The AMR of a 3-D material will contain features that saturate in high fields, due to closed orbits, and may include non-saturating features due to open orbits. Where open orbits occur at a wide range of field orientations, they will dominate the high-field AMR. Field orientations that do not correspond to an open orbit will appear as dips in the magnetoresistance, as it falls to a saturated value. In materials where open orbits are fewer and further between, they will appear instead as spikes in an otherwise largely saturated high-

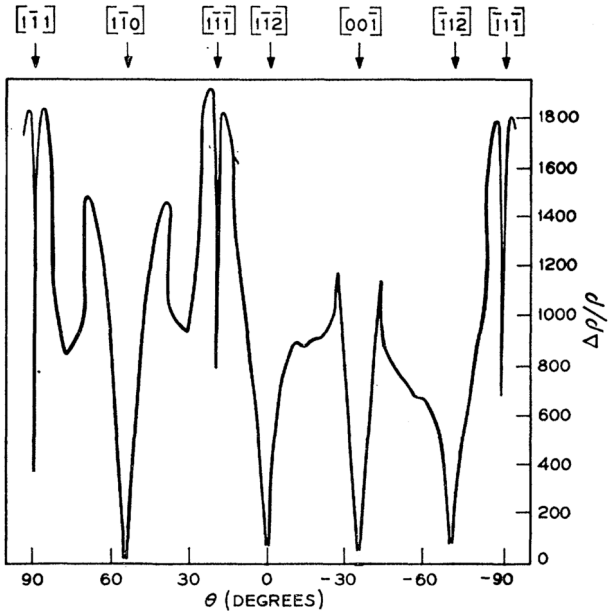

Figure 4.5: AMR of copper showing sharp dips at significant symmetry directions, corresponding to closed orbits of the Fermi surface and consequently saturated magnetoresistance. In the notation of figure 4.1, magnetic field is rotated from $\mathbf{B} \parallel \hat{\mathbf{z}}$ ($\theta = 0°$) to $\mathbf{B} \parallel \hat{\mathbf{y}}$ ($\theta = 90°$), while the current is applied along $\hat{\mathbf{x}}$ and the measured resistivity component is ρ_{xx}.
Reproduced from [55].

field AMR. These spikes and dips at special orientations contain a lot of information about the precise shape of the Fermi surface. As an example, the AMR of copper is shown in figure 4.5. Regardless of the presence or absence of these sharp features, the AMR must have the same rotational symmetry as the Fermi surface, which follows the point group of the reciprocal lattice, which in turn is determined by the space group of the crystal lattice. As such, in an experiment geometry like that shown in figure 4.1, with current applied along the $(1\,0\,0)$ direction, one would expect bulk-origin AMR in SmB_6 to display four-fold rotational symmetry as the field is rotated around the current axis.

Quasi-2-D and quasi-1-D layered metallic materials typically show a rich variety of correlated electron behaviour. Intense interest in layered organic metals and unconventional superconductors has lent great importance to the study of the Fermi surfaces of such quasi-reduced-dimensionality systems [46, 56, 57]. The Fermi surface of a quasi-2-D metal takes the form of a warped cylinder, such as that shown in figure 4.4. The shape of the $\hat{\mathbf{z}}$-normal cross-section is determined by the in-plane transfer integrals. The warping is determined by the weaker inter-plane transfer integral. Similarly, the Fermi surfaces of quasi-1-D metals take the form of warped sheets. The slight warping of the Fermi surfaces of quasi-reduced-dimensionality systems often supports rich and complex so-called angle-dependent magnetoresistance oscillations (AMRO), as there are a multitude of intricate Fermi surface orbits traversing them. Quasi-2-D and -1-D AMR will not be of particular relevance to our investigation of SmB_6 but they are worth mentioning for the fact that the specific details of Fermi surface shape can lead to field-dependence of the magnetoresistance that differs markedly from the rather simplistic B^2 relationship presented above. Various functional forms are possible in addition to B^2, including B and $B^{3/2}$ [47].

A true 2-D material has no out-of-plane conductivity, momentum or velocity components. In many respects its Fermi surface resembles a simpler version of the quasi-2-D Fermi surfaces described above, in the limit of zero inter-plane transfer integral (and hence no Fermi surface warping). Because the only possible orbits are in the plane of the surface, only the component of $\mathbf{B}$ normal to the surface contributes to the magnetoresistance. Therefore, where θ is the angle between $\mathbf{B}$ and the surface normal, any B-dependence in the magnetoresistance is replaced by $B\cos\theta$. Ordinarily, a 2-D material will therefore not show any magnetoresis-

tance when the field is in the plane of the material. In chapter 6, we see that this is complicated in SmB_6 by the existence of multiple facets in different relative orientations, so that it is not possible to attribute the presence of magnetoresistance at all field orientations to an absence of 2-D behaviour.

4.3 QUANTUM OSCILLATIONS

One of the most useful tools for exploring the Fermi surface morphology of metals is the study of quantum oscillations. Oscillations in properties such as the magnetisation (the de Haas–van Alphen effect) and resistivity (the Shubnikov–de Haas effect), periodic in $1/B$, arise from the Landau quantisation of allowed states in reciprocal space. Quantum oscillations are observed when the applied magnetic field is swept, such that the Landau levels successively pass through extremal cross-sections of the Fermi surface [58]. They allow for a quantitative measure of the areas of extremal cross-sections of the Fermi surface. By altering the orientation of the applied field, one can therefore also obtain some information about the shape and dimensionality of the Fermi surface. No new quantum oscillations data are presented in this thesis, but the provenance of previously reported de Haas–van Alphen oscillations in SmB_6 has been the subject of some protracted debate.

5

TOPOLOGICAL INSULATORS

Until relatively recently, our knowledge of the mechanisms and behaviour of systems of condensed matter was built exclusively on models of spontaneously broken symmetry. While symmetry breaking remains essential to understanding most aspects of condensed matter physics, the last few decades have seen the realisation that some phases of matter can be fully explained only with additional theoretical tools. One such new tool is the application of topology to systems in the solid state. This has led to the discovery, in such systems, of novel phenomena, including properties with unusually robust quantisation, which are related to topological invariants.

Since its inception, the study of topological condensed matter has caused much excitement, not just for its theoretical interest but also for its suggested practical applications. The technological use of so-called topological insulators (TIs) will require a better understanding of their transport properties. This chapter begins by explaining the background to current TI research in the discovery of the quantum Hall effect and topologically protected edge and surface transport. It then introduces the quantum spin Hall effect and the concept of two-dimensional and three-dimensional TIs. A short review of experimental studies of 3-D TIs follows. Finally, the likely topological Kondo insulator SmB_6 is reviewed in more detail and identified as a suitable subject for the transport study in chapter 6.

5.1 TOPOLOGY IN CONDENSED MATTER PHYSICS

5.1.1 *The quantum Hall effect*

In 1980, the discovery of the integer quantum Hall effect in a two-dimensional quasiparticle gas, constrained at a semiconductor heterojunction and subject to a strong magnetic field [59], provided the first example of a phenomenon in condensed matter physics that could not adequately be described solely in the spontaneous symmetry breaking paradigm of Landau [60]. A full understanding of the quantisation of Hall conductance required the development of theoretical tools that were to form the basis of the current understanding of topological protection of surface states in so-called topological insulators (TIs), topological superconductors, etc.. Before describing such materials, a short review of the integer quantum Hall effect is included here by way of an introduction to topological concepts in condensed matter. A slightly more detailed introductory overview is provided by Avron *& al.* [61] and a more thorough review by Bellisard *& al.* [62].

Shortly after the first report of quantised Hall conductance by von Klitzing *& al.*, an argument to explain it was proposed by Thouless *& al.* (TKNdN) [63], building on a non-topological argument of Laughlin [64, 65]. The TKNdN argument was neatly generalised by Niu *& al.* [66], who recognised the very precise quantisation as a manifestation of topological order. It describes the two-dimensional quasiparticle gas using a simple model Hamiltonian,

$$\mathcal{H} = \sum_j \left(\frac{1}{2m^*} \left(-i\hbar \boldsymbol{\nabla}_j - q\mathbf{A}(\mathbf{r}_j) \right)^2 + qE_y y_j \right) , \tag{5.1}$$

where $\mathbf{E} = E_y\hat{\mathbf{y}}$ is the electric field, $\mathbf{r} = (x, y, 0)$ is quasiparticle position, the magnetic vector potential $\mathbf{A}(\mathbf{r}) = (-By + A_x)\hat{\mathbf{x}} + A_y\hat{\mathbf{y}}$, and the sum runs over all quasiparticles, enumerated by index j. Of course, the values of A_x and A_y simply reflect a choice of gauge. Naturally, at low temperature (to reduce thermal broadening of energy levels) and high magnetic field (to increase the spacing of the allowed energy levels) the energy spectrum resembles the familiar Landau levels, with each level centred on an energy U_n, where $n \in \mathbb{N}$ and

$$U_n = \hbar\omega_c \left(n + \tfrac{1}{2}\right) . \tag{5.2}$$

As quasiparticles move through the sample by a displacement $\mathbf{d}$, they acquire a phase difference, $\frac{q}{\hbar}\mathbf{d} \cdot \mathbf{A}$, by virtue of the magnetic vector potential. There are additive terms in this additional phase that are due to the choice of gauge: if a quasiparticle is transported from one end of the sample to the other, i.e. $\mathbf{d} = L_x\hat{\mathbf{x}}$, there is a phase contribution $\theta = \frac{q}{\hbar}L_xA_x$, and if a quasiparticle is transported from one side of the sample to the other, i.e. $\mathbf{d} = L_y\hat{\mathbf{y}}$, there is a phase contribution $\phi = \frac{q}{\hbar}L_yA_y$. Conveniently, the x- and y-components of the quasiparticle group-velocity operator, $\mathbf{v} = \frac{\mathbf{p}}{m^*}$, can therefore be expressed as $v_x = -\frac{L_x}{\hbar}\frac{\partial\mathcal{H}}{\partial\theta}$ and $v_y = -\frac{L_y}{\hbar}\frac{\partial\mathcal{H}}{\partial\phi}$. If the ground state is non-degenerate, the transverse conductance can be worked out from the Kubo formula [66, 67] as

$$\begin{aligned}\sigma_{xy} &= \frac{iq^2\hbar}{L_xL_y}\sum_{n>0}\frac{\langle\psi_0 \,|\, v_x \,|\, \psi_n\rangle\langle\psi_n \,|\, v_y \,|\, \psi_0\rangle - \langle\psi_0 \,|\, v_y \,|\, \psi_n\rangle\langle\psi_n \,|\, v_x \,|\, \psi_0\rangle}{(E_0 - E_n)^2} \\ &= -2\frac{q^2\hbar}{L_xL_y}\,\mathrm{Im}\sum_{n>0}\frac{\langle\psi_0 \,|\, v_x \,|\, \psi_n\rangle\langle\psi_n \,|\, v_y \,|\, \psi_0\rangle}{(E_0 - E_n)^2} ,\end{aligned} \tag{5.3}$$

where the subscripts 0 & n denote the ground and $n^{\underline{\text{th}}}$ excited states, respectively, and E_0 & E_n are their associated energy eigenvalues. With the aid of our new expressions for the components of $\mathbf{v}$, this can be expressed as

$$\sigma_{xy} = -2\frac{e^2}{\hbar}\,\mathrm{Im}\sum_{n>0}\frac{\left\langle\psi_0\left|\frac{\partial\mathcal{H}}{\partial\theta}\right|\psi_n\right\rangle\left\langle\psi_n\left|\frac{\partial\mathcal{H}}{\partial\phi}\right|\psi_0\right\rangle}{(E_0-E_n)^2} \tag{5.4}$$

$$= -2\frac{e^2}{\hbar}\,\mathrm{Im}\sum_{n>0}\left\langle\frac{\partial\psi_0}{\partial\theta}\middle|\psi_n\right\rangle\left\langle\psi_n\middle|\frac{\partial\psi_0}{\partial\phi}\right\rangle$$

$$= \quad 2\frac{e^2}{\hbar}\,\mathrm{Im}\left\langle\frac{\partial\psi_0}{\partial\phi}\middle|\frac{\partial\psi_0}{\partial\theta}\right\rangle\,, \tag{5.5}$$

for given values of θ and ϕ. Because these values represent an arbitrary choice of gauge and the system is free to explore all such choices freely, the actual value of the transverse conductivity (i.e. the Hall conductivity) is the average of our calculated σ_{xy} over all values $0 \leq \theta < 2\pi$ and $0 \leq \phi < 2\pi$:

$$\sigma_{\mathrm{H}} = \frac{e^2}{\pi h}\int_0^{2\pi}\int_0^{2\pi}\mathrm{Im}\left\langle\frac{\partial\psi_0}{\partial\phi}\middle|\frac{\partial\psi_0}{\partial\theta}\right\rangle\,\mathrm{d}\theta\,\mathrm{d}\phi\,. \tag{5.6}$$

This equation, as yet, contains no reference to topological order and it still gives no indication as to why the Hall conductance should be quantised. To understand the final, topological component of the argument, it is helpful to recall the Gauss-Bonnet theorem, which describes a property of the Gaussian curvature, K, of surfaces in three dimensions [68]. Though the Gaussian curvature is only a local measure of the surface's curvature, the Gauss-Bonnet theorem shows that, for any closed surface, S, there is a universal relationship between the surface integral of K and the number, g, of holes or 'handles' enclosed by the surface, regardless of its shape:

$$\frac{1}{2\pi}\oint_S K\,\mathrm{d}S = 2\,(1-g)\ . \tag{5.7}$$

A sphere, for example, having no handles, has $g = 0$, while a torus has $g = 1$.*

An innovation of Berry [69–71] was to realise that a wavefunction of a particle undergoing an adiabatic evolution of its Hamiltonian, such that the Hamiltonian traverses a closed loop, l, in the space of its parameters, acquires a phase with a particular geometric component, now known as the Berry phase, here denoted γ_B. If we consider the Hamiltonian parameters B, θ & ϕ to span a toroidal space, with B as the minor radius, θ as the poloidal angle and ϕ as the toroidal angle, then for a given value of B, the full range of θ & ϕ describes the surface of a torus in this phase space. Adiabatically traversing a closed loop anywhere on this toroidal surface incurs a Berry phase which can be expressed as a surface integral on the torus:

$$\gamma_\mathrm{B} = -2\,\mathrm{Im}\int_{S_l}\sum_{n>0}\frac{\left\langle\psi_0\left|\,\frac{1}{B}\frac{\partial\mathcal{H}}{\partial\theta}\,\right|\psi_n\right\rangle\left\langle\psi_n\left|\,\frac{1}{R+B\cos\theta}\frac{\partial\mathcal{H}}{\partial\phi}\,\right|\psi_0\right\rangle}{(E_0-E_n)^2}\,\mathrm{d}S\ , \tag{5.8}$$

where S_l is the part of the toroidal surface that is enclosed by l and R is the major radius of the torus (we choose $R > B$ so that the torus is a ring, but R has no physical meaning and, since $\mathrm{d}S = B\,\mathrm{d}\theta\cdot(R + B\cos\theta)\ \mathrm{d}\phi$, all factors of R cancel anyway). It was realised by Simon [72] that, in the limit of an infinitesimally small loop, the Berry phase divided by the area enclosed by l has the form of a curvature in parameter space, analogous to the Gaussian curvature in real space. This is

* A teapot (here's my handle, here's my ~~spout~~ *other handle*) has $g = 2$.

known as the Berry curvature, $K_\mathrm{B} = \frac{\partial \gamma_\mathrm{B}}{\partial S}$. As a generalisation of the Gauss-Bonnet formula, it is possible to deduce an integral identity similar to equation 5.7:

$$\frac{1}{2\pi} \oint_S K_\mathrm{B} \, \mathrm{d}S = c \, , \tag{5.9}$$

where S is the entire surface of the parameter-space torus and c, the Chern number, is an integer. This is known as the Gauss-Bonnet-Chern formula. Since K_B is not the Gaussian curvature, c does not count handles. It turns out that the Chern number counts the values of B, not lying within the region of parameter space enclosed by S, where the energy of the ground state would cross that of another state, so that there is a degeneracy of the ground state [69]. As B increases, S expands. Each time B passes through a value B_d corresponding to a ground state degeneracy, the torus with minor radius B_d becomes enclosed by S and the Chern number decreases by 1.

The relevance of the quantisation of the Chern number to the observed quantisation of the Hall conductance is straightforward. By substituting γ_B from equation 5.8 into equation 5.9 and comparing with equations 5.4 & 5.6, we obtain

$$\frac{1}{2\pi} \oint_S K_\mathrm{B} \, \mathrm{d}S = \frac{1}{\pi} \int_0^{2\pi} \int_0^{2\pi} \mathrm{Im} \left\langle \frac{\partial \psi_0}{\partial \phi} \middle| \frac{\partial \psi_0}{\partial \theta} \right\rangle \mathrm{d}\theta \, \mathrm{d}\phi \, , \tag{5.10}$$

and hence

$$\sigma_\mathrm{H} = \frac{e^2}{h} c \, . \tag{5.11}$$

This explains why, as the magnetic field is varied, the Hall conductance makes a step change every time a Landau level crosses the Fermi surface. In between Landau level crossings, the remarkably constant Hall conductivity is guaranteed by the requirement that the Chern number is a topological invariant.

5.1.2 *Living on the edge—topologically protected surface states*

When the Fermi level lies between two Landau levels, we would expect the sample to behave as an insulator because there are no available low-energy states at the Fermi surface. The observation that there is actually a non-zero Hall conductance seems paradoxical—where does the transverse current flow? The answer is provided by examining the edges of the sample. Between the interior of the sample and the surrounding vacuum, the quasiparticle Hamiltonian must evolve from the form in equation 5.1 to its vacuum form. This deformation necessarily results in the Chern number changing to $c = 0$ (there is no quantised Hall conductance in the vacuum) and, since changes of the Chern number are related to crossings of the ground state energy level, there must therefore be one or more energy level crossings at the sample edge [73]. The implication is that the edge has a different bandstructure to the bulk, with the Fermi level no longer lying in an energy gap. Consequently, there are low-energy states that can carry a current.

The edge current can be pictured semi-classically by imagining the quasiparticles performing their cyclotron orbits, with radius $r_c = \frac{m^* v}{eB}$. Those particles within $\sim r_c$ of the sample edge have their trajectory interrupted when they strike the edge and they start again, hopping along the sample edge in a sequence of aborted

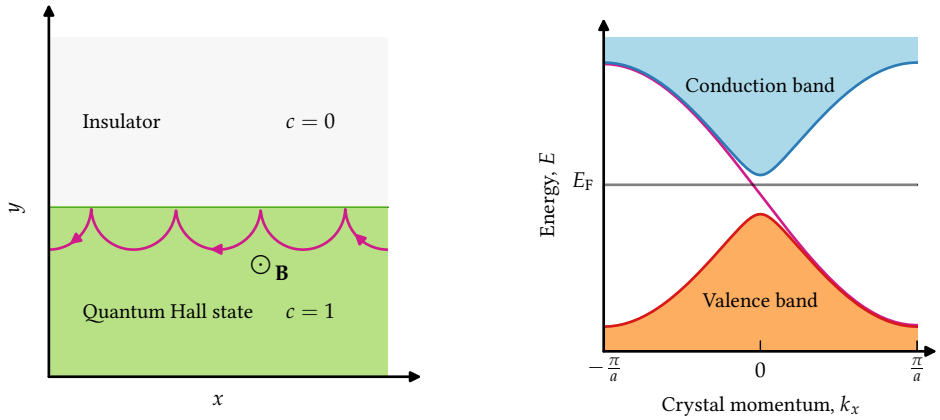

(a) Edge of a quantum Hall state

(b) Schematic edge bandstructure

Figure 5.1: Section of edge of a quantum Hall state. a: At the edge of the state, the Chern number, c, undergoes a step change. The interrupted cyclotron orbits of electrons at the edge are shown, forming a one-way current along the sample edge; b: Schematic bandstructure at the sample edge, showing the bulk (insulator) structure augmented with a single edge state (pink) crossing the Fermi level with negative k_x, corresponding to the situation in (a). The number of such Fermi-level-traversing edge states is equal to the change Δc across the edge.

orbits (see figure 5.1). This edge current is chiral in the sense that it only travels one way around the sample, as governed by the sign of the magnetic field. The current, and hence the Hall conductance, is robust to disorder because there are no states available for backscattering of the quasiparticles. Furthermore, because the evolution of the Hamiltonian from the sample bulk to the vacuum causes a change of Chern number, regardless of the nature of the intermediary Hamiltonian, the conducting surface state is 'topologically protected'—i.e. in spite of any possible distortion of the surface bandstructure by damage, impurities, etc., there must exist a band crossing at the Fermi level.

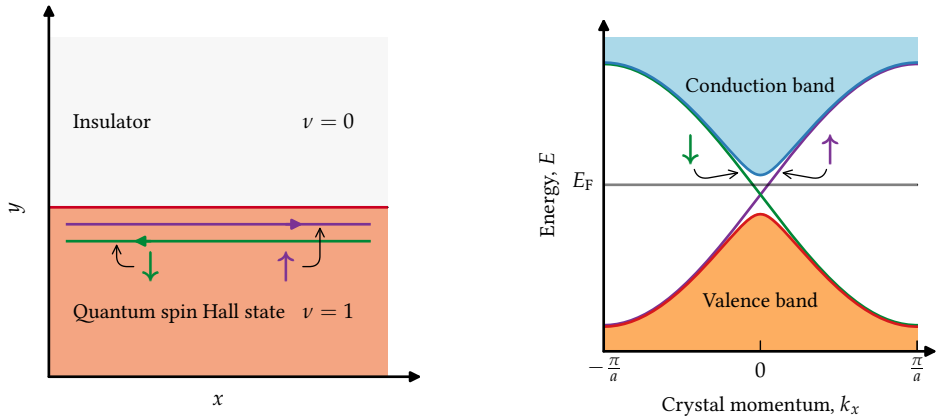

(a) Edge currents in a 2-D TI

(b) Schematic edge bandstructure

Figure 5.2: Section of edge of a quantum spin Hall (2-D TI) state. Up- and down-spins are indicated by purple and green arrows. a: At the edge of the state, the topological invariant undergoes a step change from $\nu = 1$ to $\nu = 0$. Currents of up- and down-spin flow around the sample edge in opposite directions;
b: The bandstructure at the sample edge, with the bulk (insulator) structure augmented with spin-polarised edge states crossing the Fermi level in a $\mathcal{T}$-symmetric pair.

5.1.3 *$\mathcal{T}$-symmetric topological order*

The existence of edge currents with this combination of topological protection and insensitivity to scattering is exciting because it can also be found in systems with no applied magnetic field [74]. In some such systems, a spin-orbit coupling term in the Hamiltonian, rather than the Lorentz force due to a magnetic field, is responsible for the topological edge state. For these systems, the topological invariant is no longer the Chern number of equation 5.9, but it can be deduced, by the same principle, from a surface integral of Berry curvature in the parameter space of the Hamiltonian. These two-dimensional systems turn out to have a topological invariant $\nu \in \mathbb{Z}_2$ (i.e. it can only take value 0 or 1) [75]. Unlike in the case of the quantum Hall effect, the surface state in such systems is time-reversal invari-

ant ($\mathcal{T}$-invariant) and the surface quasiparticles' spin and crystal momentum are coupled such that the spin is perpendicular to the crystal momentum with a particular handedness. Consequently, the currents associated with the two spin states have opposite chirality—spin-up quasiparticles travel one way around the edge and spin-down particles travel the other way. For each spin-up state at $\mathbf{k}$, there is a corresponding spin down state at $-\mathbf{k}$ (see figure 5.2). Because backscattering now requires impurities that can couple to the spin, i.e. scattering sites with a magnetic moment, the spin currents are still very robust in the absence of magnetic impurities, much like the edge currents in the quantum Hall effect. This is known as the quantum spin Hall effect.

It turns out that many different systems with a bulk energy gap at the Fermi level, including band insulators and superconductors, can display topologically protected conducting edge states. The quantum Hall effect and quantum spin Hall effect are special cases and, collectively, these systems are called topological insulators (TIs) and topological superconductors [74, 76–78] (in fact, the quantum spin Hall effect is often now commonly referred to as the 2-D TI). Apart from simply being an exciting new plaything for condensed matter physicists, TIs are of particular interest for the suggestion that they might have future technological uses. Amongst other possibilities, they could be exploited for a very robustly reproducible magnetoelectric effect that could find application in information storage technologies [77], and the boundary between a TI and a non-topological superconductor may provide a way of realising a Majorana fermion, potentially providing a highly fault-tolerant qubit for quantum computation [79–81].

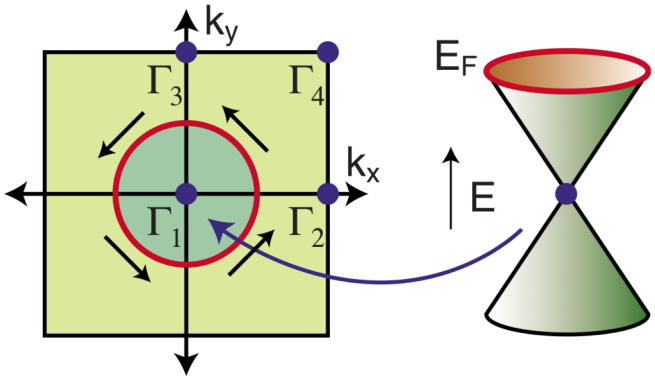

(a) 3-D TI Fermi surface (b) Bandstructure

Figure 5.3: Schematic bandstructure of a strong 3-D TI with a single Dirac point. a: First Brillouin zone, showing idealised circular Fermi surface and spins (black arrows) locked to $\mathbf{k}$; b: Bandstructure in the form of a Dirac cone, with Fermi energy E_F above the Dirac point at Γ_1. *Reproduced from [74].*

5.2 THREE-DIMENSIONAL TOPOLOGICAL INSULATORS

The predictions [82–84] and early observations [85, 86] of 2-D TIs piqued the interest of both theorists and experimentalists in the nascent field of TI research. Much interest focussed on the realisation of a 3-D TI. These systems are governed by four $\mathbb{Z}_2$ topological invariants, often grouped as $(\nu_0; \nu_1\,\nu_2\,\nu_3)$. The Brillouin zone of the surface bandstructure is naturally two-dimensional and contains four $\mathcal{T}$-invariant points (labelled Γ_1–Γ_4 in figure 5.3), where the surface states must necessarily be Kramers degenerate. The surface bandstructure therefore resembles a set of Dirac cones (the dispersion of massless Dirac fermions), with an apex (a Dirac point) at each of these locations. The manner in which these Dirac points are connected in the surface bandstructure has significant implications for the nature of the surface state. If the surface state Fermi surface encloses an odd number of Dirac points, the surface state must necessarily connect them in a topologically

non-trivial way. This is represented by a value $\nu_0 = 1$ and implies that there can be no gap in the surface bandstructure. If the Fermi surface encloses an even number of Dirac points, the crossings of the surface state through the Fermi surface will be topologically trivial. This is encoded as $\nu_0 = 0$ and indicates that the surface bandstructure may be deformed in such a way as to result in an energy gap [74].

3-D TIs therefore fall into two classes according to the value of ν_0, so-called 'weak' ($\nu_0 = 0$) and 'strong' ($\nu_0 = 1$) TIs. Weak 3-D TIs are equivalent to a stack of 2-D TI layers, in which case ν_1, ν_2 & ν_3 are very similar to the 2-D TI invariant, ν, and are akin to Miller indices, indicating the plane in which 2-D-like TI behaviour occurs. Because transport in weak TIs is only topologically protected in directions perpendicular to $(\nu_1\,\nu_2\,\nu_3)$, they do not share the robustness to disorder of an isolated 2-D state. Strong 3-D TIs more closely resemble a higher-dimensional extension of the 2-D case, with robust topologically protected conducting surface states [74, 77, 87]. Of course, the direction of $\mathbf{k}$ can now lie anywhere in the plane of the surface but the direction of the spin, which also lies in the surface plane, is still locked to $\mathbf{k}$ such that they are perpendicular with a particular handedness. This is because the topological protection is still governed by the spin-orbit interaction. As such, the surface spin currents are insensitive to $\mathcal{T}$-invariant back-scattering, just as in the 2-D case, and $\mathcal{T}$-invariant processes that result in scattering of less than 180° are suppressed according to the projection of the spin before and after scattering [78, 87].

5.2.1 *Common TI measurement techniques—surface spectroscopy*

Because the topologically protected conducting states in a TI are at the surface of the material, they are ideally suited to investigation using surface spectroscopy techniques, such as angle-resolved photo-emission spectroscopy (ARPES) [88, 89] and scanning tunnelling spectroscopy (STS) [90, 91].

ARPES makes use of the photoelectric effect, typically exciting photoelectrons with X-rays. Their energy and momentum are measured with an analyser, in which the photoelectrons are separated according to their energy and angle of emission by means of the electric field between two charged plates. The preferred apparatus is usually a spherical deflection analyser, wherein the plates are concentric hemispheres, between which the photoelectrons pass. Spin polarisation can be measured by means of a polarimeter, such as a Mott polarimeter, which exploits the spin-orbit interaction between the high-energy electrons and the ionic nuclei in a high-atomic-number target.

STS is an extension of scanning tunnelling microscopy (STM). By varying the bias voltage between the sample and the STM tip, the density of states can be measured as a function of energy. By performing a Fourier transform of the spatial modulation of the tunnelling amplitude, one can also deduce the **k**-dependent dispersion relation in the plane of the surface [92]. Coating the STM tip in a magnetic material creates an effective spin-valve, discriminating between different spin states of the tunneling electrons and allowing resolution of the spin-dependence of the quasiparticle bandstructure.

Both of these techniques have been much used in the discovery and characterisation of strong TIs, including $Bi_{1-x}Sb_x$ [93], Bi_2Se_3 [94–102], Bi_2Te_3 [97, 103–106] and SmB_6 [107–112].

5.2.2 *Experimental observation of 3-D TIs*

Following a very detailed theoretical prediction [113], the first strong TI to be discovered was the alloy $Bi_{1-x}Sb_x$ [93, 114–116], which has topological invariants $(\nu_0;\nu_1\,\nu_2\,\nu_3) = (1;1\,1\,1)$. However, the surface conduction of this alloy, like that of pure bismuth, is complicated by the presence of other surface states, which have their spin-degeneracy lifted by a strong Rashba effect [117, 118]. These too allow conduction on the surface and, though they don't cross between the valence and conduction bands, they confuse both the transport and the spin-polarised surface spectroscopy.

Predictions were also made that strong TI behaviour might be observed in certain selenide and telluride compounds [103, 113] including Bi_2Se_3 and Bi_2Te_3. These are compounds with a tetradymite structure, consisting of stacked quintuple-layers (e.g. Se–Bi–Se–Bi–Se). Consequently they cleave easily to expose the **c**-normal surface, with the **a**-**b** plane having hexagonal symmetry. Observation of the predicted effect followed very shortly for Bi_2Se_3 [94] and Bi_2Te_3 [104, 105]. These materials have a much less complicated surface bandstructure than $Bi_{1-x}Sb_x$ and have the additional advantages of a larger bandgap, with higher bulk resistivity and thereby the possibility of observation of TI behaviour at room temperature, and a more easily synthesised stoichiometric composition. The cleaner surface states mean that

the Dirac cones in the $\mathbf{a}^*$-$\mathbf{b}^*$ plane are very clearly seen in the surface spectroscopy. In Bi_2Te_3 the Dirac point is above a local trough in the valence band and below the energy of the valence band maximum, making it harder to tease out the Dirac-fermion-like behaviour expected of the low-energy surface states. Furthermore, the Dirac 'cone' is not very conical, with a strong hexagonal distortion of the $\mathbf{a}^*$-$\mathbf{b}^*$ cross-section. In contrast, in Bi_2Se_3 the Dirac cone is very circular and the Dirac point lies well within the bandgap, with an almost linear dispersion, such that the low-energy states approximate quite well the behaviour described by the massless Dirac Hamiltonian.

Unfortunately, as-grown Bi_2Se_3 and Bi_2Te_3 contain naturally-occurring structural defects that tend to pin the Fermi level in the bulk conduction band [78, 119]. As such, the surface transport properties tend to be swamped by the metallic behaviour of the bulk. Though careful doping has allowed some transport studies [95, 120, 121], the bulk contribution must be carefully subtracted to accurately examine the surface transport. Furthermore, sensitivity to air makes accurate doping control particularly difficult. For these reasons, the search for an ideal test-bed for strong TI behaviour continues.

5.3 SAMARIUM HEXABORIDE

The rare earth hexaborides are a family of compounds that have been of significant interest for decades for their complex magnetic properties and bandstructure [122, 123]. It has been proposed that some materials in this family should have the

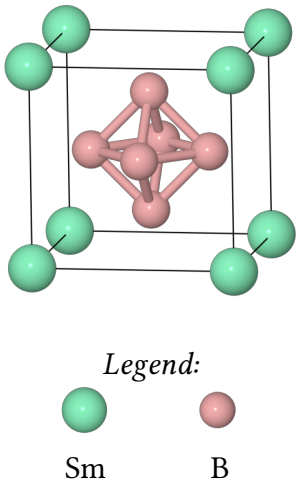

Figure 5.4: The simple-cubic unit cell of SmB_6. The lattice parameter is $a = 4.13\,\text{Å}$, with little variation over a wide temperature range [124].

characteristics of strong TIs and that SmB_6 in particular may be a good candidate system for exploring the non-trivial transport properties of such systems.

5.3.1 *General properties of rare earth hexaborides*

The binary rare earth hexaborides all share the same simple cubic crystal structure. It consists of a boron octahedron at the body centre, surrounded by rare earth ions, as illustrated in figure 5.4. The boron octahedron is nominally deficient of two electrons, while the rare earths have various valencies in these compounds [122]. Europium and ytterbium each supply a divalent ion and their hexaborides are consequently semiconducting or semi-metallic [125]. Most other rare earths are trivalent, yielding good metal hexaborides [126]. The exception is SmB_6, in which the samarium ions are of mixed divalent ($4f^6$) and trivalent ($4f^5$) electronic configuration in the approximate ratio 3:7 [127, 128].

5.3.2 *Magnetism and the lattice Kondo effect*

Most of the rare earth hexaborides exhibit antiferromagnetism, though EuB_6 displays ferromagnetism. More subtle magnetic behaviour is seen in CeB_6 and SmB_6, however [122, 123]. In these materials, magnetism is quenched by the lattice Kondo effect [53, 129], wherein the magnetic $4f$ ions of the lattice interact strongly with the spins of the conduction electrons. At low enough temperatures, below a characteristic Kondo temperature T_K, the lattice spins become screened by the conduction electrons. The spin of each magnetic ion becomes effectively dissolved in the conduction sea as one or more magnetic excitations, bearing charge inherited from the screening electrons. These excitations behave as quasiparticles, referred to as heavy fermions for their very large effective mass [130]. CeB_6 and SmB_6 are believed to be heavy fermion materials [122, 123]. The hybridisation of the ionic $4f$-orbitals with the conduction band also manifests itself as the opening of a narrow gap in the bandstructure, the Kondo gap. The position of the Kondo gap is such that when each rare earth ion contributes a single heavy electron, the Fermi level lies in the gap and the new valence band is completely filled. Materials displaying the semiconductor-like behaviour associated with this gap are known as Kondo insulators [130, 131]. When each rare earth ion contributes more than one heavy electron, the conduction band is part filled and the resulting Kondo metal typically shows resistivity with a characteristic logarithmic temperature dependence,

$$\rho \propto \ln\left(\frac{T_K}{T}\right) . \tag{5.12}$$

Since the first measurements of resistivity and Hall effect in SmB_6, there has been much debate about the causes of its puzzling transport behaviour, particularly at low temperature [128, 132–134]. SmB_6 is now understood to be a Kondo insulator [135]. Its transport properties between $10\,\mathrm{K} \lesssim T \lesssim 30\,\mathrm{K}$ simply resemble a semiconductor with a bandgap of $\sim$ 5–7 meV [133, 134, 136–138]. This is supported by low-temperature optical reflectivity [139] and tunnelling spectroscopy measurements [140]†.

5.3.3 *Topological complications*

In Kondo insulators, the Fermi level is expected to sit in the middle of the hybridisation gap, so one would naively predict SmB_6 to have the characteristics of a very cleanly intrinsic semiconductor. Deviation from semiconducting behaviour at lower temperatures, with an apparent plateau in the conductivity below $\sim 3\,\mathrm{K}$ [136, 142] (see figure 5.5), remained unexplained until the extension of topological band theory from conventional band insulators to Kondo insulators [143, 144] led to the prediction that SmB_6 should be a strong TI, with topological invariants $(\nu_0;\nu_1\,\nu_2\,\nu_3) = (1;1\,1\,1)$ [135, 145, 146]. The small Kondo gap means that thermal population of the bulk conduction band dwarfs the surface state population at higher temperatures. Hence the transport behaviour resembles a conventional Kondo insulator, except at the lowest temperatures. More recent transport studies have exploited unusual sample geometries to tease apart the surface and bulk

† It is worth noting that some surface spectroscopy measurements, notably several ARPES studies, suggest a larger bandgap of $\sim$ 18–24 meV [107, 108, 111, 141], almost certainly because the resolution of these experiments is coarser than the 2–7 meV that would be required to resolve the smaller bandgap [123].

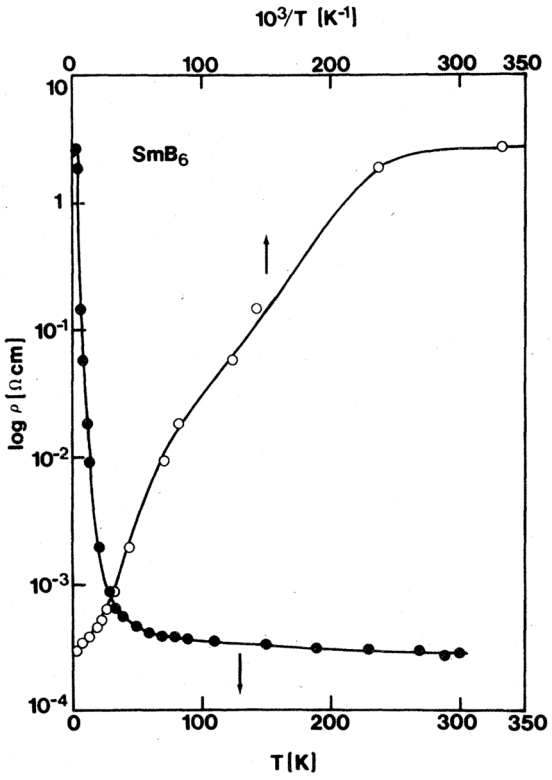

Figure 5.5: Temperature dependence of resistivity of SmB_6. *Reproduced from [134].*

contributions to the conductivity. They show convincingly that surface transport is responsible for the low temperature conductivity plateau and strongly support the strong TI hypothesis [137, 138, 147].

A number of surface spectroscopy studies have been conducted that also lend weight to the evidence for SmB_6 being a strong TI [135]. They confirm that the Kondo hybridisation gap is fully established in the bulk bandstructure below $\sim$ 30 K and that there are coexistent conducting surface states with spin-momentum chirality [108, 110–112]. ARPES studies have revealed three Fermi surface pockets, one around the $\overline{\mathbf{\Gamma}}$ point and one around each of the two $\overline{\mathbf{X}}$ points in the first Brillouin zone of the surface [111], as shown in figure 5.6. This confirms the prediction of strong TI behaviour and is in good qualitative agreement with bandstructure cal-

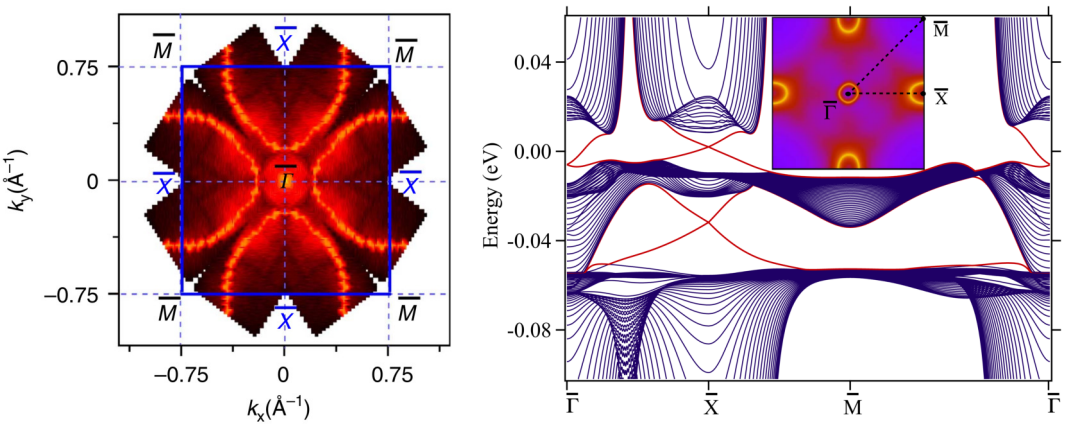

(a) Fermi surface of the surface state (b) Calculated bandstructure

Figure 5.6: a: Fermi surface of the SmB_6 surface state, deduced from ARPES measurements on the $(0\,0\,1)$ face. *Reproduced from [111]*;
b: Calculated bulk (blue) and surface (red) bandstructure of SmB_6 and (inset) calculated Fermi surface for the $(0\,0\,1)$ face. *Reproduced from [146].*

culations [146]. However, with state-of-the-art ARPES, it is currently very difficult to resolve the small Kondo gap in this material, which rather tests its utility as a fail-safe probe of strong TI behaviour [135, 148].

STM studies of SmB_6 surfaces have shown that this material rarely cleaves with pristine termination, such as preserve at the surface the symmetry of the bulk. Instead, a number of different reconstructed surfaces have been observed [149, 150]. This mixture of terminations suggests that the ARPES data should be interpreted with caution, as the spot size in an ARPES measurement is large enough that it may illuminate several regions of differing termination [135]. Nevertheless, STS shows a well established hybridisation gap, at an energy level that depends on the termination, with residual spectral weight that might be attributed to the in-gap surface states. This appears to be the case on all surfaces, regardless of termination type, which supports the concept of a protected state robust to surface imperfections [149]. Similar behaviour has been seen with point-contact spectroscopy [107].

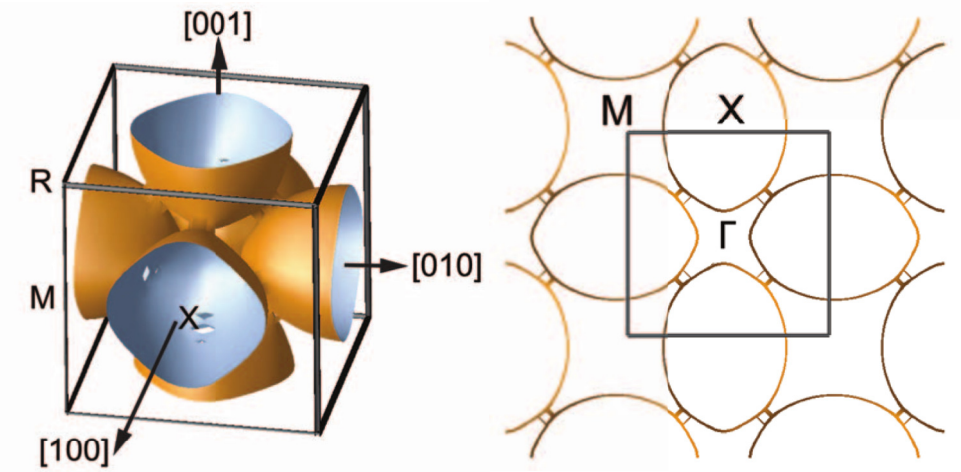

(a) Bulk Fermi surface (b) Cross section

Figure 5.7: a: Fermi surface of bulk SmB_6, calculated using density functional theory with a downward shift of the Fermi energy from its calculated position within the gap to expose the unhybridized bands. The Fermi surface consists of large multiply connected prolate spheroids centred at the **X** points of the Brillouin zone. This Fermi surface appears to be consistent with high frequency quantum oscillations measured using high magnetic fields.
b: Cross section in the **ΓXM** plane, showing more clearly the connecting necks. The Brillouin zone is shown as a black wire cage in (a) and a black square in (b). *Reproduced from [153].*

Helical coupling of spin and crystal momentum has not yet been observed though, so strong TI behaviour has not been demonstrated conlusively [135].

Topological insulators ought to show pronounced weak anti-localisation (WAL) in the transverse magnetoresistance, due to the strong spin-orbit coupling that underlies the geometric phase of the wavefunction [151]. Though early magnetoresistance studies of SmB_6 above 4 K gave no indication of WAL [152], later studies suggest that it is only significant at temperatures below 3 K and is very difficult to resolve, even below ∼1 K where surface conduction dominates [138].

Torque magnetometry has yielded quantum oscillations, which have been interpreted in different ways by various authors. One school of thought holds that the

oscillations arise from the surface state Fermi surface, consistent with the picture of SmB_6 as a topological Kondo insulator [154]. However, measurements made at high fields show additional frequencies of quantum oscillation that appear similar to those observed in other, non–Kondo insulator hexaborides such as LaB_6, CeB_6 and PrB_6. This has led to the suggestion that these oscillations are somehow arising from the gapped bulk states (see figure 5.7) [153]. Furthermore, the temperature-dependence of the amplitude of the quantum oscillations at dilution refrigerator temperatures cannot be explained with current models and, while there have been measurements of de Haas–van Alphen (magnetisation) oscillations in SmB_6, no Shubnikov–de Haas (conductivity) oscillations have yet been observed. A number of different theories have been suggested to explain these phenomena, ranging from simple models of heavy fermion systems in which the cyclotron energy exceeds the hybridisation gap [155], to more exotic scenarios such as the existence of a novel charge-neutral quasiparticle in the bulk, with appreciable non-zero density of states at the Fermi surface [153]. This latter theory appears to run counter to the conclusions drawn from transport measurements and, if true, would likely be the first mechanism of its kind reported. Evidence for neither the surface nor the bulk model is conclusive and remains the subject of active experimental and theoretical investigation and much debate [148, 156–159].

In summary, transport studies seem strongly suggestive of a topological surface state in SmB_6, whereas more direct probes of the Fermi surface and density of states, including surface spectroscopy and quantum oscillations, are still subject to experimental limitations and differing interpretations. Nevertheless, the fact that stoichiometric SmB_6 is relatively straightforward to produce and not appreciably air-sensitive [136, 160] makes it an appealing subject of further study and a very

promising test-bed for investigations into the properties of transport in strong TIs. In the topological Kondo insulator model of SmB_6, it seems that the Kondo hybridisation origin of the insulating behaviour constrains the Fermi level to sit within the bulk bandgap. Consequently, the transport properties do not suffer from the pollution of the surface phenomena with bulk transport, as is so often the case in Bi_2Se_3 and Bi_2Te_3. Though the small bandgap in SmB_6 necessitates quite low temperatures in order to view unadulterated surface transport, this is balanced by the ease of working with such a chemically stable compound. For these reasons, SmB_6 presented an ideal system for our own investigation, detailed in chapter 6, which aimed to better understand the nature of transport in this material and the extent to which topological protection plays a role.

6

USING MOLECULAR MAGNETS TO PROBE SURFACE TRANSPORT IN SAMARIUM HEXABORIDE

Since the advent of research into topological insulators (TIs), of which an overview was presented in chapter 5, many innovative transport techniques have been devised to tease out the muddled properties of the bulk and the topologically protected surface state. This chapter presents the development of a new technique to examine the sensitivity of the surface states of possible strong 3-D TIs to magnetic versus non-magnetic impurities. By using single-molecule magnets (SMMs) as surface scatterers, we are able to do this less ambiguously than in previous studies. This chapter begins by explaining in more detail the motivation for the development of this technique and describing the key elements of the method. There follows a review of the key magnetic properties of SMMs and an introduction to the two SMM materials used in this study. We then give more detail of the technique and relate its application to transport measurments of SmB_6. The results of our measurements are strongly suggestive of a spin-polarised conducting surface state dominating transport at temperatures below about 3 K, very much supporting the model of SmB_6 as a topological Kondo insulator.

6.1 MOTIVATION

As mentioned in section 5.2.2, spectroscopic techniques cannot always easily distinguish between topologically protected surface states and spin-polarised states arising from other phenomena. Transport studies can be used to provide complementary information about the electron dynamics of strong TIs to investigate the topologically protected behaviour. As was described in section 5.1.3, the topological protection of surface transport in strong TIs is a consequence of the coupling of spin and crystal momentum for surface quasiparticles, so that scattering from $\mathcal{T}$-invariant defects is suppressed. Naturally, several studies have been performed to investigate this phenomenon by exploring the effect of magnetic impurities, both by synthesising strong TI materials with magnetic ion dopants [97, 101, 102, 161, 162] and by surface deposition of magnetic ions [96, 98–100, 163]. Inevitably however, such methods cannot cleanly isolate the influence of the magnetic part of the impurity potential on the transport properties, because the impurities also dope and distort the bandstructure. Studies have also been performed to explore the behaviour of TI/ferromagnet heterojunctions [164], but again the bandstructure at the interface is a distortion of the TI surface bandstructure. It would therefore be desirable to develop a technique wherein one can effectively switch magnetic interactions on and off independently of any electrostatic modifications to the electronic structure and dynamics of the TI. Here we describe transport measurements that exploit some unique properties of single-molecule magnets (SMMs) to achieve just such a distinction between the electrostatic and magnetic scattering contributions of a deposited surface coating.

6.2 METHOD

We have already described how SmB_6, a possible strong TI, is a good candidate test-bed for a low-temperature investigation of surface transport in such materials (see section 5.3). For this study, we selected two derivatives of the well-studied SMM $Cr_8F_8(O_2C\,{}^tBu)_{16}$, one of whch has a magnetic moment associated with its total molecular spin $S = \frac{3}{2}$ and the other has no magnetic moment in the ground state. Besides their distinct magnetic characteristics, these SMMs have very similar properties and are isoelectronic. One or another of these two substances were deposited as a coating on the surface of each of several samples of SmB_6 so that we might investigate independently their individual effect on surface transport. Because the two SMMs are fully expected to provide an equivalent electrostatic scattering potential, the comparison of the effect of the magnetic and non-magnetic molecules permits us to obtain a measure of the effect of the magnetic scattering potential alone.

The experiment was performed as follows. First, we obtained some high-quality single-crystal samples of SmB_6 and wired them with electrical contacts in an appropriate geometry for measurements of longitudinal resistance and Hall effect. We characterised various transport properties of these pristine samples, including the effect of breaking a sample in two to explore the relative contribution of bulk and surface quasiparticles to the transport properties. We then obtained samples of a diamagnetic and a paramagnetic SMM (Ga_7Zn and Cr_7Zn rings, see section 6.3.2 below) and deposited each on a previously characterised pristine sample of SmB_6 by thermal sublimation without removing the original electrical contacts.

The transport measurements were then repeated, using the same contacts, to ascertain independently what difference scattering from the diamagnetic material, Ga_7Zn, and the paramagnetic material, Cr_7Zn, had on surface conduction.

6.3 SINGLE-MOLECULE MAGNETS

Ferromagnetism and antiferromagnetism are conventionally thought of as properties of purely inorganic crystalline solids, consisting of extended lattices. Recently however, there has been a focus on compounds that are not inorganic. These include crystallised molecules of purely organic compounds, containing elements with only *s*- and *p*-electrons and having at least one unpaired electron, and also crystals of organometallic compounds in which metal coordination centres display magnetic ordering mediated by superexchange through organic ligands [165–167]. The first organometallic molecular magnets to be explored were three-dimensional, notably including the thoroughly-studied family of Prussian blues [168], but subsequent investigations yielded lower-dimensional molecular magnets as well. At the zero-dimensional extreme are single-molecule magnets (SMMs) consisting of multiple transition metal or rare earth coordination centres with non-zero spin, bound together by various organic ligands [167, 169, 170]. In these compounds, there is no need to consider interactions through an extended lattice, the physics is determined by the intra-molecular interactions alone. These materials have attracted much interest, initially as bits for classical information storage [169] and, more recently, for the possibility of their application as qubits in quantum computation [171–174].

6.3.1 *The spin Hamiltonian*

In order to understand the magnetic properties of an SMM, it is necessary to examine the spin-dependent contribution, $\mathcal{H}_{\mathbf{S}}$, to the Hamiltonian. $\mathcal{H}_{\mathbf{S}}$ can usually, to good approximation, be modelled as a sum of contributions from the Zeeman effect, $\mathcal{H}_{\mathbf{B}}$, from the crystal field splitting, $\mathcal{H}_{\mathrm{cf}}$, and from the exchange interactions between the individual spin centres within the molecule, $\mathcal{H}_{\mathbf{J}}$:

$$\mathcal{H}_{\mathbf{S}} = \mathcal{H}_{\mathbf{B}} + \mathcal{H}_{\mathrm{cf}} + \mathcal{H}_{\mathbf{J}} \,. \tag{6.1}$$

For this model, the nuclear hyperfine interaction is assumed to be small enough that it can be neglected. Also, the orbital angular momentum of the spin centres is assumed to be quenched, at least to the extent that the orbital contribution to the total angular momentum and the spin-orbit interaction can both be treated as negligible perturbations in this approximation [167, 173–175].

Where the N individual spin centres are labelled with index $i \in \mathbb{Z}_N$ and have spin $\mathbf{s}_i$, the Zeeman term can, to first order in $\mathbf{s}_i$, be written as

$$\mathcal{H}_{\mathbf{B}} = \mu_{\mathrm{B}} \mathbf{B} \cdot \sum_{i=1}^{N} \mathbf{g}_i \cdot \mathbf{s}_i \,, \tag{6.2}$$

where $\mathbf{B}$ is the applied magnetic field and $\mathbf{g}_i$ is the effective gyromagnetic tensor at site i. $\mathbf{g}_i$ is a symmetric second-rank tensor that takes account of the fact that the existence of orbital angular momentum at site i can augment the effective magnetic field acting on $\mathbf{s}_i$. This enhancement may not be isotropic, so $\mathbf{g}_i$ encodes the anisotropy of the resultant Zeeman response.

The crystal field term accounts for the fact that electrostatic interactions in the neighbourhood of site i affect the energies of the different spin states. Electronic orbitals of the coordination centre, particularly the protruding d- and f-orbitals, overlap with the electron distribution of the surrounding ligands, introducing a different energy penalty to each orbital, which may be anisotropic. This affects the spin states of the coordination centre, since the shifted energies affect the application of Hund's first rule. In the absence of crystal field splitting, orbitals are populated so as to maximise multiplicity $(2s_i + 1)$ because this minimises the number of doubly occupied orbitals and the attendant electrostatic energy cost. When the crystal field is introduced, the energy cost of single occupancy of the highest-raised energy levels may be greater than the cost of double occupancy of lower-energy orbitals. The ground state of the coordination centre will then have a smaller value of s_i. To lowest order in $\mathbf{s}_i$, the corresponding Hamiltonian can be stated as

$$\mathcal{H}_{\text{cf}} = \sum_{i=1}^{N} \mathbf{s}_i \cdot \mathbf{D}_i \cdot \mathbf{s}_i \ , \tag{6.3}$$

where $\mathbf{D}_i$ is a symmetric, second-rank tensor. Naturally, $\mathbf{D}_i$ can be diagonalised by choosing to align the Cartesian basis of the each spin centre with the eigenvectors of $\mathbf{D}_i$. One can then express $\mathbf{D}_i$ as the sum of an isotropic contribution $\frac{1}{3}\,\text{Tr}(\mathbf{D}_i)\,\mathbb{1}$, and a traceless contribution $\mathbf{D}_i' = \mathbf{D}_i - \frac{1}{3}\,\text{Tr}(\mathbf{D}_i)\,\mathbb{1}$, where $\text{Tr}(\mathbf{D}_i)$ is the trace of $\mathbf{D}_i$. The isotropic component represents the mean energy shift, due to the crystal field, of all levels with a given value of s_i, and $\mathbf{D}_i'$ represents the splitting of these levels due to the anisotropy of the crystal field. Furthermore, since $\mathbf{D}_i'$ is a traceless, diagonal, second-rank tensor, it can only have two independent components and can be written as

$$\mathbf{D}_i' = \begin{pmatrix} D_i & 0 & 0 \\ 0 & E_i & 0 \\ 0 & 0 & -E_i \end{pmatrix} - \frac{1}{3} D_i \mathbb{1} \,, \tag{6.4}$$

where $D_i = D_{z_i z_i} - \frac{1}{2}\left(D_{x_i x_i} + D_{y_i y_i}\right)$ and $E_i = \frac{1}{2}\left(D_{x_i x_i} + D_{y_i y_i}\right)$, and $D_{x_i x_i}$, $D_{y_i y_i}$ and $D_{z_i z_i}$ are the on-diagonal components of $\mathbf{D}_i$. The basis $\{x_i, y_i, z_i\}$ can always be chosen in such a way that $-\frac{1}{3} \leq \frac{E_i}{D_i} \leq \frac{1}{3}$. The crystal field term in the spin Hamiltonian is now

$$\begin{aligned} \mathcal{H}_{\text{cf}} &= \sum_{i=1}^{N} \mathbf{s}_i \cdot \left(\mathbf{D}_i' + \frac{1}{3} \operatorname{Tr}(\mathbf{D}_i)\, \mathbb{1} \right) \cdot \mathbf{s}_i \\ &= \sum_{i=1}^{N} \left[D_i \left({s_{i,z_i}}^2 - \frac{1}{3} {\mathbf{s}_i}^2 \right) + E_i \left({s_{i,x_i}}^2 - {s_{i,y_i}}^2 \right) + \frac{1}{3} \operatorname{Tr}(\mathbf{D}_i)\, {\mathbf{s}_i}^2 \right] \\ &= \sum_{i=1}^{N} \left[D_i {s_{i,z_i}}^2 + E_i \left({s_{i,x_i}}^2 - {s_{i,y_i}}^2 \right) + E_i {\mathbf{s}_i}^2 \right] \,. \end{aligned} \tag{6.5}$$

$\frac{E_i}{D_i} = 0$ represents a spin anisotropy with axial symmetry, in which $D_i < 0$ corresponds to an easy axis anisotropy and $D_i > 0$ corresponds to an easy plane anisotropy. ${\mathbf{s}_i}^2$ commutes with $\mathcal{H}_{\text{cf}}$ but, unless site i has axial anisotropy, s_{i,z_i} does not commute with $\mathcal{H}_{\text{cf}}$, so the crystal field mixes the eigenstates of s_{i,z_i} and lifts their degeneracy.

The contribution to the Hamiltonian due to exchange interactions between different spin-centres within a SMM is represented by $\mathcal{H}_{\mathbf{J}}$. This tends to be very well represented as an expansion to first order in each of $\mathbf{s}_i$ and $\mathbf{s}_j$, where the indices i and j run independently over the spin centres:

$$\mathcal{H}_{\mathbf{J}} = \sum_{i=1}^{N} \sum_{j \neq i} \mathbf{s}_i \cdot \mathbf{J}_{i,j} \cdot \mathbf{s}_j \,. \tag{6.6}$$

The second-rank tensor $\mathbf{J}_{i,j}$ can be further expanded to illustrate the different exchange phenomena at work:

$$\mathcal{H}_{\mathbf{J}} = \sum_{i=1}^{N} \sum_{j \neq i} \left(-J_{i,j}\, \mathbf{s}_i \cdot \mathbf{s}_j \; + \; \mathbf{s}_i \cdot \mathbf{D}_{i,j} \cdot \mathbf{s}_j \; + \; \mathbf{d}_{i,j} \cdot \left(\mathbf{s}_i \times \mathbf{s}_j \right) \right) \; . \tag{6.7}$$

Here, the first term is familiar as the Heisenberg exchange interaction, which represents isotropic exchange, hence $J_{i,j} = -\frac{1}{3} \operatorname{Tr}\left(\mathbf{J}_{i,j}\right)$. The second term represents symmetric anisotropy in the exchange interaction, so $\mathbf{D}_{i,j}$ (not to be confused with the crystal field anisotropy tensor, $\mathbf{D}_i$, above) is a traceless, symmetric, second-rank tensor,

$$\mathbf{D}_{i,j} = \frac{1}{2} \left(\mathbf{J}_{i,j} + {\mathbf{J}_{i,j}}^{\mathrm{T}} \right) - \frac{1}{3} \operatorname{Tr}\left(\mathbf{J}_{i,j}\right) \mathbb{1} \; . \tag{6.8}$$

Like $\mathbf{D}_i$, $\mathbf{D}_{i,j}$ can be diagonalised with an appropriate choice of basis. The third term, the Dzyaloshinskii-Moriya interaction, represents antisymmetric anisotropic exchange, driven by spin-orbit coupling, which encourages a canting of the spins towards a mutually perpendicular orientation. This is represented by an antisymmetric contribution to $\mathbf{J}_{i,j}$, so

$$\mathbf{d}_{i,j} \cdot \left(\mathbf{s}_i \times \mathbf{s}_j \right) = \mathbf{s}_i \cdot \frac{1}{2} \left(\mathbf{J}_{i,j} - {\mathbf{J}_{i,j}}^{\mathrm{T}} \right) \cdot \mathbf{s}_j \; . \tag{6.9}$$

Because each individual spin has $2s_i + 1$ eigenstates, the eigenstates of the full spin Hamiltonian span a Hilbert space of $\prod_i \left(2s_i + 1\right)$ dimensions. The fact that the dimensionality of the Hilbert space rises exponentially with the number of spin centres makes numerical diagonalisation of the Hamiltonian a very computationally intensive problem for all but the smallest SMMs. However, a useful simpli-

fication can be made by noting that both the total spin $\mathbf{S} = \sum_i \mathbf{s}_i$ and (if the z_i-axes of the single-ion crystal field anisotropies are aligned) the total z-projection of the spin $S_z = \sum_i s_{i,z_i}$ commute with the Heisenberg exchange term*. In most circumstances, Heisenberg exchange is the dominant contribution and the anisotropic terms can be treated as a perturbation. The Hamiltonian then need only be block diagonalised, each block corresponding to a value of S and consisting of $2S + 1$ elements, in which the detailed structure of each block can be elucidated using raising and lowering operators. The molecule can then be treated as a single giant spin centre, described by a simplified Hamiltonian, amalgamating the crystal field and exchange anisotropy and the Zeeman effect, in what is known as the giant spin approximation:

$$\mathcal{H}_{\mathbf{S}} = D{S_z}^2 + E\left({S_x}^2 - {S_y}^2\right) + \mu_{\mathrm{B}}\mathbf{B}\cdot\mathbf{g}\cdot\mathbf{S}\,, \tag{6.10}$$

where D, E and $\mathbf{g}$ are analogous to D_i, E_i and $\mathbf{g}_i$ for a single ion.

6.3.2 *Cr/Ga antiferromagnetic rings*

One class of SMMs, known as antiferromagnetic rings, consists of near-planar ring-shaped clusters of spin centres with antiferromagnetic Heisenberg exchange coupling between nearest neighbours. $Cr_8F_8(O_2C\,{}^tBu)_{16}$ (hereafter referred to as Cr_8) is one such antiferromagnetic ring molecule. The molecule has four-fold rotational symmetry around the axis of the ring and the eight Cr^{III} ions form an almost-planar

* This is only strictly true if $J_{i,j}$ is independent of i & j, but even in a more realistic situation, where exchange is dominated by nearest neighbour interactions, it typically remains a good approximation.

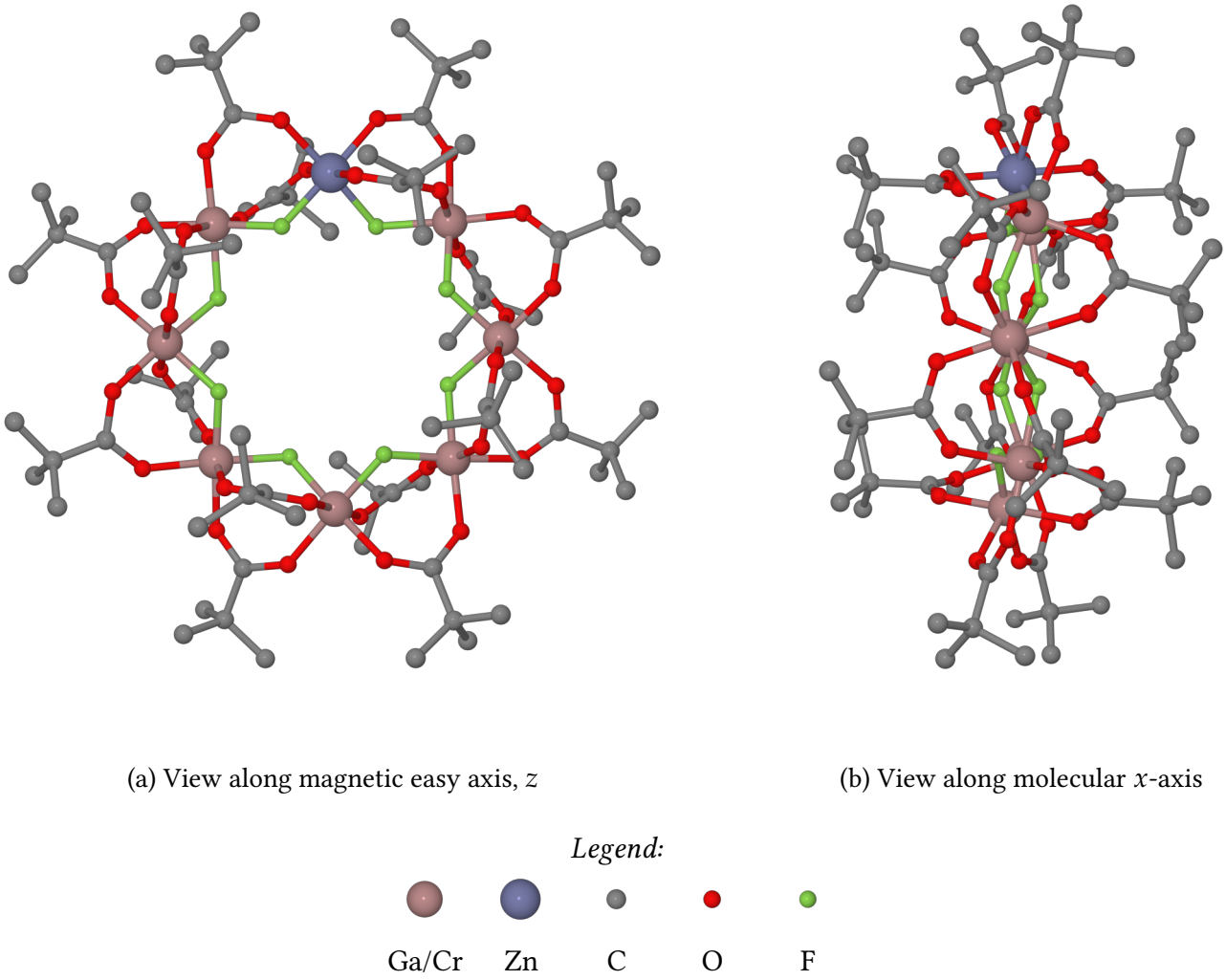

(a) View along magnetic easy axis, z

(b) View along molecular x-axis

Figure 6.1: The molecular structure of the $[M_7ZnF_8(O_2C\,{}^tBu)_{16}]^-$ ion, with M = Ga, Cr. For clarity, the hydrogen atoms in the *tert*-butyl groups have been omitted.
a: A view of the ion along its z-axis (the magnetic easy axis).
b: A view of the ion along its x-axis.
The nearest-neighbour separation of metal coordination centres is 3.4 Å. The ion is an almost planar octagon and, with a $(Me_2NH_2)^+$ cation at the centre of the ring (not shown), it forms the molecule $(Me_2NH_2)[M_7ZnF_8(O_2C\,{}^tBu)_{16}]$, referred to in the text simply as Ga_7Zn or Cr_7Zn, according to the identity of the metal ion M.
Structure data are adapted from the supplementary information to reference [176].

octagon [177]. Each has spin $s_i = \frac{3}{2}$ and the single-ion anisotropy at each of the two symmetry-independent sites has an easy axis aligned with the axis of the ring. Consequently, the ground state, $|0\rangle$, is a superposition of Néel states, i.e. states with $m_{s_i} = \pm\frac{3}{2}$, alternating around the ring,

$$|0\rangle = \frac{1}{\sqrt{2}}\left(|\Uparrow\Downarrow\Uparrow\Downarrow\Uparrow\Downarrow\Uparrow\Downarrow\rangle + |\Downarrow\Uparrow\Downarrow\Uparrow\Downarrow\Uparrow\Downarrow\Uparrow\rangle\right) . \tag{6.11}$$

The total spin in the ground state is therefore $S = 0$ but there is a rich structure of magnetic excitations [178], with the first excited state, having $S = 1$, at 0.80 meV $\equiv$ 9.3 K above the ground state [179, 180].

Although Cr_8 has $S = 0$ in the ground state, it is possible to synthesise modified structures, Cr_7M, with one of several species substituted for one of the chromium ions, often resulting in non-zero S [181]. In the case where a Zn^{II} ion is used in place of one of the Cr^{III} ions, the $Cr_8F_8(O_2C\,{}^tBu)_{16}$ molecule becomes a $[Cr_7ZnF_8(O_2C\,{}^tBu)_{16}]^-$ ion, depicted in figure 6.1. This is bound ionically to a cation such as $(Me_2NH_2)^+$, to form a new molecule $(Me_2NH_2)[Cr_7ZnF_8(O_2C\,{}^tBu)_{16}]$ (referred to in the following as Cr_7Zn). The antiferromagnetic coupling between the Cr^{III} ions in Cr_7Zn is not materially different to that in Cr_8, but the Zn^{II} ion has spin $s = 0$ so that the spins are not perfectly compensated, with a resultant total spin of $S = \frac{3}{2}$ in the ground state. Cr_7Zn inherits the easy axis anisotropy of Cr_8, aligned with the axis of the ring, but no-longer has rotational symmetry, the ground state having axial and rhombic zero-field splitting parameters $D = -51.90\,\mu eV$ and $E = -60.63\,neV$, respectively. Similarly to Cr_8, the first excited state in Cr_7Zn, with $S = \frac{1}{2}$, is 0.83 meV $\equiv$ 9.6 K above the ground state. Furthermore, one can synthesise another related compound, isoelectronic with

Cr_7Zn but with Ga^{III} in place of Cr^{III}, yielding $(Me_2NH_2)[Ga_7ZnF_8(O_2C\,{}^tBu)_{16}]$ (or, shorthand, Ga_7Zn). Because, like the Zn^{II} ion, the Ga^{III} ions have $s = 0$, Ga_7Zn is devoid of magnetic structure, so that it has $S = 0$ and is simply diamagnetic [176].

It has been demonstrated that Cr_7M-based antiferromagnetic ring SMMs are stable enough that they can be heated to temperatures in excess of 230 °C without causing any change in the molecular structure. This makes them suitable for deposition on surfaces by thermal sublimation [182]. On some surfaces, and with carefully chosen ligands, they can even be made to self-assemble into thin films. The magnetic properties of the rings remain fundamentally unchanged by the deposition, regardless of the surface environment [182], which demonstrates that, because of the size and stability of the molecule, no significant hybridisation with the conduction electrons in the surface is possible. Furthermore, as seen in figure 6.1, the magnetic ions are surrounded by a padding of quite large organic groups. This means there can be no substantive exchange coupling between the giant spin centres to promote inter-molecular magnetic ordering. For the same reason, it is unfeasible for a Ruderman-Kittel-Kasuya-Yosida (RKKY) interaction, mediated by the surface quasiparticles an SmB_6 substrate, to cause magnetic ordering in a Cr_7Zn coating [183]. In order to work out the strength of the dipole-dipole interaction of two adjacent $S = \frac{3}{2}$ molecules, we recall the form of the magnetic flux density $\mathbf{B}$ at a displacement $\mathbf{r}$ from a magnetic dipole $\boldsymbol{\mu}$,

$$\mathbf{B}(\mathbf{r}) = \frac{\mu_0}{4\pi}\left(\frac{3\,(\boldsymbol{\mu}\cdot\mathbf{r})\,\mathbf{r}}{r^5} - \frac{\boldsymbol{\mu}}{r^3}\right) . \tag{6.12}$$

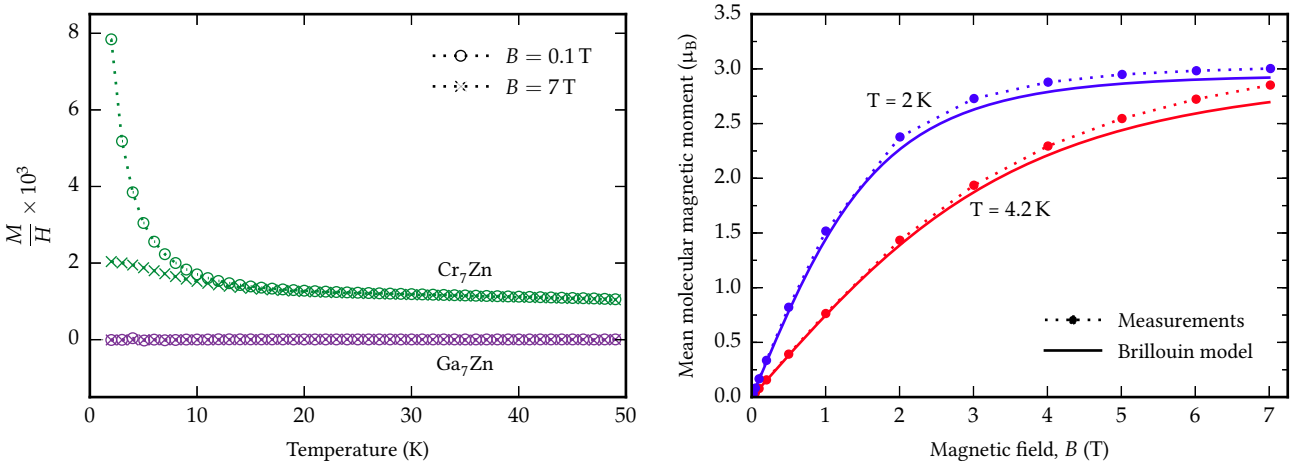

(a) Magnetisation M in applied field $B = \mu_0 H$

(b) Magnetic moment per molecule

Figure 6.2: Magnetisation of Cr_7Zn and Ga_7Zn, measured by SQUID magnetometry.
a: Temperature dependence. Ga_7Zn is clearly diamagnetic. The behaviour of Cr_7Zn is very close to Curie law behaviour at low temperatures but does not approach $M = 0$ at high temperatures;
b: Field dependence of Cr_7Zn magnetisation, expressed as magnetic moment per molecule, compared to the Brillouin function behaviour expected of a simple $S = \frac{3}{2}$ paramagnet.

Given the magnetic dipole moment of a spin, $\boldsymbol{\mu} = -\frac{g_S \mu_B}{\hbar}\mathbf{S}$, we obtain

$$\mathbf{B}(\mathbf{r}) = 0.49\frac{\mu_0 \mu_B}{\pi\hbar}\left(\frac{\mathbf{S}}{r^3} - \frac{3\,(\mathbf{S}\cdot\mathbf{r})\,\mathbf{r}}{r^5}\right)\,, \tag{6.13}$$

where we have taken the gyromagnetic ratio $g = 1.96$ [176]. In previous deposition studies, these molecules tend to lie with their z-axis normal to the surface of the substrate [182]. Since they have a crystallographic diameter of 1.9 nm in the x-y plane, the strength of the dipole-dipole interaction of neighbouring molecules will only be of order 1 mK. All evidence therefore suggests that an assembly of Cr_7Zn molecules, either crystalline or an amorphous surface coating, is simply paramagnetic, even at the temperatures of most cryo-magnetic measurements.

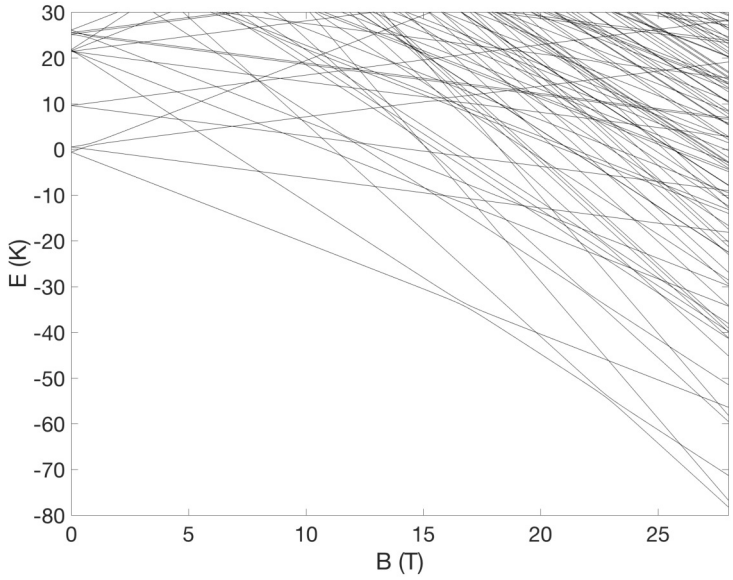

Figure 6.3: Calculated fine structure and Zeeman splitting of Cr_7Zn. Eigenvalues E of the Hamiltonian $\mathcal{H}_S$ (equation 6.10) as a function of magnetic field B. At zero field, the levels are grouped into multiplets corresponding to different values of the giant spin S. At higher fields, the Zeeman energy dominates.
Reproduced from [184] by kind permission.

The expected magnetic behaviour of crystalline Cr_7Zn and Ga_7Zn was confirmed by SQUID magnetometry measurements of powder samples, shown in figure 6.2. At all temperatures from 2 K to 300 K and in fields from 0 T to 7 T, Ga_7Zn only showed very weak diamagnetic behaviour, as seen in figure 6.2a, whereas Cr_7Zn was paramagnetic throughout. Below 5 K, the susceptibility of Cr_7Zn strongly resembles that of an ideal paramagnet, with each molecule contributing a magnetic moment corresponding to $S = \frac{3}{2}$. Without correcting for imperfect packing of grains in the powder sample, the measured Curie constant was $C = 15.7$ mK, close to the predicted value of 14.8 mK. The dependence of magnetisation of Cr_7Zn on field strength is depicted in figure 6.2b. The measured magnetisation is very close to the expected Brillouin function for an ideal $S = \frac{3}{2}$ paramagnet. Deviation at

higher fields can be explained by the fact that Zeeman splitting reduces the energy of field-aligned components of higer-S states to the extent that they have appreciable thermal population, slightly increasing the magnetisation. This can clearly be seen in the calculated energy level structure shown in figure 6.3, where levels from the $S = \frac{5}{2}$ and $S = \frac{1}{2}$ excited states become mixed with the highest levels of the $S = \frac{3}{2}$ ground state at fields as low as 5 T.

Cr_7Zn and Ga_7Zn are sufficiently identical in their electrostatic properties that they can easily be made to co-crystallise [176]. Because they are electronically so very indistinguishable but are magnetically distinct, Cr_7Zn and Ga_7Zn together form a perfect tool for exploring the sensitivity to magnetic scattering of topologically protected surface-state quasiparticles in a strong TI.

6.4 Ga_7Zn AND Cr_7Zn AS SURFACE SCATTERERS

6.4.1 *Provenance of samples*

The samples used in this experiment were grown by Shuhua Yao, Minhui Lu and Yan-Feng Chen at the National Laboratory of Solid State Microstructures, Nanjing University, in collaboration with Yulin Chen of the Clarendon Laboratory. High quality single crystals of SmB_6 were grown by spontaneous nucleation from high temperature solutions, using aluminium as the solvent. The starting materials were elemental samarium, boron and aluminium, each with a purity of 99.99 %. The molar ratio of solute to solvent was 1 : 10. The mixture was heated to 1500 °C and held at this temperature for 24 hours in an argon atmosphere to homogenize the

solution. Following this, the melt was cooled quickly to 1450 °C and then slowly to 700 °C. It was then allowed to cool to room temperature naturally. The aluminium flux was removed by dissolving in hydrochloric acid and single crystals of SmB_6 were obtained with sizes of up to 4 mm × 0.8 mm × 0.4 mm.

6.4.2 *Details of experiment*

In all, two iterations of this experiment were performed. For the first, we obtained a needle-shaped crystal of SmB_6, measuring 2.82 mm × 0.36 mm × 0.235 mm and with clean, shiny facets. The sample was mounted on a piece of amorphous quartz and seated on a socket for an eight-pin dual in-line package (DIP). 25 µm-diameter gold wire was used to connect each of the eight pins of the DIP socket to the sample surface, where the wires were fixed using a graphite paste conducting adhesive. The eight contacts were arranged on the top $(0\,0\,1)$ surface of the sample, as shown in figure 6.4. Measurements were then made of longitudinal and transverse resistance, including the temperature dependence of longitudinal resistance from 1.4 K to room temperature, longitudinal and transverse magnetoresistance in fields from 0 T to 15 T, and anisotropic magnetoresistance (AMR, see section 4.2) in a field of 15 T at various temperatures. The contacts were then removed and the sample cleaned and broken along a $(1\,0\,0)$ plane to form two needle-shaped samples, one with dimensions 1.40 mm × 0.36 mm × 0.235 mm and the other 1.42 mm × 0.36 mm × 0.235 mm. Each new sample was mounted on its own DIP socket and patterned with eight contacts in the same way as the parent sample,

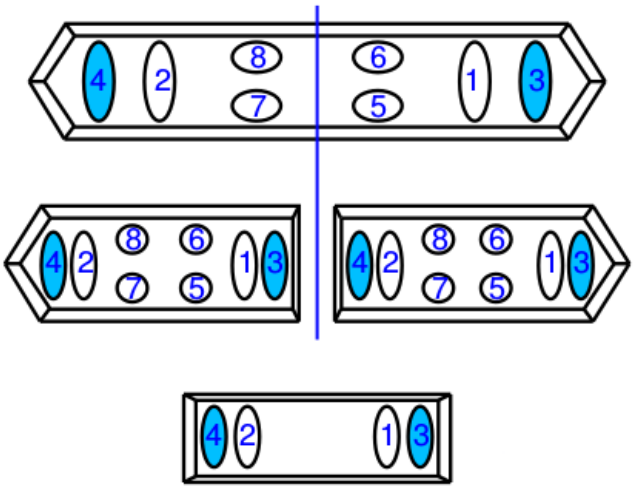

Figure 6.4: *Top:* Contact geometry on SmB_6 samples for the first iteration of the experiment. The initial sample is shown with eight contacts (ellipses numbered 1–8) for transport measurements. *Middle:* The sample having been cleaned and cleaved in two ($(1\,0\,0)$ cleavage plane denoted by blue line), each half was similarly prepared with eight contacts on the $(0\,0\,1)$ face for further measurements. *Bottom:* Contact geometry on each of the four SmB_6 samples for the second iteration of the experiment. Each sample was prepared with a simpler four-point pattern of contacts.
In each case, contacts 3 & 4 (light blue) served to carry the excitation current, while contacts 1, 2 & 5–8 were used to measure the induced potential in the sample surface.

as illustrated in figures 6.4 & 6.5. Further measurements of AMR and Hall effect were then made on each sample.

Once the samples had been characterised in their pristine state, SMM scatterers were deposited by thermal sublimation. The mounting of the wired SmB_6 samples on DIP sockets allowed them to be removed from the measurement apparatus, without disturbing the contacts and wiring, and transferred into an ultra-high vacuum chamber for SMM deposition. The samples of Ga_7Zn and Cr_7Zn were grown by Grigore Timco of the Molecular Magnetism Group in the School of Chemistry of the University of Manchester. Samples of both Ga_7Zn and Cr_7Zn from the same batches were previously the subject of an electron paramagnetic resonance spec-

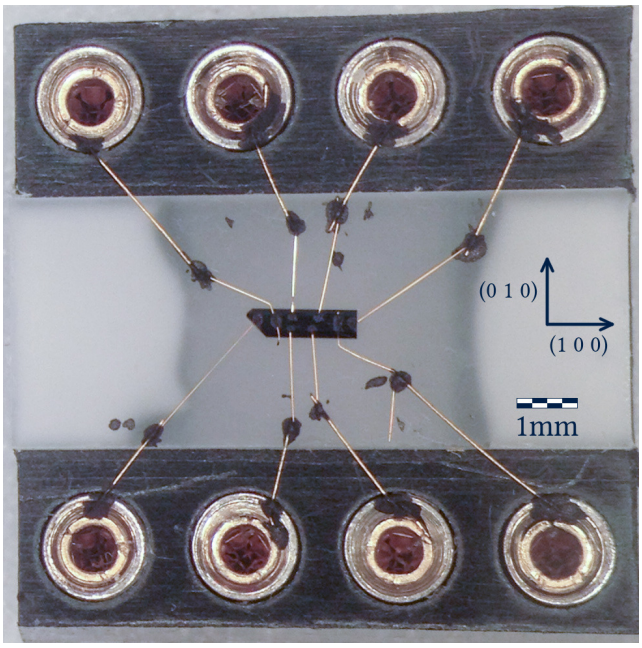

Figure 6.5: Photograph of a sample of SmB_6 prepared for measurement. This sample is one of the two obtained after cleaving the parent sample in the first iteration of the experiment. The crystal itself is the black oblong in the centre of the image, with the cleaved surface being at the right-hand end. The face on which the contacts are arranged is a $(0\,0\,1)$ plane. The crystal is fixed to a quartz plate and mounted on a DIP socket. It is wired for transport measurements, as illustrated in figure 6.4, and has been coated with Ga_7Zn to a thickness of 5 nm.

troscopy study [176], in which details of the synthesis have already been reported. Thermal deposition was performed by Christopher Muryn at the School of Chemistry of the University of Manchester in a manner very similar to that previously reported for Cr_7Ni heterometallic ring SMMs [182]. The mounted SmB_6 crystals were each held at $\sim 2 \times 10^{-8}$ mbar, at a distance of 10 cm from an ohmically heated crucible containing a crystalline powder of either Ga_7Zn or Cr_7Zn. The SMMs were sublimed in the temperature range 180–230 °C and the deposition rate was monitored using a quartz crystal microbalance. A total mass of SMM equivalent to a uniform surface coverage of 5 nm was deposited on each sample. After SMM deposition, further measurements of AMR and Hall effect were made, to complete the first iteration of the experiment. Unfortunately, some of the contacts were found to have broken, perhaps because the carbon paste was too fragile an adhesive to survive ultra-high vacuum and the thermal stresses of SMM deposition. This did not prevent our obtaining enough data to illustrate reasonably well the effect of Ga_7Zn and Cr_7Zn on transport in SmB_6, but prompted a repeat of the experiment, in order to check the validity of the results.

In this second iteration, four new single-crystal samples of SmB_6, with very similar appearance to the parent sample from the first iteration, were obtained from the same source. They were mounted in pairs on two DIP sockets, wired this time with a simpler four-contact geometry, as illustrated in figures 6.4 & 6.6. This precluded transverse transport measurements but permitted longitudinal transport measurements of twice as many samples, to serve as ample confirmation of the results of the first iteration. Additionally, instead of the fragile carbon paste adhesive, a stronger silver-based conductive paint, DuPont 4929N, was used.

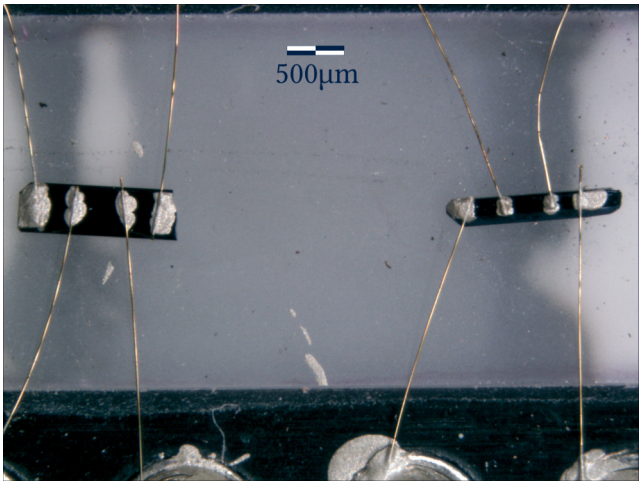

Figure 6.6: Photograph of one of the two pairs of SmB_6 crystals mounted for measurement in the second iteration of the experiment. The crystals are fixed to a quartz plate, mounted on a DIP socket. They are wired for transport measurements, as illustrated in figure 6.4, and have been coated with Cr_7Zn to a thickness of 5 nm. As in figure 6.5, the long axis of each crystal is the $(1\,0\,0)$ direction and the face with painted contacts is the $(0\,0\,1)$ direction.

As before, we first characterised the transport properties of the pristine samples. One pair of samples was then coated in Ga_7Zn and the other in Cr_7Zn, following exactly the same procedure as in the first iteration. Again, the change in the samples' transport behaviour was measured. One of the Ga_7Zn-coated samples was lost, again due to a poor-quality contact. The other Ga_7Zn-coated sample and both the Cr_7Zn-coated samples yielded good data. The Ga_7Zn-coated sample with good contacts was a short rod, measuring 0.99 mm × 0.34 mm × 0.326 mm. The Cr_7Zn-coated samples were a needle, measuring 2.01 mm × 0.31 mm × 0.212 mm, and a cuboid platelet, measuring 1.81 mm × 0.56 mm × 0.109 mm.

6.4.3 *Characterisation of uncoated SmB_6*

The temperature dependence of the resistance was measured from near room temperature to 1.4 K (figure 6.7). The data show behaviour very much consistent with previous reports [134, 136, 160, 185], with insulator-like behaviour between ∼40 K and ∼5 K, which may be attributed to the opening of a Kondo hybridisation gap in the bandstructure, and more complicated behaviour at lower temperatures, with resistances lower than expected for a simple Kondo insulator. By modelling the longitudinal conductance of a sample as a sum of independent parallel contributions from the surface and the bulk, a fit to these data can be attempted. The form of the fitted model of the bulk resistance is based on the expected behaviour of an intrinsic semiconductor, as derived from the law of mass action [186]. To reflect the expected behaviour at the lowest temperatures, quasiparticle-phonon scattering is assumed to be effectively frozen out, such that quasiparticle scattering is dominated by temperature-independent impurity scattering. It follows that the resistivity of the bulk has the form

$$\rho_b = \gamma_b T^{-\frac{3}{2}} \exp\left(\frac{E_g}{2k_B T}\right), \tag{6.14}$$

and the corresponding resistance is

$$R_b = C_b T^{-\frac{3}{2}} \exp\left(\frac{E_g}{2k_B T}\right), \tag{6.15}$$

where the coefficient C_b and the band-gap energy E_g are free parameters in the fit. Knowing the dimensions of the current path through the bulk, the sample-

independent resistivity parameter γ_b can be determined from C_b. Meanwhile, the behaviour of the surface resistance is appears to bear some resemblance to that of a Kondo metal (see section 5.3.2). A good fit was obtained with a surface resistance of the form

$$R_s = C_s \ln\left(\frac{1\,\mathrm{K}}{T}\right) + D_s\,, \tag{6.16}$$

where

$$D_s = C_s \ln\left(\frac{T_K}{1\,\mathrm{K}}\right) + (\text{other contributions})\,. \tag{6.17}$$

The parameters C_s and D_s are fitting parameters and T_K is the Kondo temperature (see section 5.3.2). The total fitted longitudinal resistance is therefore

$$R_{xx} = \left({R_b}^{-1} + {R_s}^{-1}\right)^{-1}\,. \tag{6.18}$$

Because surface conduction is highly non-local, with significant contributions to the conductance from current paths that go 'the long way around', across the entire sample surface [137, 138, 147], C_s and D_s are expected to be strongly dependent on the sample geometry and this means it is not easily possible to deduce a sample-independent surface parameter, analogous to γ_b, for direct comparison of different samples. Nevertheless, such a fit allows one to compare bulk parameters to check for consistency between samples. Since the contact positions on a given sample are unaltered before and after the introduction of SMMS, the surface transport parameters in the fit also allow one to quantify the resultant changes, if any, in the conductance of the surface.

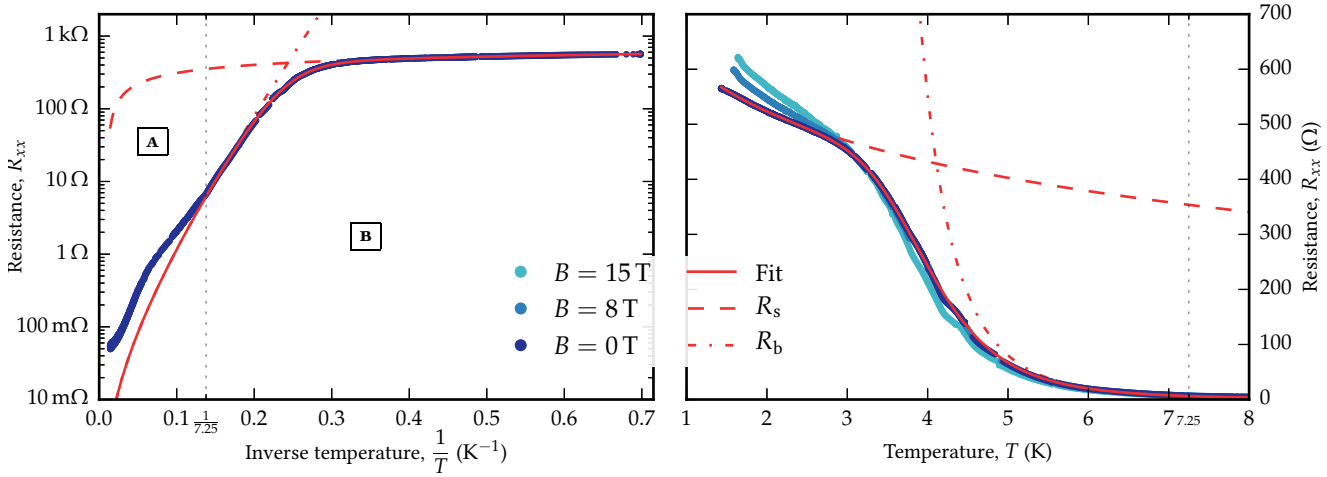

(a) Resistance at $B = 0\,\mathrm{T}$

(b) Resistance at $B = 0\,\mathrm{T}$, $8\,\mathrm{T}$ & $15\,\mathrm{T}$

Figure 6.7: Longitudinal resistance of pristine SmB_6, with current applied along $(1\,0\,0)$. Measured data are overlaid with a two-component parallel resistance fit to the subset of the $B = 0\,\mathrm{T}$ data having $T < 7.25\,\mathrm{K}$, as described in the text. The individual components, R_b and R_s, are also plotted. The fitted parameters are $E_g = 5.50\,\mathrm{meV}$, $C_b = 1.52\,\Omega\mathrm{K}^{\frac{3}{2}}$, $C_s = 132\,\Omega$ and $D_s = 615\,\Omega$.
a: There is a noticeable deviation in the trend at $T \geq 7.25\,\mathrm{K}$ (region A) from the lower temperature behaviour (region B). The fit has been extrapolated into region A to highlight this deviation at 7.25 K;
b: Conductance is clearly dominated by bulk carriers at temperatures above ∼5.5 K and by surface carriers at temperatures below ∼3 K, but shows mixed characteristics in between. The effect of applying magnetic field, **B**, along $(0\,0\,1)$ is also shown.

Fits were performed with a least-squares routine using the Levenberg-Marquardt algorithm, which was seeded with the initial values $C_s = 500\,\Omega$, $D_s = 1\,\Omega$, $E_g = 4\,\text{meV}$ and $C_b = 1\,\Omega\text{K}^{\frac{3}{2}}$. When the fit is performed on the data from all temperatures, it shows a clear deviation from the data for $T > 7.25\,\text{K}$ (this is particularly clear in a plot of $\log R$ versus $\frac{1}{T}$). We do not propose a detailed mechanism for this, though it may be due to the onset of quasiparticle-phonon scattering, undermining our assumption in the fit that the only significant bulk scattering processes are temperature-independent. Another possibility is that the thermal evolution of the Kondo hybridisation gap may result in fluctuations that lead to increased scattering. In the absence of a satisfying explanation for this behaviour, the fits reported here were instead performed only on data from $T < 7.25\,\text{K}$ (see figure 6.7a). Fits were performed on data from several different samples, all yielding very consistent results for the bulk properties. By aggregating the derived parameters from each sample, the bulk resistivity coefficient is found to be $\gamma_b = (70.5 \pm 17.4)\,\mu\Omega\text{m}\,\text{K}^{\frac{3}{2}}$ and the band-gap energy is found to be $E_g = (5.42 \pm 0.26)\,\text{meV}$. This is in good agreement with a recently published value of $E_g = 5.5\,\text{meV}$ deduced from similar transport measurements [138] and sits well inside the range of previously reported values, 5–7 meV [133, 134, 136, 137]. Plotting the fit alongside the individual fitted components R_b and R_s shows a clear suggestion that transport is dominated by bulk carriers at temperatures above $\sim$5.5 K, while surface carrier transport appears to be dominant below $\sim$2.5 K. At intermediate temperatures, $2.5\,\text{K} < T < 5.5\,\text{K}$, the transport appears to be a well-blended mix of surface and bulk contributions. Naturally, since C_s and D_s are sample dependent and subject to the exact positioning of the contacts, these temperatures are very likely to depend strongly on experiment geometry.

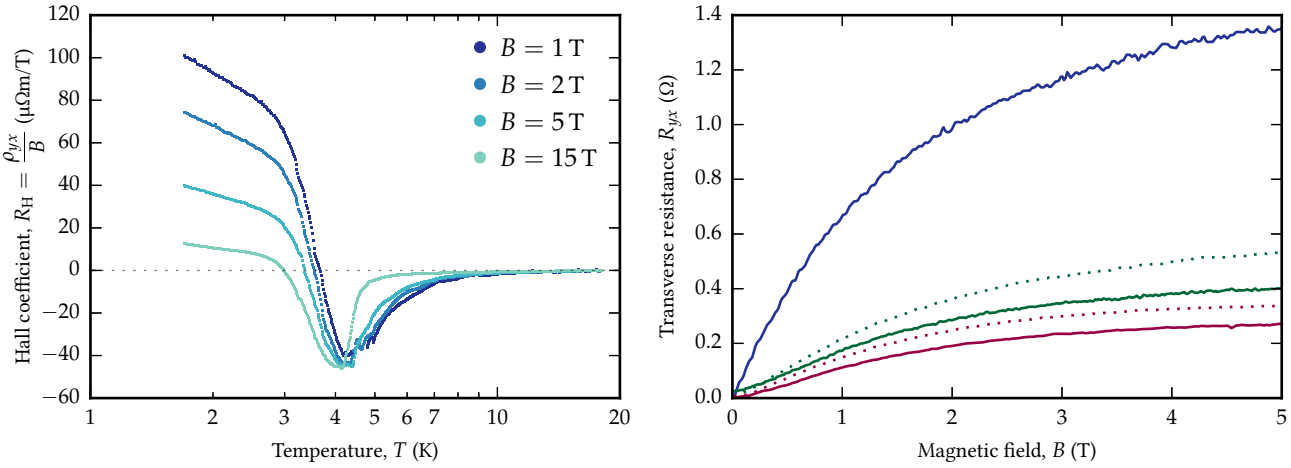

(a) Hall effect in as-grown sample

(b) Transverse resistance of cut samples at 1.4 K

Figure 6.8: Dependence of SmB_6 transverse magnetoresistance on magnetic field, temperature and sample dimensions. Current was applied along $(1\,0\,0)$, transverse voltage measured across $(0\,1\,0)$ and field applied along $(0\,0\,1)$.
a: Temperature and field dependence of Hall coefficient (logarithmic T scale);
b: Transverse magnetoresistance of a long sample (*blue*) and of two shorter samples (*green* and *red*) obtained by cleaving the first sample on a $(1\,0\,0)$ plane. Broken lines show the effect of adding Ga_7Zn (*red*) and Cr_7Zn (*green*) to the daughter samples.

Further indication of the mixed surface and bulk nature of the transport is provided in the longitudinal and transverse magnetoresistance. The temperature dependence of the Hall coefficient, $R_H = \rho_{yx}/B$ (figure 6.8a), shows some features that do not correspond to the behaviour expected of conventional quasiparticle transport. In particular, for conventional electron- and hole-like quasiparticles, it follows from equation 4.11 that in the low-B limit of small $\omega_{ci}\tau_i$,

$$R_H \simeq \frac{1}{B} \cdot \frac{\sum_i \sigma_{0i} \frac{q_i}{e} \omega_{ci} \tau_i}{\sum_i \sigma_{0i}} , \tag{6.19}$$

which is independent of B. In contrast, below 3 K, R_H shows a pronounced suppression with increasing B. We suggest that this is due to the fact that the topologically

protected surface state dominates transverse conductance at these temperatures but is disrupted by the magnetic field, whereby R_H is suppressed.

The hypothesis that unconventional surface carriers dominate the low-temperature transverse conductance in SmB_6 is supported by the unusual dependence of transverse resistance, R_{yx}, on the sample dimensions. Equation 4.12 shows that, under normal circumstances, the transverse resistance, being simply the product of the applied current and the Hall voltage, should depend on the thickness of the sample, l_z, but ought not to depend on its length, l_x. We tested this by comparing R_{yx} measurements from samples with identical l_y and l_z but differing l_x. This was done by measuring the Hall voltage of a long sample, then cleaving it along a $(1\,0\,0)$ plane to form two shorter samples (see figure 6.4) and comparing the Hall voltage measurements from all three. As shown in figure 6.8b, R_{yx} is markedly different for the long and short samples. This can only be due to a predominant contribution to the conductance from a surface state, with convoluted non-local current paths in all directions across the sample surface.

Longitudinal magnetoresistance also shows a clear change in character with temperature, as seen in figures 6.7b and 6.9a. At $T = 1.4\,\mathrm{K}$, magnetoresistance shows a quadratic field dependence at low fields and appears to tend towards a saturation value at higher fields. This is suggestive of closed Fermi surface orbits and indicative of a metallic state (see section 4.2.2). Weak anti-localisation in the low temperature magnetoresistance [187] has been suggested as a key signature of topological insulator behaviour, arising from the spin-orbit interaction that underpins the topological surface state. Although one would expect such behaviour if SmB_6 were a topological insulator, none is seen here. However, as described in section 5.3, previously reported magnetoresistance measurements appear to show

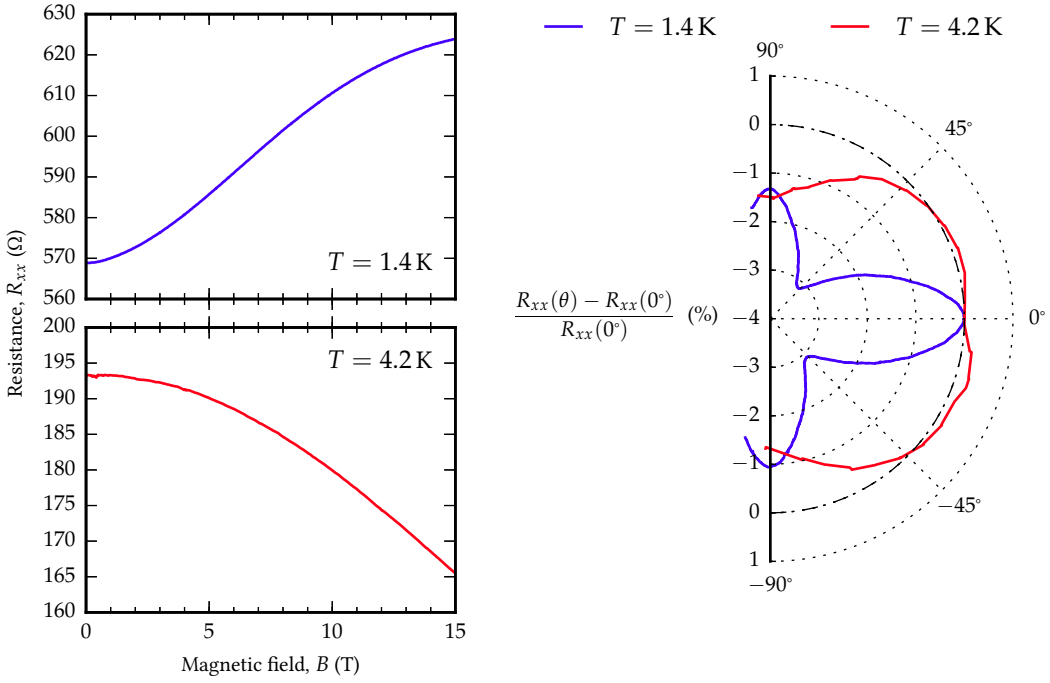

(a) Magnetoresistance at $\theta = 0°$

(b) AMR at $B = 15\,\mathrm{T}$

Figure 6.9: Magnetoresistance of the pristine sample, with applied field **B** rotated in the **b**-**c** plane. θ is the angle between **B** and **c**, as illustrated in figure 6.10.
a: Magnetoresistance at two different temperatures, T, showing a change in character between the surface-carrier-dominated ($T = 1.4\,\mathrm{K}$) and mixed ($T = 4.2\,\mathrm{K}$) regimes;
b: AMR, expressed as a fractional change in the $\theta = 0°$ value.

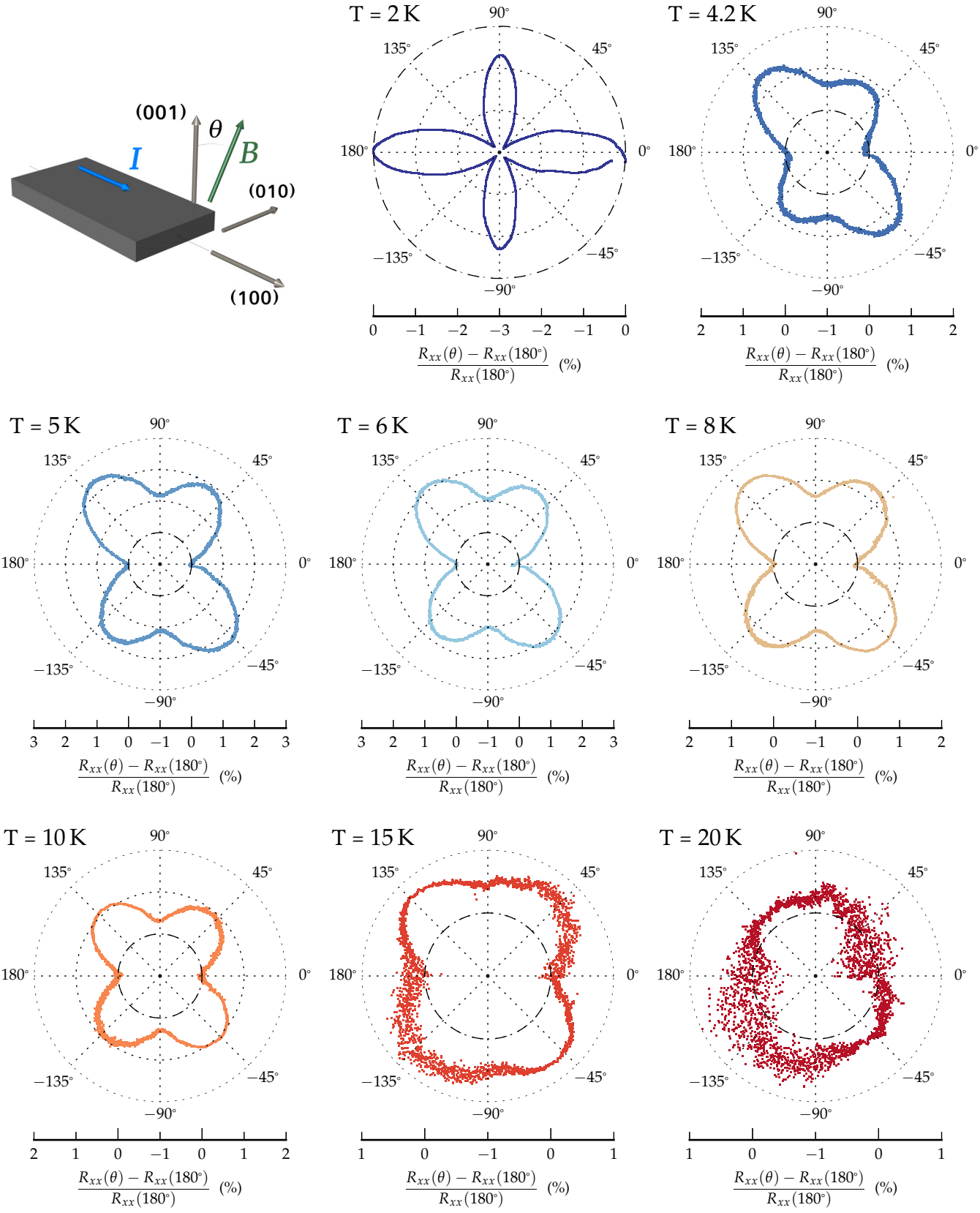

Figure 6.10: AMR in SmB_6 as a function of temperature, T. Radial scales offset below. *Top left:* Current, I, is applied and resistance R_{xx}, measured along the $(1\,0\,0)$ direction. A magnetic field of $B = 15\,\mathrm{T}$ is rotated in the b-c plane, with $\theta = 0°$ corresponding to **B** parallel to $(0\,0\,1)$.

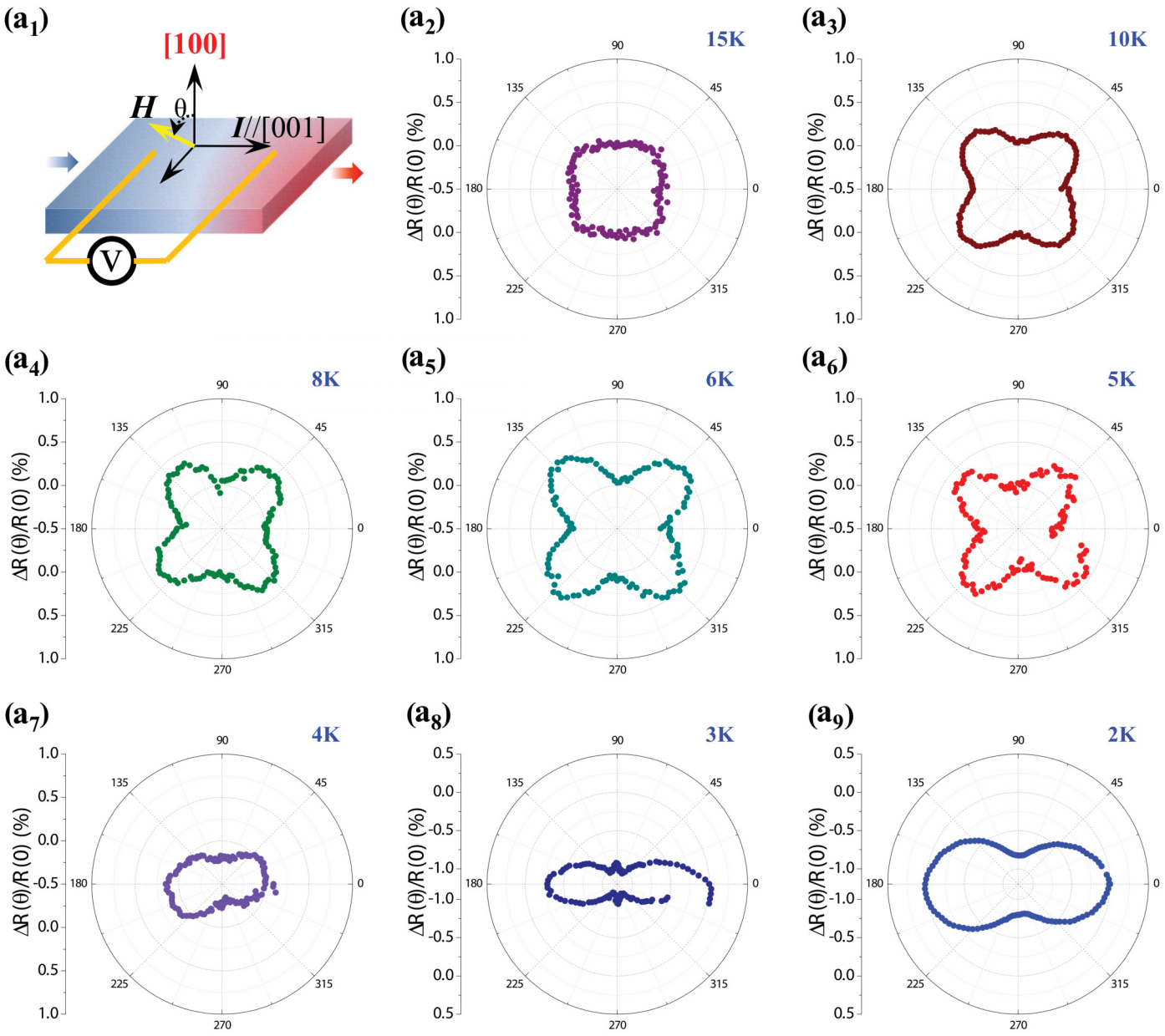

Figure 6.11: AMR in SmB_6 as a function of temperature, T, compare with figure 6.10.
a_1: Sample geometry.
a_2–a_9: AMR measurements, showing qualitatively similar behaviour to our samples, with some key differences. Again, a magnetic field is rotated in the b-c plane, with $\theta = 0°$ corresponding to **B** parallel to $(0\,0\,1)$, but here $B = 9\,\mathrm{T}$. Here, the butterfly pattern is more symmetrical than in our measurements, which may likely be attributed to a better alignment of the axis of rotation with the $(1\,0\,0)$ direction.
Reproduced from [185].

that weak anti-localisation becomes clearly discernible only at temperatures below $\sim$1 K [138]. At 4.2 K, magnetoresistance is less pronounced but is clearly negative, suggesting a different origin for this behaviour, and possibly a mixing of contributions from two different species, such as a Kondo insulating bulk and a metallic surface. It has previously been suggested that the negative character of the magnetoresistance in this temperature range may be due to a narrowing of the bandgap, due to partial suppression of the Kondo hybridisation in a magnetic field [152, 185, 188, 189]. It is notable that the form of the magnetoresistance at 4.2 K is close to that previously reported for other Kondo insulators at low temperature [190].

By rotating the sample around $(1\,0\,0)$ in the magnetic field (effectively rotating **B** in the **b**-**c** plane), some indication of the symmetry of the underlying conducting states may be discerned. Figure 6.9b shows that the AMR at $T = 1.4$ K has a four-lobed pattern, with larger magnetoresistance at $\theta = 0^\circ$ than at $\theta = 90^\circ$, providing two-fold rotational symmetry suggestive of a two-dimensional state. There is no hint in these data of open Fermi surface orbits (see section 4.2.2). Rather, the field dependence of the magnetoresistance was seen to retain the same characteristics, with quadratic dependence at low fields and a suggestion of saturation at high fields, regardless of the orientation θ. Also not observed in these data is any orientation with zero magnetoresistance. Naively, one would expect this to rule out 2-D metallic states, as they ought to display a $\cos^2\theta$ dependence when the field is nearly coplanar with the 2-D Fermi surface. We cannot rule out 2-D surface states so readily however, as the presence of facets at different orientations guarantees that there will always be a surface with a significant surface-normal component of **B**. By comparing with previous AMR studies on thinner platelet samples of SmB_6

[185, 191], we can see that the smaller lobes at $\theta = \pm 90^\circ$ are the AMR contribution from the smaller $(0\,1\,0)$ and $(0\,\bar{1}\,0)$ side faces. In our samples, the side faces are only slightly smaller than the $(0\,0\,1)$ and $(0\,0\,\bar{1})$ top and bottom faces, which appear to contribute the larger lobes at $\theta = 0^\circ$ and $\theta = 180^\circ$. In fact, the AMR contribution from each face of the crystal appears to be a simple two-lobed pattern with much less ambiguous two-fold rotational symmetry. The complicated structure is an inevitable consequence of measuring transport in all faces at once. This illustrates the impossibility of studying the transport properties of a single surface in isolation, since the different facets effectively act as several 2-D samples in different orientations with non-trivial electrical connections.

As the temperature is increased into the regime where bulk and surface transport contributions appear to be mixed, the shape of the AMR changes, adopting a butterfly-shaped four-lobed pattern. This is depicted, evolving with temperature, in figure 6.10. We have not been able to account satisfactorily for this feature, but other recently published studies [185, 191] show similar results (see figure 6.11). It seems that a complicated interplay of surface and bulk quasiparticles may be responsible, each species having its own mechanism of magnetoresistance and its own temperature dependence. Hence examination of the temperature evolution of the AMR (figures 6.10 & 6.12) provides a further qualitative measure of the temperature dependence of the mixing of surface and bulk. This corroborates the conclusions of the fits to R_{xx}, that surface carrier transport dominates the behaviour of SmB_6 at $T = 1.4\,\mathrm{K}$, while the transport properties of surface and bulk are mixed at higher temperatures. Finally, at temperatures as high as 20 K, the surface contribution to the transport becomes practically unmeasurable and there is no significant anisotropy in the magnetoresistance.

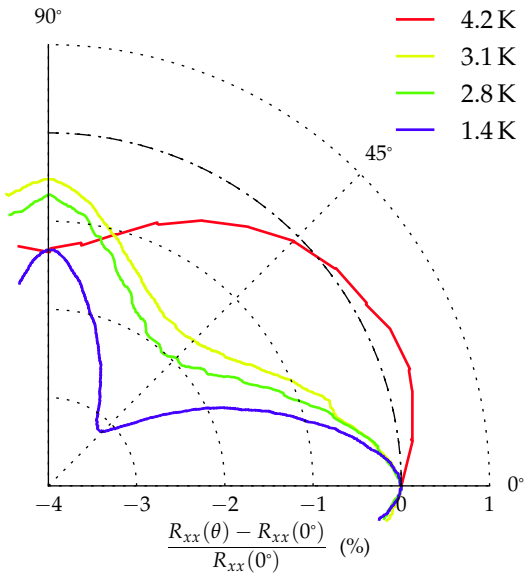

Figure 6.12: Temperature dependence of the first quadrant of AMR of a pristine sample, with experiment geometry as per figure 6.10. Further detail can be seen of the transition from surface-carrier-dominated transport at $T = 1.4\,\mathrm{K}$ to the mixed regime at $T = 4.2\,\mathrm{K}$.

6.4.4 *Effect of surface scatterers*

Having characterised the low-temperature transport properties of unadorned SmB_6 in some detail, we proceeded to coat the $(0\,0\,1)$ surface of each of the measured samples with either Ga_7Zn or Cr_7Zn. We were then able to make directly comparable measurements to determine the effect of the two scatterer molecules. In order better to understand the effect of the coatings, we performed AFM on samples before and after coating with SMMs. Scanned micrographs and indentation data were obtained by Sonia Contera of the Clarendon Laboratory, using an Asylum Research MFP-3D AFM. Scanned images were taken in amplitude modulation mode, using Olympus AC240 silicon cantilevers with a spring constant of $2\,\mathrm{N\,m^{-1}}$. Indentation measurements were performed using Olympus AC160 silicon cantilevers with

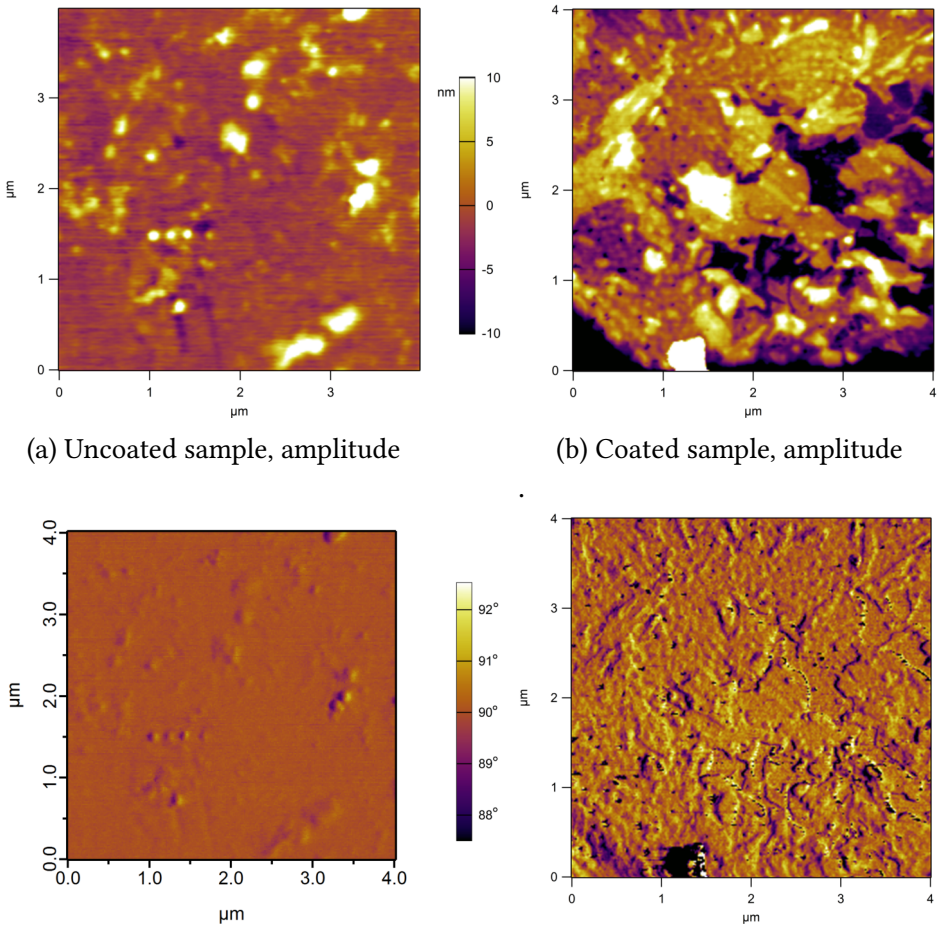

(a) Uncoated sample, amplitude

(b) Coated sample, amplitude

(c) Uncoated sample, phase

(d) Coated sample, phase

Figure 6.13: Atomic force micrographs of SmB_6, with and without a layer of Cr_7Zn.
a & c: Images of bare SmB_6. The amplitude of the cantilever displacement (*a*) shows that the base surface is quite rough, but the phase difference (*c*) between actuation and reflected signal barely deviates from 90° anywhere, indicating that the surface is uniformly hard.
b & d: Images of SmB_6 coated with Cr_7Zn. The displacement amplitude (*b*) shows more extreme features than on the bare sample, indicating that there are regions with widely varying coating thickness. The coating does not appear to be in any way ordered. The phase difference (*d*) between actuation and reflected signal shows significant deviation from 90° across the whole area, implying that the entire surface is coated with the softer, more absorbent SMM.

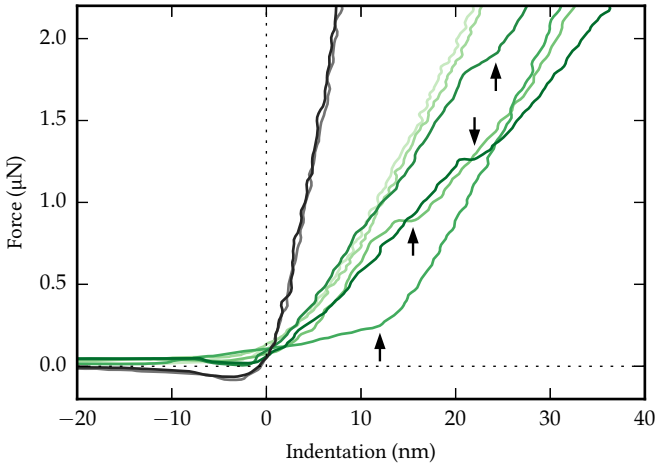

Figure 6.14: AFM indentation on several uncoated and Cr_7Zn-coated regions of SmB_6. The bare surface (*grey lines*) is clearly very hard, and also hydrophilic (attractive force on the cantilever at zero indentation is due to adsorbed water). By contrast, the coated surface (*green lines*) clearly has a lower Young's modulus and is more hydrophobic. Step features (*arrows*) may represent the AFM tip penetrating a layer of Cr_7Zn.

a spring constant of $51.5\,\mathrm{N\,m^{-1}}$, approaching the surface at $2\,\mu\mathrm{m\,s^{-1}}$. The cantilevers were calibrated using the Sader method [192].

As shown in figure 6.13, AFM images of the bare surface show SmB_6 to be very hard, with a somewhat rough surface. By contrast, surfaces coated with Cr_7Zn appear softer and uniformly absorptive of the cantilever actuation energy, indicating that the entire surface is coated. Nevertheless, there is no evidence of long-range structural ordering in the coating material. Indentation data at dozens of sites on uncoated and coated surfaces, a few of which are shown in figure 6.14, reinforce this picture and show additional features that may correspond to penetration of individual layers of Cr_7Zn by the AFM tip.

Since it appears that the SMM molecules are deposited on the sample surface without ordering, the scattering potential of Ga_7Zn is expected to be a purely elec-

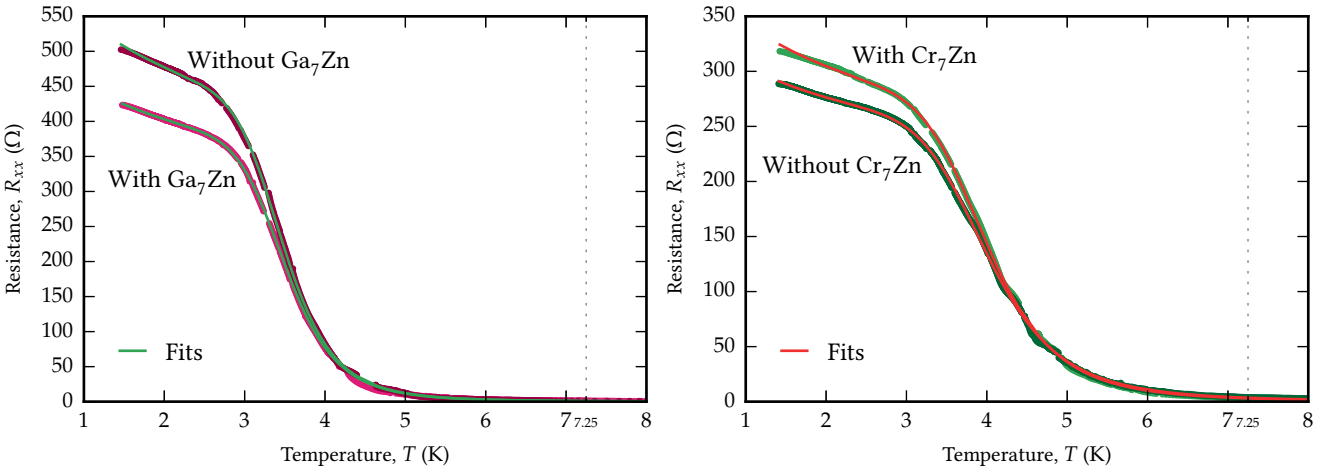

(a) Before and after coating with Ga_7Zn

(b) Before and after coating with Cr_7Zn

Figure 6.15: Temperature dependence of resistance of SmB_6 before and after surface scatterers are deposited on the $(0\,0\,1)$ surface. a: Adding Ga_7Zn, with $S = 0$, causes a drop in surface resistance; b: Cr_7Zn, with $S = \frac{3}{2}$, causes an increase.

trostatic white-noise potential, whereas that of Cr_7Zn will have a similar white-noise distribution with an additional magnetic component. Because the transport data reported here were all taken at temperatures below 8 K, it is safe to assume that the scatterer SMMs will each predominantly be in their magnetic ground state. As such, we expect Ga_7Zn, which has $S = 0$, not to significantly affect the scattering rate of surface quasiparticles, though it may alter the transport properties by the influence of its electrostatic potential on the surface bandstructure. Cr_7Zn, being isoelectronic with Ga_7Zn, is expected to have an identical electrostatic influence on the surface bandstructure but also, due to its having $S = \frac{3}{2}$, to cause an increase in scattering rate in the surface transport.

Figure 6.15 shows the typical longitudinal resistance behaviour observed in a sample before and after coating with Ga_7Zn, and in another before and after coating with Cr_7Zn. A two-component parallel conductance fit has been performed in

each case, just as for the resistance data of the pristine samples, as described in section 6.4.3. For the Ga_7Zn-coated sample (figure 6.15a), the addition of the surface scatterer caused a drop in the surface resistance coefficient C_s, obtained from the fit, yielding a ratio of coated to uncoated values $C_s^{Ga_7Zn}/C_s^{bare} = 0.706 \pm 0.008$. This shows that the electrostatic potential of the SMM coating acts to increase surface conductance. Meanwhile, for the Cr_7Zn-coated sample (figure 6.15b), the addition of the surface scatterer caused an increase in C_s, yielding a ratio $C_s^{Cr_7Zn}/C_s^{bare} = 1.369 \pm 0.018$. If we assume that the electrostatic potential of Cr_7Zn decreases surface resistance by the same factor as does Ga_7Zn, this suggests that the observed net increase in surface resistance is due to the magnetic component of the scattering potential alone. This appears to cause an increase in the low-temperature ($T < 3\,K$) surface carrier scattering rate by a factor of $C_s^{Cr_7Zn}/C_s^{Ga_7Zn} = 1.94 \pm 0.04$.

Measurements of magnetoresistance are shown for two samples, one before and after coating with Ga_7Zn in figure 6.16, and one before and after coating with Cr_7Zn in figure 6.17. They show that the effect of the scatterer coating can be treated as a multiplicative contribution to the behaviour of pristine SmB_6, independent of magnetic field strength and direction. The impact of the surface scatterers on R_{xx} is proportionally slightly larger at $T = 1.4\,K$ than at $T = 4.2\,K$, which probably reflects the fact that surface transport is more dominant at lower temperatures.

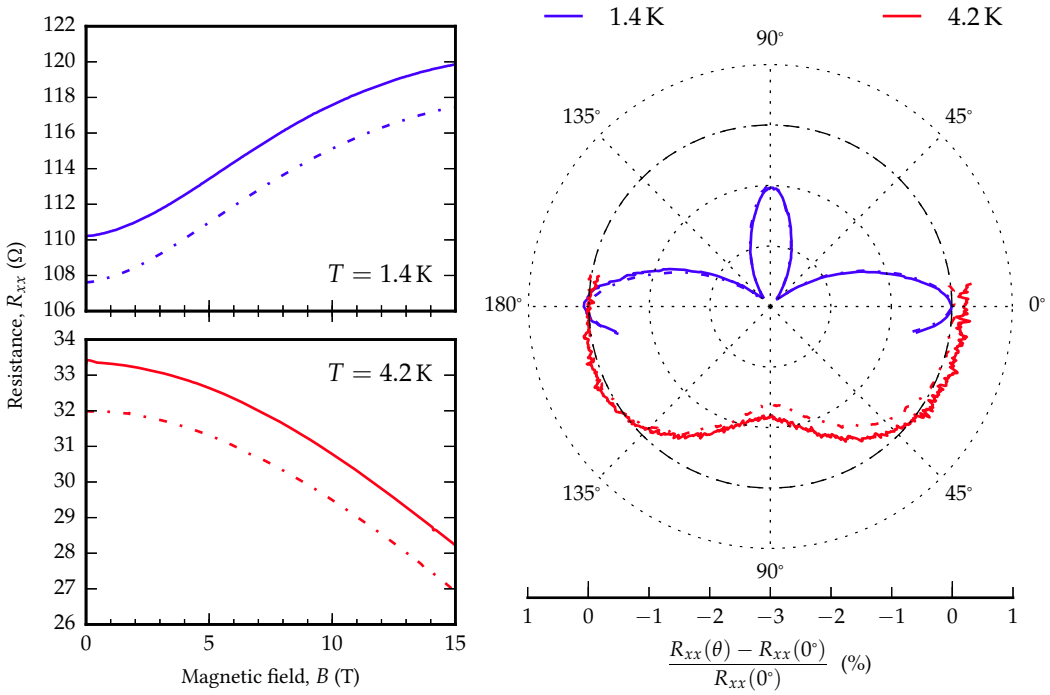

(a) Magnetoresistance at $\theta = 0°$

(b) AMR at $B = 15\,\mathrm{T}$

Figure 6.16: Magnetoresistance of a sample both before (solid lines) and after (broken lines) coating with Ga_7Zn ($S = 0$), with applied field **B** rotated in the **b**-**c** plane. a: Magnetoresistance at two different temperatures, $T = 1.4\,\mathrm{K}$ & $T = 4.2\,\mathrm{K}$; b: AMR, expressed as a fractional change in the $\theta = 0°$ value, as in figure 6.9b. Radial scale offset below.

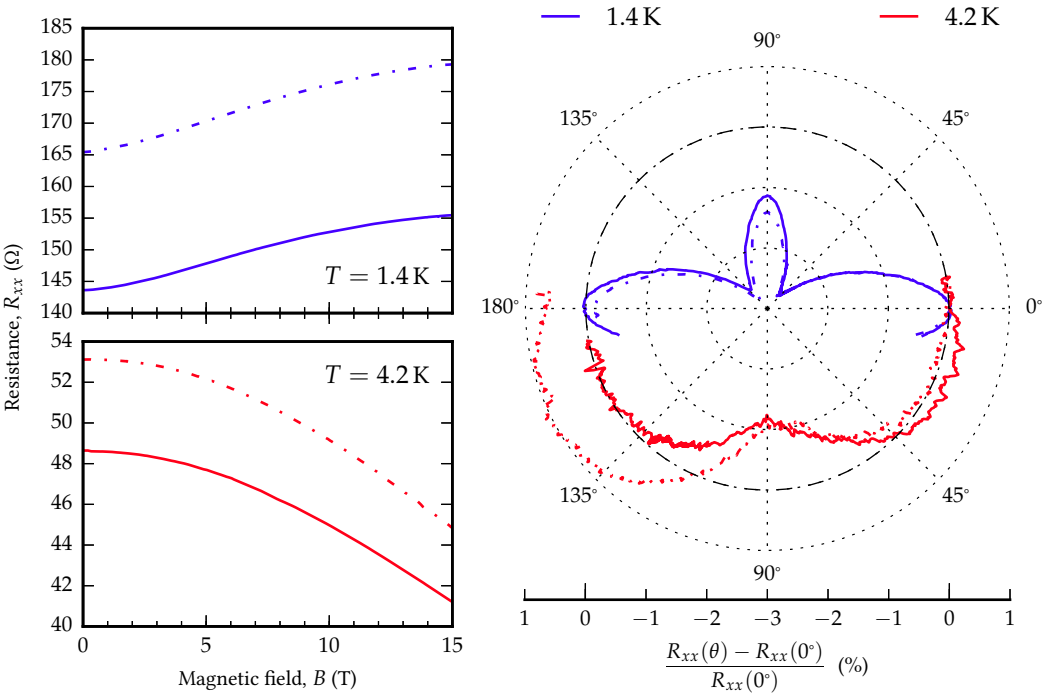

(a) Magnetoresistance at $\theta = 0°$

(b) AMR at $B = 15\,\mathrm{T}$

Figure 6.17: Magnetoresistance of a sample both before (solid lines) and after (broken lines) coating with Cr_7Zn ($S = \frac{3}{2}$), with applied field **B** rotated in the **b**-**c** plane. a: Magnetoresistance at two different temperatures, $T = 1.4\,\mathrm{K}$ & $T = 4.2\,\mathrm{K}$; b: AMR, expressed as a fractional change in the $\theta = 0°$ value, as in figure 6.9b. Radial scale offset below.

6.4.5 *Discussion of results*

In these transport measurements, we have seen many features in SmB_6 that cannot be explained by a conventional bulk conductance model. Our best understanding is that a complicated mixture of surface and bulk effects contribute to the transport properties to differing extents, dependent on temperature and magnetic field. At temperatures below $\sim$7.25 K and at low fields, this mixture appears to be well described by a model of the surface resembling a Kondo metallic state and the bulk as a narrow-bandgap semiconductor. Perhaps the strongest evidence for surface conduction being dominant at low temperatures is that a coating of one face of a sample with a species that is not able to diffuse into the bulk, or affect the bulk bandstructure in any way, nevertheless results in a significant fractional change in the resistance. If both Ga_7Zn and Cr_7Zn caused a decrease in the resistance, and if the molecular system offered a conjugated charge conduction path, it would be possible to ascribe this change to conduction in the deposited layer. The organic ligands shield the metallic core of the molecule from its environment and deny any such conduction path. In fact, what is seen is a marked difference between the effect of a diamagnetic and a paramagnetic surface coating, the latter actually causing an increase in longitudinal resistance. This effect is consistent between samples and is reproducible. It points to the importance of time reversal symmetry in the surface quasiparticle scattering mechanism. Indeed, our data suggest that the magnetic component of the Cr_7Zn scattering potential is responsible for a near doubling of the scattering rate, by comparison with the Ga_7Zn coating.

These data alone cannot determine whether the putative SmB_6 surface state arises from a non-trivial bandstructure topology, but they do lend further weight to that model. At the very least, the importance of time reversal symmetry indicates a surface bandstructure that contains non–Kramers-degenerate states. The debate over whether surface or bulk physics dominates has been particularly difficult to resolve in light of various quantum oscillations studies [148] (see section 5.3.3). On the strength of our results, it seems difficult to rule out a surface state Fermi surface. It seems likely therefore that the reconciliation of the differing schools of thought on SmB_6 should involve a model in which the bulk Kondo gap is established at lower temperatures and magnetic fields, but is suppressed or even closed altogether at higher fields, as it is at higher temperatures. A model along these lines has already been proposed [155] and would account for apparent the dominance of the surface state in our study, while others report data, obtained at much higher magnetic fields, more consistent with a bulk Fermi surface [153].

Another complication, which has been discussed widely in studies of flux-grown samples of SmB_6 [154], is the suggestion that the observed transport effects and quantum oscillations might be attributable to inclusions of aluminium flux in the bulk of some or all such samples [193]. Our results do not rule out the possibility that aluminium contributes to transport in SmB_6. Indeed, the exact level of the low-temperature resistance plateau (see figure 6.7) may be dependent on the amount of co-crystallised flux or lacunae of elemental aluminium. We have not speculated on the nature of the various possible non–Kondo-metal conduction processes implicit in equation 6.17. Aluminium cannot account, however, for the logarithmic temperature dependence of the resistance, suggestive of Kondo-metal-like behaviour. Finally, the most striking feature of our data, that a perturbative coating on

the surface causes such significant changes in the resistance of a sample of SmB_6, with key differences in character between magnetic and non-magnetic coatings, likewise cannot be attributed to residual flux.

6.5 CLOSING COMMENTS AND OUTLOOK

In summary, we have developed a technique for introducing a random surface potential, with and without a magnetic component, to probe the specific sensitivity of a surface state to magnetic scattering. This is, to our knowledge, the first technique that allows one to separate the effects of the electrostatic and magnetic components of a scattering potential. We anticipate this technique to be particularly applicable to studies of topologically non-trivial surface states. Such specialist transport measurements are likely to be essential if topological insulators are to fulfil their promise as the basis of new electronic device technologies. In SmB_6, there is a clear difference between the influence of magnetic and of non-magnetic scatterers, which may be evidence to support the hypothesis that $\mathcal{T}$-invariant scattering processes are suppressed in the surface state because of topological protection. It seems it would be possible to apply this method to any TI materials that are amenable to transport measurements, that have a well-established bulk bandgap and that are robust enough to withstand the moderately high temperatures encountered during deposition of the SMMs. As such, we expect the technique to have quite broad applicability in future studies of strong TIs.

It seems most likely that our measurements at these reasonably low temperatures and magnetic fields corroborate other transport studies in supporting the

topological Kondo insulator model of SmB_6, or some other model in which the surface bandstructure is key. Future studies of this material must therefore reconcile this with the observation at higher fields of high frequency quantum oscillations, which have been attributed to a Fermi surface in the bulk bandstructure. One possible future approach might be to employ a similar SMM deposition technique to explore the robustness of these high-field quantum oscillations to perturbation at the surface. Bulk-origin oscillations ought not to be affected, whereas one might expect surface-origin oscillations to exhibit a shift in frequency due to electrostatic gating altering the extremal Fermi surface area, and a change in amplitude due to magnetic scattering by the SMM. The result of such an experiment would further inform the quest for a complete model of bandstructure and transport in SmB_6, which at present remains elusive.

Part III

CONCLUSION

Lithography is a difficult and ofttimes a very trying occupation, and calls for young men of courage and determination. For this reason therefore, in spite of disappointment and failure, the apprentice must constantly strive to improve on his previous best.

D Cumming on the *Training of Apprentices* [1]

7

SUMMARY AND OUTLOOK

This thesis has outlined the development of two new techniques that exploit very small structures, on the micro- and nano-scale, to enable innovative electrical transport measurements on a variety of materials.

In developing the first technique, we set out to find a way of applying the versatility of electron-beam lithography for patterning sub-micron-scale electronic circuitry to the problem of deriving single crystal samples from a powder. To overcome difficulties associated with the variability of sample morphology and size, we found it convenient to embed samples in a layer of SU-8 photoresist such that the top surfaces of the sample and of the photoresist form a composite substrate. This was found to provide an adequate canvas for electron-beam lithography and permitted us to make patterned contacts on samples as small as about 10 μm. It thereby presents a possible means of making electrical transport measurements on materials of which single crystals have not yet been grown large enough for conventional techniques. The micro-fabricated apparatus was designed to be compatible with high magnetic field measurements at cryogenic temperatures, though this has not yet been fully tested.

By way of exposition, this technique was used to perform a simple resistivity measurement on a crystallite of $Sr_2MnO_2Cu_{1.5}Se_2$, which was approximately 40 μm × 30 μm × 1 μm in size. Though the sample was destroyed during the meas-

urement, an apparent phase transition was observed in the resistivity at 213 K, which may possibly be associated with a structural transition from disorder to short-range order in the copper and copper vacancies within the $Cu_{1.5}Se_2$ layers.

To realise our ambition that this technique might be made applicable to powder samples of a wide range of materials, some further characterisation is still required. It would be desirable to perform basic measurements, of the sort performed on $Sr_2MnO_2Cu_{1.5}Se_2$, on a wider range of samples and at lower temperatures. Further straightforward refinements might include the adoption of more adventurous contact geometries and the investigation of scanning electron microscope energy dispersive x-ray spectroscopy to provide in situ compositional analysis of mounted samples. Also, the performance of these micro-fabricated assemblies has not yet been thoroughly tested in a magnetic field.

The second technique provides a method by which one can determine the sensitivity of surface transport in a topological insulator to a magnetic scattering potential. It exploits some useful properties of two species of molecular nano-magnets derived from $Cr_8F_8(O_2C\,{}^tBu)_{16}$ rings, one with a non-zero spin and the other (not strictly magnetic at all) with zero spin. By characterising the properties of native samples of a topological insulator and then depositing one or other nano-magnet onto the surface, one can determine the increase in scattering rate due to the magnetic scatterers, independently of the gating effect of the associated electrostatic potential. We believe ours is the first technique to realise this distinction in a straightforward measurement.

We applied this technique to the Kondo insulator SmB_6, which has been proposed as a 3-D topological insulator, and were able to demonstrate that a sur-

face conduction channel dominates the low temperature transport. Using atomic force microscopy we were able to determine that our single-molecule magnet layer formed a coating over the whole of the upper sample surface and that the coating was disordered, such that the resultant scattering potential ought to be random. Although the electrostatic influence of the deposited molecules gated the surface state such as to increase the surface conductance, the effect of the magnetic scatterers was to induce a marked decrease in conductance. In a topological insulator, the locking of the quasiparticles' spin to their crystal momentum, guaranteed by the topology of the surface bandstructure, suppresses only time-reversal invariant scattering processes. Scattering from a magnetic potential should therefore not be so suppressed. Consequently, our measurements confirm that SmB_6 shows transport behaviour consistent with its being a topological insulator.

While transport measurements and several spectroscopic studies tend to support the 3-D topological insulator model of SmB_6, certain other investigations instead support an unconventional non-topological picture. Particular division is evident in the interpretation of seemingly contradictory measurements of quantum oscillations. Our results appear to confirm that SmB_6 has a topologically protected surface state at low temperature and relatively low magnetic field. It therefore seems likely that the apparently inconsistent interpretations may arise due to a difference in behaviour at higher magnetic fields, perhaps due to suppression or complete closure of the Kondo gap.

Our method is now sufficiently fully developed that there is, in principle, no obstacle to its employment in the measurement of other topological insulator systems. Investigations of surface transport properties in topological insulators are generally hampered by the fact that relatively few of the 3-D topological insulators

discovered so far actually display good bulk insulating properties. This can mean that the conductivity of the surface state is swamped by that of the bulk. Nevertheless, our technique could be applied to samples of topological insulators such as $Bi_{1-x}Sb_x$, Bi_2Se_3 or Bi_2Te_3, provided they were appropriately doped and/or gated such that the Fermi surface lies within the bulk bandgap, or to other topological insulator materials that may yet be uncovered in future research.

In short, though the development of the two techniques reported here has not been without challenges, both are now poised for application to a wide variety of future electrical transport experiments. They may yet, it is hoped, yield interesting data in fields as diverse as the search for new high-temperature superconductors and the quest to better understand the strange properties of topologically protected conduction.

BIBLIOGRAPHY

[1] D Cumming. *Handbook of lithography*. A & C Black, reissued 2nd (1919) edition, 1932.

[2] R P Feynman. There's plenty of room at the bottom. *Engineering and Science*, 23 (5):22–36, February 1960.

[3] D A Buck and K R Shoulders. An approach to microminiature printed systems. In *Papers and Discussions Presented at the December 3–5, 1958, Eastern Joint Computer Conference: Modern Computers: Objectives, Designs, Applications*, AIEE-ACM-IRE '58 (Eastern), pages 55–59. Association for Computing Machinery, December 1958.

[4] E Ruska. The development of the electron microscope and of electron microscopy. In G Ekspong, editor, *Physics: 1981–1990*, Nobel Lectures Including Presentation Speeches and Laureates' Biographies, pages 355–380. World Scientific, December 1993.

[5] R Hooke. *Micrographia, or, Some physiological descriptions of minute bodies made by magnifying glasses with observations and inquiries thereupon*. Royal Society, 1665.

[6] T E Everhart and T L Hayes. The scanning electron microscope. *Scientific American*, 226(1):54–69, January 1972.

[7] G Owen. Electron lithography for the fabrication of microelectronic devices. *Reports on Progress in Physics*, 48(6):795–851, October 1985.

[8] J I Goldstein, D E Newbury, P Echlin, D C Joy, C E Lyman, E Lifshin, L Sawyer, and J R Michael. *Scanning Electron Microscopy and X-ray Microanalysis*. Springer, 3rd edition, 2003.

[9] D J Stokes. *Principles and Practice of Variable Pressure/Environmental Scanning Electron Microscopy (VP-ESEM)*. Published in association with the Royal Microscopical Society. Wiley, November 2008.

[10] N H Turner. X-ray photoelectron and Auger electron spectroscopy. In *Encyclopedia of Analytical Chemistry*, chapter 2, pages 1–40. Wiley, September 2006.

[11] N Samoto and R Shimizu. Theoretical study of the ultimate resolution in electron beam lithography by Monte Carlo simulation, including secondary electron generation: Energy dissipation profile in polymethylmethacrylate. *Journal of Applied Physics*, 54(7):3855–3859, March 1983.

[12] D F Kyser and N S Viswanathan. Monte Carlo simulation of spatially distributed beams in electron-beam lithography. *Journal of Vacuum Science & Technology*, 12(6):1305–1308, September 1975.

[13] M Hatzakis. Electron resists for microcircuit and mask production. *Journal of the Electrochemical Society*, 116(7):1033–1037, March 1969.

[14] I Zailer, J E F Frost, V Chabasseur-Molyneux, C J B Ford, and M Pepper. Crosslinked PMMA as a high-resolution negative resist for electron beam

lithography and applications for physics of low-dimensional structures. *Semiconductor Science and Technology*, 11(8):1235–1238, April 1996.

[15] MicroChem. Data sheet, *NANO™ PMMA and Copolymer*, 2001.

[16] J G Bednorz and K A Müller. Possible high T_c superconductivity in the Ba–La–Cu–O system. *Zeitschrift für Physik B Condensed Matter*, 64(2):189–193, April 1986.

[17] H Takagi, S Uchida, H Obara, K Kishio, K Kitazawa, K Fueki, and S Tanaka. Magnetic susceptibility of high-T_c superconducting oxides $(La,A)_2CuO_4$ (A = Ba,Sr). *Japanese Journal of Applied Physics*, 26(4A):L434–L436, April 1987.

[18] J G Bednorz and K A Müller. Perovskite-type oxides – the new approach to high-T_c superconductivity. In G Ekspong, editor, *Physics: 1981–1990*, Nobel Lectures Including Presentation Speeches and Laureates' Biographies, pages 424–457. World Scientific, December 1993.

[19] D Johrendt, H Hosono, R D Hoffmann, and R Pöttgen. Structural chemistry of superconducting pnictides and pnictide oxides with layered structures. *Zeitschrift für Kristallographie*, 226(4):435–446, February 2011.

[20] J D Corbett. Synthesis of solid-state materials. In A K Cheetham and P Day, editors, *Solid State Chemistry: Techniques*, volume 1: Techniques, chapter 1. Oxford University Press, 1st (corrected) edition, 1988.

[21] M T Weller. *Inorganic Materials Chemistry*. Oxford Chemistry Primers. Oxford University Press, January 1994.

[22] P C Canfield and Z Fisk. Growth of single crystals from metallic fluxes. *Philosophical Magazine Part B*, 65(6):1117–1123, 1992.

[23] D L Kaiser and L F Schneemeyer. Growth of superconducting single crystals. In D A Cardwell and D S Ginley, editors, *Handbook of Superconducting Materials*, volume 1: Superconductivity, Materials and Processes, chapter B2.4, pages 353–391. CRC Press, June 2002.

[24] C N R Rao, R Nagarajan, and R Vijayaraghaven. Synthesis of cuprate superconductors. *Superconductor Science and Technology*, 6(1):1, October 1993.

[25] H J Scheel and F Licci. Phase diagrams and crystal growth of oxide superconductors. *Thermochimica Acta*, 174:115–130, May 1991.

[26] K H P Kim, J H Choi, C U Jung, P Chowdhury, H S Lee, M S Park, H J Kim, J Y Kim, Z Du, E M Choi, M S Kim, W N Kang, S I Lee, G Y Sung, and J Y Lee. Superconducting properties of well-shaped MgB_2 single crystals. *Physical Review B: Condensed Matter and Materials Physics*, 65(10):100510, February 2002.

[27] P J W Moll, R Puzniak, F Balakirev, K Rogacki, J Karpinski, N D Zhigadlo, and B Batlogg. High magnetic-field scales and critical currents in SmFeAs(O,F) crystals. *Nature Materials*, 9(8):628–633, August 2010.

[28] R Cortes-Gil and S J Clarke. Structure, magnetism, and superconductivity of the layered iron arsenides $Sr_{1-x}Na_xFe_2As_2$. *Chemistry of Materials*, 23(4):1009–1016, January 2011.

[29] B H W S De Jong, R G C Beerkens, P A van Nijnatten, and E Le Bourhis. Glass, 1. Fundamentals, chapter 4.13 Optical properties. In *Ullmann's Encyclopedia of Industrial Chemistry*. Wiley-VCH, October 2011.

[30] H Lorenz, M Despont, N Fahrni, J Brugger, P Vettiger, and P Renaud. High-aspect-ratio, ultrathick, negative-tone near-UV photoresist and its applications for MEMS. *Sensors and Actuators A: Physical*, 64(1):33–39, January 1998. Tenth IEEE International Workshop on Micro Electro Mechanical Systems.

[31] A del Campo and C Greiner. SU-8: a photoresist for high-aspect-ratio and 3D submicron lithography. *Journal of Micromechanics and Microengineering*, 17(6):R81–R95, May 2007.

[32] J Melai, C Salm, R Wolters, and J Schmitz. Qualitative and quantitative characterization of outgassing from SU-8. *Microelectronic Engineering*, 86(4–6):761–764, April–June 2009. Special issue: MNE '08—The 34th International Conference on Micro- and Nano-Engineering (MNE).

[33] MicroChem. Data sheet, *SU-8 2000 Permanent Epoxy Negative Photoresist. Processing guidelines for: SU-8 2025, SU-8 2035, SU-8 2050 and SU-8 2075*.

[34] O P Parida and N Bhat. Characterization of optical properties of SU-8 and fabrication of optical components. In *International Conference on Optics and Photonics (ICOP-2009), $34^{\underline{th}}$ Symposium of the Optical Society of India*. Central Scientific Instruments Organisation, Chandigarh, India 2009.

[35] K H Rasmussen, S S Keller, F Jensen, A M Jorgensen, and O Hansen. SU-8 etching in inductively coupled oxygen plasma. *Microelectronic Engineering*, 112:35–40, December 2013.

[36] B J Klein. Electromigration in thin gold films. *Journal of Physics F: Metal Physics*, 3(4):691, 1973.

[37] S J Clarke, P Adamson, S J C Herkelrath, O J Rutt, D R Parker, M J Pitcher, and C F Smura. Structures, physical properties, and chemistry of layered oxychalcogenides and oxypnictides. *Inorganic Chemistry*, 47(19):8473–8486, May 2008. PMID: 18821814.

[38] P Adamson, J Hadermann, C F Smura, O J Rutt, G Hyett, D G Free, and S J Clarke. Competing magnetic structures and the evolution of copper ion/vacancy ordering with composition in the manganite oxide chalcogenides $Sr_2MnO_2Cu_{1.5}(S_{1-x}Se_x)_2$. *Chemistry of Materials*, 24(14):2802–2816, June 2012.

[39] S Jin, X Chen, J Guo, M Lei, J Lin, J Xi, W Wang, and W Wang. $Sr_2Mn_3Sb_2O_2$ type oxyselenides: Structures, magnetism, and electronic properties of $Sr_2AO_2M_2Se_2$ (A = Co,Mn; M = Cu,Ag). *Inorganic Chemistry*, 51(19):10185–10192, September 2012. PMID: 22967274.

[40] J N Blandy, A M Abakumov, K E Christensen, J Hadermann, P Adamson, S J Cassidy, S Ramos, D G Free, H Cohen, D N Woodruff, A L Thompson, and S J Clarke. Soft chemical control of the crystal and magnetic structure of a layered mixed valent manganite oxide sulfide. *APL Materials*, 3(4):041520, April 2015.

[41] J N Blandy, J C Boskovic, and S J Clarke. Synthesis and magnetic structure of the layered manganese oxide selenide $Sr_2MnO_2Ag_{1.5}Se_2$. *Journal of Solid State Chemistry*, 245:61–66, January 2017.

[42] E H Hall. On a new action of the magnet on electric currents. *American Journal of Mathematics*, 2(3):287–292, September 1879.

[43] N W Ashcroft and N D Mermin. *Solid State Physics*. Holt, Rinehart and Winston, January 1976.

[44] C Kittel. *Introduction to Solid State Physics*. Wiley, 8$^{\underline{\text{th}}}$ edition, November 2004.

[45] S H Simon. *The Oxford Solid State Basics*. Oxford University Press, June 2013.

[46] M V Kartsovnik. High magnetic fields: A tool for studying electronic properties of layered organic metals. *Chemical Reviews*, 104(11):5737–5782, October 2004.

[47] P A Goddard. *Magnetotransport Studies of Layered Metallic Systems*. DPhil thesis, University of Oxford, 2003.

[48] A B Pippard. *Magnetoresistance in Metals*. Number 2 in Cambridge Studies in Low Temperature Physics. Cambridge University Press, January 1989.

[49] R G Chambers. The kinetic formulation of conduction problems. *Proceedings of the Physical Society, Section A*, 65(6):458–459, March 1952.

[50] H Budd. Chamber's solution of the Boltzmann equation. *Physical Review*, 127:4, July 1962.

[51] N Demez, Y Takato, S Fujita, and A Suzuki. Theory of the anisotropic magnetoresistance in copper. *Journal of Physics and Chemistry of Solids*, 71(9):1187–1190, September 2010.

[52] A B Pippard. An experimental determination of the Fermi surface in copper. *Philosophical Transactions of the Royal Society of London A: Mathematical, Physical and Engineering Sciences*, 250(979):325–357, December 1957.

[53] S Blundell. *Magnetism in Condensed Matter*. Oxford Master Series in Physics. Oxford University Press, October 2001.

[54] I M Lifshitz, M I Azbel', and M I Kaganov. The theory of galvanomagnetic effects in metals. *Journal of Experimental and Theoretical Physics*, 4(1):41–54, January 1957.

[55] J R Klauder, W A Reed, G F Brennert, and J E Kunzler. Study of the fine structure in the high-field galvanomagnetic properties and the Fermi surface of copper. *Physical Review*, 141:592–603, January 1966.

[56] M S Nam, S J Blundell, A Ardavan, J A Symington, and J Singleton. Fermi surface shape and angle-dependent magnetoresistance oscillations. *Journal of Physics: Condensed Matter*, 13(10):2271–2279, 2001.

[57] P A Goddard, S J Blundell, J Singleton, R D McDonald, A Ardavan, A Narduzzo, J A Schlueter, A M Kini, and T Sasaki. Angle-dependent magnetoresistance of the layered organic superconductor κ-$(ET)_2Cu(NCS)_2$: Simulation and experiment. *Physical Review B: Condensed Matter and Materials Physics*, 69:174509, May 2004.

[58] D Shoenberg. *Magnetic Oscillations in Metals*. Cambridge Monographs on Physics. Cambridge University Press, September 1984.

[59] K von Klitzing, G Dorda, and M Pepper. New method for high-accuracy determination of the fine-structure constant based on quantized Hall resistance. *Physical Review Letters*, 45:494–497, August 1980.

[60] P W Anderson. *Basic Notions of Condensed Matter Physics*. Westview Press, 1st (revised) edition, November 1997.

[61] J E Avron, D Osadchy, and R Seiler. A topological look at the quantum Hall effect. *Physics Today*, 56(8):38–42, August 2003.

[62] J Bellissard, A van Elst, and H Schulz-Baldes. The noncommutative geometry of the quantum Hall effect. *Journal of Mathematical Physics*, 35(10):5373–5451, October 1994.

[63] D J Thouless, M Kohmoto, M P Nightingale, and M den Nijs. Quantized Hall conductance in a two-dimensional periodic potential. *Physical Review Letters*, 49:405–408, August 1982.

[64] R B Laughlin. Quantized Hall conductivity in two dimensions. *Physical Review B: Condensed Matter and Materials Physics*, 23(10):5632–5633, May 1981.

[65] R B Laughlin. Fractional quantization. In G Ekspong, editor, *Physics: 1996–2000*, Nobel Lectures Including Presentation Speeches and Laureates' Biographies, pages 264–286. World Scientific, December 2003.

[66] Q Niu, D J Thouless, and Y S Wu. Quantized Hall conductance as a topological invariant. *Physical Review B: Condensed Matter and Materials Physics*, 31(6):3372–3377, March 1985.

[67] R Kubo. Statistical-mechanical theory of irreversible processes. I. General theory and simple applications to magnetic and conduction problems. *Journal of the Physical Society of Japan*, 12(6):570–586, June 1957.

[68] E Kreyszig. *Differential Geometry*. Number 11 in Mathematical Expositions. University of Toronto Press, 1959.

[69] M V Berry. Quantal phase factors accompanying adiabatic changes. *Proceedings of the Royal Society A: Mathematical, Physical and Engineering Sciences*, 392(1802):45–57, March 1984.

[70] F Wilczek and A Shapere. *Geometric Phases in Physics*. Advanced Series in Mathematical Physics. World Scientific, July 1989.

[71] J Anandan. The geometric phase. *Nature*, 360(6402):307–313, November 1992.

[72] B Simon. Holonomy, the quantum adiabatic theorem, and Berry's phase. *Physical Review Letters*, 51:2167–2170, December 1983.

[73] B I Halperin. Quantized Hall conductance, current-carrying edge states, and the existence of extended states in a two-dimensional disordered potential. *Physical Review B: Condensed Matter and Materials Physics*, 25(4):2185–2190, February 1982.

[74] M Z Hasan and C L Kane. *Colloquium*: Topological insulators. *Reviews of Modern Physics*, 82:3045–3067, November 2010.

[75] C L Kane and E J Mele. Z_2 topological order and the quantum spin Hall effect. *Physical Review Letters*, 95:146802, September 2005.

[76] X L Qi and S C Zhang. Topological insulators and superconductors. *Reviews of Modern Physics*, 83(4):1057–1110, October 2011.

[77] X L Qi, T L Hughes, and S C Zhang. Topological field theory of time-reversal invariant insulators. *Physical Review B: Condensed Matter and Materials Physics*, 78:195424, November 2008.

[78] Y Ando. Topological insulator materials. *Journal of the Physical Society of Japan*, 82(10):102001, September 2013.

[79] A Y Kitaev. Fault-tolerant quantum computation by anyons. *Annals of Physics*, 303(1):2–30, January 2003.

[80] L Fu and C L Kane. Superconducting proximity effect and Majorana fermions at the surface of a topological insulator. *Physical Review Letters*, 100:096407, March 2008.

[81] P J Leek, J M Fink, A Blais, R Bianchetti, M Goppl, J M Gambetta, D I Schuster, L Frunzio, R J Schoelkopf, and A Wallraff. Observation of Berry's phase in a solid-state qubit. *Science*, 318(5858):1889–1892, December 2007.

[82] C L Kane and E J Mele. Quantum spin Hall effect in graphene. *Physical Review Letters*, 95:226801, November 2005.

[83] B A Bernevig and S C Zhang. Quantum spin Hall effect. *Physical Review Letters*, 96:106802, March 2006.

[84] B A Bernevig, T L Hughes, and S C Zhang. Quantum spin Hall effect and topological phase transition in HgTe quantum wells. *Science*, 314(5806):1757–1761, December 2006.

[85] M König, S Wiedmann, C Brüne, A Roth, H Buhmann, L W Molenkamp, X L Qi, and S C Zhang. Quantum spin Hall insulator state in HgTe quantum wells. *Science*, 318(5851):766–770, November 2007.

[86] M König, H Buhmann, L W. Molenkamp, T Hughes, C X Liu, X L Qi, and S C Zhang. The quantum spin Hall effect: Theory and experiment. *Journal of the Physical Society of Japan*, 77(3):031007, March 2008.

[87] L Fu, C L Kane, and E J Mele. Topological insulators in three dimensions. *Physical Review Letters*, 98:106803, March 2007.

[88] S Hüfner. *Photoelectron Spectroscopy: Principles and Applications*. Number 82 in Springer Series in Solid-State Sciences. Springer, 3rd edition, April 2003.

[89] S Suga and A Sekiyama. *Photoelectron Spectroscopy*. Number 176 in Springer Series in Optical Sciences. Springer-Verlag, 1st edition, September 2013.

[90] R M Feenstra. Scanning tunneling spectroscopy. *Surface Science*, 299–300:965–979, January 1994.

[91] R Wiesendanger. *Scanning probe microscopy and spectroscopy: methods and applications*. Cambridge University Press, September 1994.

[92] L Petersen, P T Sprunger, P Hofmann, E Lægsgaard, B G Briner, M Doering, H P Rust, A M Bradshaw, F Besenbacher, and E W Plummer. Direct imaging of the two-dimensional Fermi contour: Fourier-transform STM. *Physical Review B: Condensed Matter and Materials Physics*, 57(12):R6858–R6861, March 1998.

[93] A Nishide, A A Taskin, Y Takeichi, T Okuda, A Kakizaki, T Hirahara, K Nakatsuji, F Komori, Y Ando, and I Matsuda. Direct mapping of the spin-filtered surface bands of a three-dimensional quantum spin Hall insulator. *Physical Review B: Condensed Matter and Materials Physics*, 81:041309, January 2010.

[94] Y Xia, D Qian, D Hsieh, L Wray, A Pal, H Lin, A Bansil, D Grauer, Y S Hor, R J Cava, and M Z Hasan. Observation of a large-gap topological-insulator class with a single Dirac cone on the surface. *Nature Physics*, 5(6):398–402, May 2009.

[95] J G Analytis, J H Chu, Y Chen, F Corredor, R D McDonald, Z X Shen, and I R Fisher. Bulk Fermi surface coexistence with Dirac surface state in Bi_2Se_3: A comparison of photoemission and Shubnikov-de Haas measurements. *Physical Review B: Condensed Matter and Materials Physics*, 81(20):205407, May 2010.

[96] Y L Chen, J H Chu, J G Analytis, Z K Liu, K Igarashi, H H Kuo, X L Qi, S K Mo, R G Moore, D H Lu, M Hashimoto, T Sasagawa, S C Zhang, I R Fisher, Z Hussain, and Z X Shen. Massive Dirac fermion on the surface of a magnetically doped topological insulator. *Science*, 329(5992):659–662, August 2010.

[97] H Beidenkopf, P Roushan, J Seo, L Gorman, I Drozdov, Y S Hor, R J Cava, and A Yazdani. Spatial fluctuations of helical Dirac fermions on the surface of topological insulators. *Nature Physics*, 7(12):939–943, December 2011.

[98] T Valla, Z H Pan, D Gardner, Y S Lee, and S Chu. Photoemission spectroscopy of magnetic and nonmagnetic impurities on the surface of the Bi_2Se_3 topological insulator. *Physical Review Letters*, 108:117601, March 2012.

[99] J Honolka, A A Khajetoorians, V Sessi, T O Wehling, S Stepanow, J L Mi, B B Iversen, T Schlenk, J Wiebe, N B Brookes, A I Lichtenstein, P Hofmann, K Kern, and R Wiesendanger. In-plane magnetic anisotropy of Fe atoms on $Bi_2Se_3(1\,1\,1)$. *Physical Review Letters*, 108:256811, June 2012.

[100] M R Scholz, J Sánchez-Barriga, D Marchenko, A Varykhalov, A Volykhov, L V Yashina, and O Rader. Tolerance of topological surface states towards magnetic moments: Fe on Bi_2Se_3. *Physical Review Letters*, 108:256810, June 2012.

[101] S Y Xu, M Neupane, C Liu, D Zhang, A Richardella, L Andrew Wray, N Alidoust, M Leandersson, T Balasubramanian, J Sánchez-Barriga, O Rader, G Landolt, B Slomski, J Hugo Dil, J Osterwalder, T R Chang, H T Jeng, H Lin, A Bansil, N Samarth, and M Zahid Hasan. Hedgehog spin texture and Berry's phase tuning in a magnetic topological insulator. *Nature Physics*, 8(8):616–622, August 2012.

[102] J Sánchez-Barriga, A Varykhalov, G Springholz, H Steiner, R Kirchschlager, G Bauer, O Caha, E Schierle, E Weschke, A A Ünal, S Valencia, M Dunst, J Braun, H Ebert, J Minár, E Golias, L V Yashina, A Ney, V Holý, and O Rader. Nonmagnetic band gap at the Dirac point of the magnetic topological insulator $(Bi_{1-x}Mn_x)_2Se_3$. *Nature Communications*, 7:10559, February 2016.

[103] H Zhang, C X Liu, X L Qi, X Dai, Z Fang, and S C Zhang. Topological insulators in Bi_2Se_3, Bi_2Te_3 and Sb_2Te_3 with a single Dirac cone on the surface. *Nature Physics*, 5(6):438–442, May 2009.

[104] Y L Chen, J G Analytis, J H Chu, Z K Liu, S K Mo, X L Qi, H J Zhang, D H Lu, X Dai, Z Fang, S C Zhang, I R Fisher, Z Hussain, and Z X Shen. Experimental realization of a three-dimensional topological insulator, Bi_2Te_3. *Science*, 325(5937):178–181, July 2009.

[105] D Hsieh, Y Xia, D Qian, L Wray, F Meier, J H Dil, J Osterwalder, L Patthey, A V Fedorov, H Lin, A Bansil, D Grauer, Y S Hor, R J Cava, and M Z Hasan. Observation of time-reversal-protected single-Dirac-cone topological-insulator states in Bi_2Te_3 and Sb_2Te_3. *Physical Review Letters*, 103:146401, September 2009.

[106] T Zhang, P Cheng, X Chen, J F Jia, X Ma, K He, L Wang, H Zhang, X Dai, Z Fang, X Xie, and Q K Xue. Experimental demonstration of topological surface states protected by time-reversal symmetry. *Physical Review Letters*, 103:266803, December 2009.

[107] X Zhang, N P Butch, P Syers, S Ziemak, R L Greene, and J Paglione. Hybridization, inter-ion correlation, and surface states in the Kondo insulator SmB_6. *Physical Review X*, 3:011011, February 2013.

[108] N Xu, X Shi, P K Biswas, C E Matt, R S Dhaka, Y Huang, N C Plumb, M Radović, J H Dil, E Pomjakushina, K Conder, A Amato, Z Salman, D M Paul, J Mesot, H Ding, and M Shi. Surface and bulk electronic structure of the strongly correlated system SmB_6 and implications for a topological Kondo insulator. *Physical Review B: Condensed Matter and Materials Physics*, 88:121102, September 2013.

[109] Z H Zhu, A Nicolaou, G Levy, N P Butch, P Syers, X F Wang, J Paglione, G A Sawatzky, I S Elfimov, and A Damascelli. Polarity-driven surface metallicity in SmB_6. *Physical Review Letters*, 111:216402, November 2013.

[110] J Jiang, S Li, T Zhang, Z Sun, F Chen, Z R Ye, M Xu, Q Q Ge, S Y Tan, X H Niu, M Xia, B P Xie, Y F Li, X H Chen, H H Wen, and D L Feng. Observation of possible topological in-gap surface states in the Kondo insulator SmB_6 by photoemission. *Nature Communications*, 4:3010, December 2013.

[111] M Neupane, N Alidoust, S Y Xu, T Kondo, Y Ishida, D J Kim, C Liu, I Belopolski, Y J Jo, T R Chang, H T Jeng, T Durakiewicz, L Balicas, H Lin, A Bansil, S Shin, Z Fisk, and M Z Hasan. Surface electronic structure of the topological Kondo-insulator candidate correlated electron system SmB_6. *Nature Communications*, 4:2991, December 2013.

[112] N Xu, P K Biswas, J H Dil, R S Dhaka, G Landolt, S Muff, C E Matt, X Shi, N C Plumb, M Radović, E Pomjakushina, K Conder, A Amato, S V Borisenko, R Yu, H M Weng, Z Fang, X Dai, J Mesot, H Ding, and M Shi. Direct observation of the spin texture in SmB_6 as evidence of the topological Kondo insulator. *Nature Communications*, 5:4566, July 2014.

[113] L Fu and C L Kane. Topological insulators with inversion symmetry. *Physical Review B: Condensed Matter and Materials Physics*, 76:045302, July 2007.

[114] D Hsieh, D Qian, L Wray, Y Xia, Y S Hor, R J Cava, and M Z Hasan. A topological Dirac insulator in a quantum spin Hall phase. *Nature*, 452(7190):970–974, April 2008.

[115] D Hsieh, Y Xia, L Wray, D Qian, A Pal, J H Dil, J Osterwalder, F Meier, G Bihlmayer, C L Kane, Y S Hor, R J Cava, and M Z Hasan. Observation of unconventional quantum spin textures in topological insulators. *Science*, 323(5916):919–922, February 2009.

[116] P Roushan, J Seo, C V Parker, Y S Hor, D Hsieh, D Qian, A Richardella, M Z Hasan, R J Cava, and A Yazdani. Topological surface states protected from backscattering by chiral spin texture. *Nature*, 460(7259):1106–1109, August 2009.

[117] B Lenoir, M Cassart, J P Michenaud, H Scherrer, and S Scherrer. Transport properties of Bi-rich Bi-Sb alloys. *Journal of Physics and Chemistry of Solids*, 57(1):89–99, January 1996.

[118] Y A Bychkov and E I Rashba. Properties of a 2D electron gas with lifted spectral degeneracy. *JETP Letters*, 39(2):78–81, January 1984.

[119] J G Checkelsky, Y S Hor, M H Liu, D X Qu, R J Cava, and N P Ong. Quantum interference in macroscopic crystals of nonmetallic Bi_2Se_3. *Physical Review Letters*, 103:246601, December 2009.

[120] J G Analytis, R D McDonald, S C Riggs, J H Chu, G S Boebinger, and I R Fisher. Two-dimensional surface state in the quantum limit of a topological insulator. *Nature Physics*, 6(12):960–964, December 2010.

[121] D X Qu, Y S Hor, J Xiong, R J Cava, and N P Ong. Quantum oscillations and Hall anomaly of surface states in the topological insulator Bi_2Te_3. *Science*, 329(5993):821–824, August 2010.

[122] T Mori. Lanthanides: Boride, carbide, and nitride compounds. In *Encyclopedia of Inorganic and Bioinorganic Chemistry*. John Wiley & Sons, 2011.

[123] S Ramankutty, N de Jong, Y K Huang, B Zwartsenberg, F Massee, T V Bay, M S Golden, and E Frantzeskakis. Comparative study of rare earth hexaborides using high resolution angle-resolved photoemission. *Journal of Electron Spectroscopy and Related Phenomena*, 208:43–50, April 2016. Special Issue: Electronic structure and function from state-of-the-art spectroscopy and theory.

[124] V A Trounov, A L Malyshev, D Y Chernyshov, M M Korsukova, V N Gurin, L A Aslanov, and V V Chernyshev. Temperature dependences of the parameters of atoms in the crystal structure of the intermediate-valence semiconductor SmB_6: investigation by high-resolution powder neutron diffraction. *Journal of Physics: Condensed Matter*, 5(16):2479–2488, 1993.

[125] J Etourneau and P Hagenmuller. Structure and physical features of the rare-earth borides. *Philosophical Magazine Part B*, 52(3):589–610, March 1985.

[126] S Kimura, T Nanba, M Tomikawa, S Kunii, and T Kasuya. Electronic structure of rare-earth hexaborides. *Physical Review B: Condensed Matter and Materials Physics*, 46:12196–12204, November 1992.

[127] C M Varma. Mixed-valence compounds. *Reviews of Modern Physics*, 48:219–238, April 1976.

[128] J C Nickerson, R M White, K N Lee, R Bachmann, T H Geballe, and G W Hull. Physical properties of SmB_6. *Physical Review B: Condensed Matter and Materials Physics*, 3:2030–2042, March 1971.

[129] B A Jones. The Kondo effect. In H Kronmuller and S Parkin, editors, *Handbook of Magnetism and Advanced Magnetic Materials*, volume 1: Fundamentals and Theory, chapter 6. Wiley, December 2007.

[130] P Coleman. Heavy fermions: Electrons at the edge of magnetism. In H Kronmuller and S Parkin, editors, *Handbook of Magnetism and Advanced Magnetic Materials*, volume 1: Fundamentals and Theory, chapter 5. Wiley, December 2007.

[131] G Aeppli and Z Fisk. Kondo insulators. In *Comments on Condensed Matter Physics*, volume 16 of *Comments on Modern Physics, part B*. Gordon & Breach, 1992.

[132] A Menth, E Buehler, H J Levinstein, and T H Geballe. Configuration of Sm in SmB_6. *Journal of Applied Physics*, 40(3):1006, March 1969.

[133] A Menth, E Buehler, and T H Geballe. Magnetic and semiconducting properties of SmB_6. *Physical Review Letters*, 22:295–297, February 1969.

[134] J W Allen, B Batlogg, and P Wachter. Large low-temperature Hall effect and resistivity in mixed-valent SmB_6. *Physical Review B: Condensed Matter and Materials Physics*, 20(12):4807–4813, December 1979.

[135] M Dzero, J Xia, V Galitski, and P Coleman. Topological Kondo insulators. *Annual Review of Condensed Matter Physics*, 7(1):249–280, March 2016.

[136] J C Cooley, M C Aronson, Z Fisk, and P C Canfield. SmB_6: Kondo insulator or exotic metal? *Physical Review Letters*, 74:1629–1632, February 1995.

[137] S Wolgast, Ç Kurdak, K Sun, J W Allen, D J Kim, and Z Fisk. Low-temperature surface conduction in the Kondo insulator SmB_6. *Physical Review B: Condensed Matter and Materials Physics*, 88:180405, November 2013.

[138] S Biswas, R Nagarajan, S Sarkar, K R Amin, M Ciomaga Hatnean, S Tewari, G Balakrishnan, and A Bid. Robust local and nonlocal transport in the topological Kondo insulator SmB_6 in the presence of a high magnetic field. *Physical Review B: Condensed Matter and Materials Physics*, 92:085103, August 2015.

[139] G Travaglini and P Wachter. Intermediate-valent SmB_6 and the hybridization model: An optical study. *Physical Review B: Condensed Matter and Materials Physics*, 29:893–898, January 1984.

[140] I Frankowski and P Wachter. Point-contact spectroscopy on SmB_6, TmSe, LaB_6 and LaSe. *Solid State Communications*, 41(8):577–580, February 1982.

[141] S Rößler, T H Jang, D J Kim, L H Tjeng, Z Fisk, F Steglich, and S Wirth. Hybridization gap and Fano resonance in SmB_6. *Proceedings of the National Academy of Sciences*, 111(13):4798–4802, April 2014.

[142] J W Allen, R M Martin, B Batlogg, and P Wachter. Mixed valent SmB_6 and gold-SmS: Metals or insulators? *Journal of Applied Physics*, 49(3):2078–2083, March 1978.

[143] M Dzero, K Sun, V Galitski, and P Coleman. Topological Kondo insulators. *Physical Review Letters*, 104:106408, March 2010.

[144] M Dzero, K Sun, P Coleman, and V Galitski. Theory of topological Kondo insulators. *Physical Review B: Condensed Matter and Materials Physics*, 85:045130, January 2012.

[145] T Takimoto. SmB_6: A promising candidate for a topological insulator. *Journal of the Physical Society of Japan*, 80(12):123710, November 2011.

[146] F Lu, J Zhao, H Weng, Z Fang, and X Dai. Correlated topological insulators with mixed valence. *Physical Review Letters*, 110:096401, February 2013.

[147] D J Kim, S Thomas, T Grant, J Botimer, Z Fisk, and J Xia. Surface Hall effect and nonlocal transport in SmB_6: Evidence for surface conduction. *Scientific Reports*, 3:3150, November 2013.

[148] P Coleman. The mystery of SmB_6: Topological or strange insulator? Journal Club for Condensed Matter Physics, www.condmatjclub.org/?p=2970, January 2017.

[149] M M Yee, Y He, A Soumyanarayanan, D J Kim, Z Fisk, and J E Hoffman. Imaging the Kondo insulating gap on SmB_6. ArXiv pre-print retrieved 29-05-17, August 2013.

[150] W Ruan, C Ye, M Guo, F Chen, X Chen, G M Zhang, and Y Wang. Emergence of a coherent in-gap state in the SmB_6 Kondo insulator revealed by scanning tunneling spectroscopy. *Physical Review Letters*, 112:136401, March 2014.

[151] T Ando, T Nakanishi, and R Saito. Berry's phase and absence of back scattering in carbon nanotubes. *Journal of the Physical Society of Japan*, 67(8):2857–2862, August 1998.

[152] A Lacerda, D Rickel, M Hundley, P Canfield, J Thompson, Z Fisk, P Haen, and F Lapierre. High field magnetoresistance in SmB_6. *Physica B: Condensed Matter*, 199–200:469–470, April 1994.

[153] B S Tan, Y T Hsu, B Zeng, M C Hatnean, N Harrison, Z Zhu, M Hartstein, M Kiourlappou, A Srivastava, M D Johannes, T P Murphy, J H Park, L Balicas, G G Lonzarich, G Balakrishnan, and S E Sebastian. Unconventional Fermi surface in an insulating state. *Science*, 349(6245):287–290, July 2015.

[154] G Li, Z Xiang, F Yu, T Asaba, B Lawson, P Cai, C Tinsman, A Berkley, S Wolgast, Y S Eo, D J Kim, Ç Kurdak, J W Allen, K Sun, X H Chen, Y Y Wang, Z Fisk, and L Li. Two-dimensional Fermi surfaces in Kondo insulator SmB_6. *Science*, 346(6214):1208–1212, December 2014.

[155] J Knolle and N R Cooper. Quantum oscillations without a Fermi surface and the anomalous de Haas–van Alphen effect. *Physical Review Letters*, 115:146401, September 2015.

[156] J D Denlinger, S Jang, G Li, L Chen, B J Lawson, T Asaba, C Tinsman, F Yu, K Sun, J W Allen, Ç Kurdak, D J Kim, Z Fisk, and L Li. Consistency of photoemission and quantum oscillations for surface states of SmB_6. ArXiv pre-print retrieved 13-03-17, January 2016.

[157] N Wakeham, P F S Rosa, Y Q Wang, M Kang, Z Fisk, F Ronning, and J D Thompson. Low-temperature conducting state in two candidate topological Kondo insulators: SmB_6 and $Ce_3Bi_4Pt_3$. *Physical Review B: Condensed Matter and Materials Physics*, 94:035127, July 2016.

[158] N J Laurita, C M Morris, S M Koohpayeh, P F S Rosa, W A Phelan, Z Fisk, T M McQueen, and N P Armitage. Anomalous three-dimensional bulk AC conduction within the Kondo gap of SmB_6 single crystals. *Physical Review B: Condensed Matter and Materials Physics*, 94:165154, October 2016.

[159] P K Biswas, M Legner, G Balakrishnan, M C Hatnean, M R Lees, D M Paul, E Pomjakushina, T Prokscha, A Suter, T Neupert, and Z Salman. Suppression of magnetic excitations near the surface of the topological Kondo insulator SmB_6. *Physical Review B: Condensed Matter and Materials Physics*, 95:020410, January 2017.

[160] T Tanaka, R Nishitani, C Oshima, E Bannai, and S Kawai. The preparation and properties of CeB_6, SmB_6, and GdB_6. *Journal of Applied Physics*, 51(7):3877–3883, July 1980.

[161] Y S Hor, P Roushan, H Beidenkopf, J Seo, D Qu, J G Checkelsky, L A Wray, D Hsieh, Y Xia, S Y Xu, D Qian, M Z Hasan, N P Ong, A Yazdani, and R J Cava. Development of ferromagnetism in the doped topological insulator $Bi_{2-x}Mn_xTe_3$. *Physical Review B: Condensed Matter and Materials Physics*, 81:195203, May 2010.

[162] Y Okada, C Dhital, W Zhou, E D Huemiller, H Lin, S Basak, A Bansil, Y B Huang, H Ding, Z Wang, S D Wilson, and V Madhavan. Direct observation of broken time-reversal symmetry on the surface of a magnetically doped topological insulator. *Physical Review Letters*, 106:206805, May 2011.

[163] L A Wray, S Y Xu, Y Xia, D Hsieh, A V Fedorov, Y S Hor, R J Cava, A Bansil, H Lin, and M Z Hasan. A topological insulator surface under strong Cou-

lomb, magnetic and disorder perturbations. *Nature Physics*, 7(1):32–37, January 2011.

[164] P Wei, F Katmis, B A Assaf, H Steinberg, P Jarillo-Herrero, D Heiman, and J S Moodera. Exchange-coupling-induced symmetry breaking in topological insulators. *Physical Review Letters*, 110:186807, April 2013.

[165] O Kahn. *Molecular magnetism*. VCH, August 1993.

[166] S J Blundell and F L Pratt. Organic and molecular magnets. *Journal of Physics: Condensed Matter*, 16(24):R771–R828, June 2004.

[167] D Gatteschi, R Sessoli, and J Villain. *Molecular Nanomagnets*. Oxford University Press, March 2006.

[168] M Verdaguer and G S Girolami. Magnetic Prussian blue analogs. In J S Miller and D Marc, editors, *Magnetism: Molecules to Materials V*, chapter 9, pages 283–346. Wiley-Blackwell, July 2005.

[169] D Gatteschi. Single molecule magnets: a new class of magnetic materials. *Journal of Alloys and Compounds*, 317–318:8–12, April 2001. The 13$^{\underline{\text{th}}}$ International Conference on Solid Compounds of Transition Elements.

[170] G Aromí, E J L McInnes, and R E P Winpenny. Recent synthetic results involving single molecule magnets. In R Winpenny, editor, *Molecular Cluster Magnets*, number 3 in World Scientific Series in Nanoscience and Nanotechnology, chapter 2, pages 59–108. World Scientific, October 2011.

[171] M N Leuenberger and D Loss. Quantum computing in molecular magnets. *Nature*, 410(6830):789–793, April 2001.

[172] F Meier, J Levy, and D Loss. Quantum computing with spin cluster qubits. *Physical Review Letters*, 90:047901, January 2003.

[173] O Rival. *Organic materials for quantum computation*. DPhil thesis, University of Oxford, 2009.

[174] D Kaminski. *Electron Spin Resonance of Molecular Magnets for Quantum Information Processing*. DPhil thesis, University of Oxford, 2015.

[175] A Abragam and B Bleaney. *Electron Paramagnetic Resonance of Transition Ions*. Oxford Classic Texts in the Physical Sciences. Oxford University Press, reissued 1970 edition, June 2012.

[176] F Moro, D Kaminski, F Tuna, G F S Whitehead, G A Timco, D Collison, R E P Winpenny, A Ardavan, and E J L McInnes. Coherent electron spin manipulation in a dilute oriented ensemble of molecular nanomagnets: pulsed EPR on doped single crystals. *Chemical Communications*, 50(1):91–93, November 2014.

[177] J van Slageren, R Sessoli, D Gatteschi, A A Smith, M Helliwell, R E P Winpenny, A Cornia, A L Barra, A G M Jansen, E Rentschler, and G A Timco. Magnetic anisotropy of the antiferromagnetic ring $[Cr_8F_8Piv_{16}]$. *Chemistry: a European Journal*, 8(1):277–285, January 2002.

[178] J Schnack and M Luban. Rotational modes in molecular magnets with antiferromagnetic Heisenberg exchange. *Physical Review B: Condensed Matter and Materials Physics*, 63:014418, December 2000.

[179] S Carretta, J van Slageren, T Guidi, E Liviotti, C Mondelli, D Rovai, A Cornia, A L Dearden, F Carsughi, M Affronte, C D Frost, R E P Winpenny, D Gatteschi, G Amoretti, and R Caciuffo. Microscopic spin Hamiltonian of a Cr_8 antiferromagnetic ring from inelastic neutron scattering. *Physical Review B: Condensed Matter and Materials Physics*, 67:094405, March 2003.

[180] O Waldmann, T Guidi, S Carretta, C Mondelli, and A L Dearden. Elementary excitations in the cyclic molecular nanomagnet Cr_8. *Physical Review Letters*, 91:237202, December 2003.

[181] F K Larsen, E J L McInnes, H E Mkami, J Overgaard, S Piligkos, G Rajaraman, E Rentschler, A A Smith, G M Smith, V Boote, M Jennings, G A Timco, and R E P Winpenny. Synthesis and characterization of heterometallic Cr_7M wheels. *Angewandte Chemie, International Edition*, 42(1):101–105, January 2003.

[182] A Ghirri, V Corradini, V Bellini, R Biagi, U del Pennino, V D Renzi, J C Cezar, C A Muryn, G A Timco, R E P Winpenny, and M Affronte. Self-assembled monolayer of Cr_7Ni molecular nanomagnets by sublimation. *ACS Nano*, 5(9):7090–7099, August 2011.

[183] Q Liu, C X Liu, C Xu, X L Qi, and S C Zhang. Magnetic impurities on the surface of a topological insulator. *Physical Review Letters*, 102:156603, April 2009.

[184] S Carretta and A Chiesa. Personal correspondence. May 2017.

[185] F Chen, C Shang, Z Jin, D Zhao, Y P Wu, Z J Xiang, Z C Xia, A F Wang, X G Luo, T Wu, and X H Chen. Magnetoresistance evidence of a surface state

and a field-dependent insulating state in the Kondo insulator SmB_6. *Physical Review B: Condensed Matter and Materials Physics*, 91:205133, May 2015.

[186] S Blundell and K Blundell. *Concepts in Thermal Physics*. Oxford University Press, 2nd edition, October 2009.

[187] S Hikami, A I Larkin, and Y Nagaoka. Spin-orbit interaction and magnetoresistance in the two dimensional random system. *Progress of Theoretical Physics*, 63(2):707–710, February 1980.

[188] C Sanchez-Castro. Negative magnetoresistance of $Ce_3Bi_4Pt_3$ at low temperatures. *Physical Review B: Condensed Matter and Materials Physics*, 49:4421–4424, February 1994.

[189] J C Cooley, C H Mielke, W L Hults, J D Goettee, M M Honold, R M Modler, A Lacerda, D G Rickel, and J L Smith. High field gap closure in the Kondo insulator SmB_6. *Journal of Superconductivity*, 12(1):171–173, February 1999.

[190] M F Hundley, A Lacerda, P C Canfield, J D Thompson, and Z Fisk. Magnetoresistance of the Kondo insulator $Ce_3Bi_4Pt_3$. *Physica B: Condensed Matter*, 186–188:425–427, May 1993.

[191] Z Yue, X Wang, D Wang, J Wang, D Culcer, and S Dou. Crossover of magnetoresistance from fourfold to twofold symmetry in SmB_6 single crystal, a topological Kondo insulator. *Journal of the Physical Society of Japan*, 84(4):044717, April 2015.

[192] J E Sader, J W M Chon, and P Mulvaney. Calibration of rectangular atomic force microscope cantilevers. *Review of Scientific Instruments*, 70(10):3967–3969, July 1999.

[193] W A Phelan, S M Koohpayeh, P Cottingham, J A Tutmaher, J C Leiner, M D Lumsden, C M Lavelle, X P Wang, C Hoffmann, M A Siegler, N Haldolaarachchige, D P Young, and T M McQueen. On the chemistry and physical properties of flux and floating zone grown SmB_6 single crystals. *Scientific Reports*, 6:20860, February 2016.

COLOPHON

This thesis was typeset using the typographical look-and-feel classicthesis developed by André Miede, using the Linux Libertine and Pazo Math fonts. Miede's style was inspired by Robert Bringhurst's seminal book on typography, The Elements of Typographic Style. classicthesis is available for both LaTeX and LyX:

https://bitbucket.org/amiede/classicthesis/

Revised version with examiners' recommended corrections, 3rd October 2017 (DPhil thesis, *Nano- and micro-scale techniques for electrical transport measurements*).